UNIVERSITY OF CALIFORNIA SAN DIEGO

Studies on molecular polaritons: condensates, topology, and metrology

A dissertation submitted in partial satisfaction of the
requirements for the degree Doctor of Philosophy

in

Chemistry

by

Sindhana Selvi Pannir Sivajothi

Committee in charge:

Professor Joel Yuen-Zhou, Chair
Professor Michael Fogler
Professor Michael Galperin
Professor Francesco Paesani
Professor Haim Weizman

2023

The Dissertation of Sindhana Selvi Pannir Sivajothi is approved, and it is acceptable in quality and form for publication on microfilm and electronically.

University of California San Diego

2023

TABLE OF CONTENTS

LIST OF FIGURES

ACKNOWLEDGEMENTS

I would like to thank my advisor, Professor Joel Yuen-Zhou, for his unwavering support and investment in my professional growth. His guidance has played a pivotal role in shaping my academic journey and preparing me for future challenges. I am also grateful to Jorge A. Campos-Gonzalez-Angulo and Luis A. Martínez-Martínez for their invaluable mentorship during my early years in graduate school.

I am deeply grateful for the friendship and stimulating scientific discussions shared with Juan B. Pérez-Sánchez and Kai Schwennicke. Their insights and perspectives have improved my understanding and inspired ideas not only in science, but also outside of it. I would also like to express my gratitude to Yong Rui Poh and Arghadip Koner for their thought-provoking questions that have consistently challenged my ideas and pushed the boundaries of my understanding. I am also grateful to Matthew Du, Raphael Ribeiro, Michael Reitz, and Sricharan RC for scientific discussions that have contributed to my intellectual growth.

My deepest appreciation goes to my parents, P. Sivajothi and E. Pannir Selvam, my sister P.S. Yazhini, and my aunt S. Vasanthi for their steadfast support and constant encouragement. Their belief in my abilities has been a driving force behind my accomplishments.

I am incredibly fortunate to have Shubham Sinha as my partner. His enthusiasm for scientific discussions and unwavering support during challenging times have helped me navigate the complexities of graduate school with confidence.

I would also like to express my gratitude to my close friends, Bhavya Rajasree Bhaskar, Subbulakshmi S, Ravi Jambhekar, Saswata Chatterjee, Randall Lionel Kharkrang, Appilineni Kushal, Mingjie Chen, Jyotsna Gidugu, Nandagopal Ramachandran, Jun Bo Lau, S. Balaji Venkat, Woonam Lim, and Zeyu Liu. Their companionship has been a constant source of inspiration and joy, making my Ph.D. journey even more meaningful and rewarding.

Lastly, I express my gratitude to the UCSD women's ultimate frisbee team, Berserk Coalition, for their unwavering support throughout my Ph.D. journey. Being a part of this team has provided a sense of belonging and community in a country far from home.

Chapter 2, in full, is adapted from the material as it appears in "Driving chemical reactions with polariton condensates," S. Pannir-Sivajothi, J. A. Campos-Gonzalez-Angulo, L. A. Martínez-Martínez, S. Sinha, J. Yuen-Zhou, *Nat. Commun.* **13**, 1–9 (2022). The dissertation author was the primary investigator and author of this paper.

Chapter 3, in full, is adapted from the material as it appears in "Molecular and solid-state topological polaritons induced by population imbalance," S. Pannir-Sivajothi, N. P. Stern, J. Yuen-Zhou, *Nanophotonics* **12**, 3109–3119 (2023). The dissertation author was the primary investigator and author of this paper.

Chapter 4, in part, has been submitted for publication as it appears in "Sub-wavelength chemical imaging of a modified reaction due to vibrational strong coupling," Z. Brawley, J. E. Yim*, S. Pannir-Sivajothi*, Y. R. Poh, J. Yuen-Zhou, and M. Sheldon, ChemRxiv preprint (2023). The dissertation author led the theoretical section of this paper (* indicates equal contribution).

Chapter 5, in full, is currently being prepared for submission for publication of the material. "Franck-Condon spectroscopy as quantum metrology," S. Pannir-Sivajothi, J. Yuen-Zhou. The dissertation author was the primary investigator and author of this material.

VITA

2018	Bachelor of Science (Research) in Physics, Indian Institute of Science
2018	Master of Science in Physics, Indian Institute of Science
2018–2019	Teaching Assistant, University of California San Diego
2020–2023	Graduate Student Researcher, University of California San Diego
2023	Doctor of Philosophy in Chemistry, University of California San Diego

PUBLICATIONS

A. Koner, M. Du, S. Pannir-Sivajothi, R. H. Goldsmith, and J. Yuen-Zhou, "A path towards single molecule vibrational strong coupling in a Fabry–Pérot microcavity", *Chemical Science*, in press (2023).

S. Pannir-Sivajothi, N. P. Stern, and J. Yuen-Zhou, "Molecular and solid-state topological polaritons induced by population imbalance," *Nanophotonics* **12**, 3109–3119 (2023).

Y. R. Poh, S. Pannir-Sivajothi, and J. Yuen-Zhou, "Understanding the energygap law under vibrational strong coupling", *J. Phys. Chem. C* **127**, 5491–5501 (2023).

S. Pannir-Sivajothi, J. A. Campos-Gonzalez-Angulo, L. A. Martínez-Martínez, S. Sinha, and J. Yuen-Zhou, "Driving chemical reactions with polariton condensates," *Nat. Commun.* **13**, 1–9 (2022).

J. Chattopadhyay, S. Pannir-Sivajothi, K. Varma, S. Ramaswamy, C. Dasgupta, and P. K. Maiti, "Heating leads to liquid-crystal and crystalline order ina two-temperature active fluid of rods", *Phys. Rev. E* **104**, 054610 (2021).

S. Pannir-Sivajothi, S.-T. Lin, and P. K. Maiti, "Efficient computation ofentropy and other thermodynamic properties for two-dimensional systems using two-phase thermodynamic model", *J. Phys. Chem. B* **123**, 180–193 (2018).

ABSTRACT OF THE DISSERTATION

Studies on molecular polaritons: condensates, topology, and metrology

by

Sindhana Selvi Pannir Sivajothi

Doctor of Philosophy in Chemistry

University of California San Diego, 2023

Professor Joel Yuen-Zhou, Chair

When optical transitions in materials couple strongly to photon modes, light and matter degrees of freedom can no longer be treated separately with the light-matter coupling taken as a perturbation. They form hybrid light-matter modes called polariton modes. Several experiments over the last decade have demonstrated a change in chemical reactivity under collective vibrational strong coupling, where vibrational modes in many molecules couple collectively to a photon mode, starting the field of polariton chemistry. However, from theoretical studies, there is no clear explanation for this phenomenon. Additionally, some recent experiments have shown no effect of collective strong light-matter coupling on reactivity.

In this dissertation, we propose strategies to enhance polaritonic effects and we also seek

out avenues outside of chemical reactivity where the effect of strong light-matter coupling could be significant. We demonstrate that the effect of polaritons on chemical reactivity under vibrational strong coupling can be enhanced by vibrational polariton condensation. The macroscopic occupation of the polariton mode through Bose-Einstein condensation amplifies its contribution to the reaction rate.

To explain an experimentally observed reduction in the dehydration temperature in an open cavity system under vibrational strong coupling on resonance, we develop a theoretical model for heat flow based on kinetic equations. We hypothesized that the reduction in temperature is not due to an inherent change in the dehydration temperature of the material, but due to a reduction in the thermal contact resistance across the interface between the molecules and the plasmonic structure due to polaritons.

We also show that the topological properties of a system under electronic strong coupling can be modified through optical pumping with circularly polarized light. Our work relies on selectively saturating electronic transitions with circularly polarized light, and, therefore, creating a population imbalance in the system and breaking time-reversal symmetry.

In the last part of this dissertation, we propose a way to measure small differences in the equilibrium positions of the vibrational coordinate between different electronic states using higher-energy Fock states. This work does not require strong light-matter coupling. Higher-energy vibrational Fock states have a smaller length scale associated with them than the ground vibrational state which aids in inferring smaller displacements in the vibrational coordinate from the electronic absorption spectrum.

Chapter 1

Introduction

Interaction between light and matter is ubiquitous in everyday life, from vision to photosynthesis. In chemical research, there are two primary uses of light: (a) to drive chemical changes in materials and alter their structure, for example, in photochemical reactions, and (b) to probe the structure and dynamics of molecules through spectroscopy. In this dissertation, we theoretically investigate projects that fall under both categories under different strengths of light-matter coupling.

Increasing the coupling between light and matter may enhance the effect of light on optically driven molecular processes. By engineering the environment of molecules, the strength of light-molecule coupling can be modified. For example, placing molecules between a pair of mirrors that are micrometers apart (Fabry-Perot cavity) can increase the light-matter coupling strength. In a variety of such systems [1–5], it has been demonstrated that the light-matter coupling can reach the strong coupling regime where the the photon mode and the material transition exchange energy faster than the decay rate of these excitations. These systems have hybrid quantum states called polariton states that possess properties of both light and molecules. Depending on the type of material excitation that hybridizes with light, different types of polaritons are formed; for instance, exciton-polaritons are formed when electronic transitions in materials strongly couple with light [1, 3, 5]. Experiments in 2015 revealed that strong light-matter coupling in molecules can be achieved not only with electronic transitions, but also

with vibrational transitions [2, 6]. Polaritons formed when molecular vibrations couple strongly with light are termed 'vibrational polaritons'. For a large part of my dissertation, I focus on such strongly coupled systems.

In a Bose-Einstein condensate (BEC), a macroscopic number of atoms/particles occupy the same quantum mechanical state. As Bose-Einstein condensates are manifestations of quantum mechanical effects at the macroscopic scale, they are of interest to the scientific community. In the early 2000s, researchers studied the effect of macroscopic coherence of BECs of molecules on chemical reactivity [7, 8]. However, cryogenic temperatures are required to achieve a BEC of atoms or molecules; this limits its practical application. Motivated by this work, in this dissertation, we study the effect of BECs on chemical reactions but in a different context: using BECs of polaritons. Owing to their hybrid nature and low effective mass, exciton-polariton condensation has been achieved at room temperature [9, 10], making it a technologically relevant platform to explore the effects of Bose-Einstein condensation on chemical reactivity. To the best of my knowledge, our theoretical work was the first to study the effect of polariton condensation on chemical reactivity [11]. As vibrational polaritons are a relatively recent development in the field of polaritonics, unlike BECs of exciton-polariton, BECs of vibrational polaritons have not been experimentally demonstrated yet. In this dissertation, we also theoretically show that vibrational polariton condensation should be within reach with current technological capabilities. Additionally, we outline the conditions under which vibrational polariton condensation can be realized and propose potential molecules where it would be feasible at room temperature [11].

Topological effects represent a fascinating set of phenomena that could have a significant impact on technological advancement as topological systems possess edge states that allow for unidirectional flow of energy with low losses. In this dissertation, we undertake theoretical investigations into the modification of topology in systems with strong light-matter coupling through the process of pumping with circularly polarized light [12]. By utilizing either left or right circularly polarized light for the pumping, the sign of the topological invariant, an integer that characterizes the system's properties, can be flipped. This opens up possibilities for reversible

optical control over the topological invariants of the system, paving the way for the development of topological opto-electronic devices.

Both research projects mentioned so far involved optical driving. However, several experiments over the last decade have reported a change in chemical reactivity under collective vibrational strong coupling, even in the dark – without optical pumping [13–16]. From theoretical studies, there is no clear explanation for this phenomenon [17]. Additionally, some recent experiments have shown no effect of strong light-matter coupling on reactivity in the dark [18, 19]. To explain a similar observation from our experimental collaborators on the reduction of dehydration temperature in an open cavity system under collective vibrational strong coupling, we followed a different approach [20]. As the experimental setup was heated using a heating stage and the open cavity was in contact with room temperature air, there must be a temperature gradient across the system. We hypothesized that the reduction in stage temperature required to achieve dehydration is not due to an inherent change in the dehydration temperature of the material, but due to a reduction in the thermal contact resistance across the interface between the molecules and the nanocavity due to radiative heat transfer through polaritons. This leads to a different observed stage temperature at dehydration even if there is no change in the inherent dehydration temperature of the molecules. We developed a phenomenological model for heat flow under strong light-matter coupling based on kinetic rate equations to support the experimental observation.

The last chapter in this dissertation is a theoretical proposal that uses light to measure small differences in the equilibrium positions of atoms between the ground and excited electronic states. Currently, such differences can be inferred from the intensities of the vibrational sidebands in the spectrum. However, due to limits to precision of the spectroscopic device and noise, this method can only detect displacements of the order of $\sqrt{\frac{\hbar}{m\omega}}$ or larger, as the initial state—the vibrational ground state—has a length scale $\sqrt{\frac{\hbar}{m\omega}}$ associated in position space. In our work, we propose preparing the system in a higher vibrational state. As the position space wavefunction of the higher vibrational state has a much smaller associated wavelength, it enables measurement of

smaller distances than the ground state. This approach could have significant implications for experimentally determining changes in nuclear configurations of molecules between ground and excited electronic states.

1.1 Summary of contents

In Chapter 2, adapted from [11], we study the effect of vibrational polariton condensation on an electron transfer process. We use Marcus-Levich-Jortner theory to model the electron transfer process and explore the effects of polariton condensation on both the rates and yields of the reaction. Note that both the backward and forward reaction rates are enhanced under condensation. We also identify the range of temperatures and collective light-matter coupling strengths where vibrational polariton condensation is feasible.

In Chapter 3, adapted from [12], we explore topological properties of systems with strong light-matter coupling under optical pumping with circularly polarized light. We consider a large number of molecules, modeled as three level systems, strongly coupled to the modes of a Fabry-Perot cavity. We derive an effective Hamiltonian under optical pumping using mean field theory and study the Berry curvature of the polariton bands.

In Chapter 4, adapted from [20], we develop a theoretical model to explain the experimental finding of reduced heating stage temperature required for a dehydration reaction under resonance condition for an open cavity system with vibrational strong coupling. We use kinetic rate equations to understand radiative heat transport across an interface with a large thermal resistance and hypothesize that the observed reduction in temperature required for the dehydration under resonance condition is due to a decrease in the thermal resistance across the interface due to additional polariton channels.

In Chapter 5, we propose a way to measure small differences in the equilibrium position of the vibrational coordinate between different electronic states. For large displacements, comparable to the width of the ground vibrational wavefunction, vibrational sidebands in the

electronic absorption spectrum can be used. We identify a smaller length scale associated with higher vibrational Fock states which come into play if we initialize the system in a higher Fock state and this smaller length scale can be used to measure small displacements.

Chapter 6 of this dissertation presents conclusions of the research and provides an outlook for future directions.

Chapter 2

Driving chemical reactions with polariton condensates

2.1 Introduction

Light and matter couple strongly when a large number of molecules are placed within optical cavities that confine light [1, 2, 6]. As a result, hybrid light-matter excitations called polaritons form when a collective molecular transition and a photon mode coherently exchange energy faster than the individual decay from each component. Light-matter strong coupling (SC) opens up a new path to modify material properties by controlling their electromagnetic environment [15, 21]. For instance, vibrational strong coupling (VSC), where an infrared cavity mode couples to an ensemble of localized molecular vibrations in a film or solution, influences chemical reactivity even without external pumping [13, 14]. However, the microscopic mechanism for modification of molecular processes through hybridization with light is still poorly understood [22–24], since it could be limited by the presence of a large number of quasi-degenerate dark modes that do not possess any photonic character and are likely to behave similarly to uncoupled molecules [24].

A Bose-Einstein condensate of polaritons [25] offers a solution to this problem since the macroscopic occupation of polaritonic states enhances the effects from SC. In the last decade, Bose-Einstein condensation has been demonstrated in several organic exciton-polariton systems at room temperature [26–29]. Recently, organic polariton condensates were used to build polariton

transistors [30], and theoretical predictions suggest they may also modify incoherent charge transport [31]. Interestingly, the consequences of polariton condensation on chemical reactivity have not been addressed in the literature prior to the present study.

Ideas of using Bose-Einstein condensates of molecules in chemistry have been previously proposed, but they require ultracold temperatures due to the large mass of the condensing entities [7,8]. The low effective mass that polaritons inherit from their photonic component, along with the large binding energy of Frenkel excitons, enables room-temperature condensation [9]. The partly photonic character of polaritons also offers additional benefits such as delocalization and remote action for manipulating chemistry [32].

Here, we investigate the effect of polariton condensation on electron transfer (ET) (Fig. 2.1). While the reaction yield under infrared laser excitation, without SC, already differs from that under thermal equilibrium conditions [33, 34], polariton condensation amplifies this difference by changing the activation barrier for the forward and backward reactions unevenly, tilting the equilibrium towards either reactants or products.

2.2 Results

2.2.1 Bose-Einstein condensation of vibrational polaritons

Bose-Einstein condensation of vibrational polaritons has not been experimentally achieved yet; however, as we shall argue, there are compelling reasons to believe that they are presently within reach. Most theoretical investigations on polariton condensation with organic microcavities involve systems under electronic strong coupling (ESC) [35, 36]; polariton condensation under VSC requires a separate treatment due to the difference in energy scales and the involved relaxation pathways [37]. While typical bare exciton energies range from 2-3 eV with Rabi splitting ~ 200 meV under ESC, the bare frequency of vibrations is 100-300 meV with Rabi splitting $\sim 20-40$ meV under VSC. Since the Rabi splitting is of the order of $k_{\mathrm{B}}T$ at room temperature, thermal effects are crucial for vibrational polaritons. Under ESC, polariton relaxation is assisted by

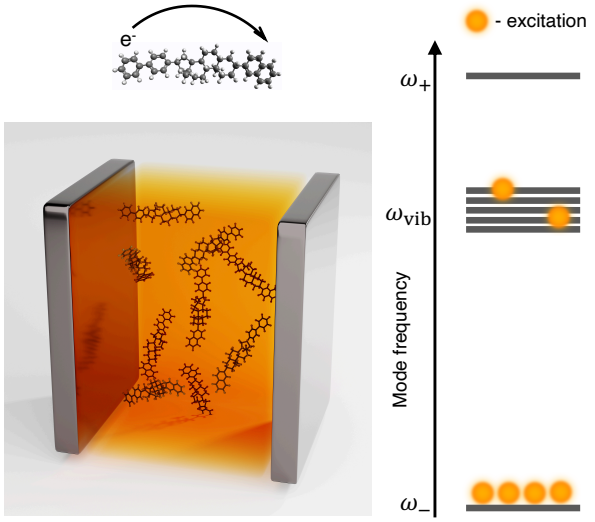

Figure 2.1. Vibrational polariton condensate. A large number of molecules are placed inside an optical cavity where their vibrations strongly couple to the cavity mode. The system is constantly pumped to create a polariton condensate and the right side of the figure depicts the occupation of different modes under condensation (frequencies of the upper polariton, dark modes and lower polariton are ω_+, ω_{vib} and ω_-, respectively). The rate of intramolecular electron transfer under vibrational polariton condensation is investigated.

high-frequency intramolecular vibrations [38], whereas, under VSC, low-frequency solvent modes play a key role in this process [39, 40], similar to what happens in THz phonon Fröhlich condensation in biomolecules [41, 42].

We model the polariton system as a set of N vibrational modes ($\hat{a}_{\text{vib},j}$), with frequency ω_{vib}, strongly coupled to a single photon mode ($\hat{a}_{\text{ph}}$) with frequency ω_{ph}. In the Hamiltonian of the system,

$$\begin{aligned}\hat{H} =&\hbar\omega_{\text{ph}}\left(\hat{a}^\dagger_{\text{ph}}\hat{a}_{\text{ph}} + \frac{1}{2}\right) + \hbar\omega_{\text{vib}}\sum_{j=1}^{N}\left(\hat{a}^\dagger_{\text{vib},j}\hat{a}_{\text{vib},j} + \frac{1}{2}\right)\\ &+ \sum_{j=1}^{N}\hbar g\left(\hat{a}^\dagger_{\text{vib},j}\hat{a}_{\text{ph}} + \hat{a}^\dagger_{\text{ph}}\hat{a}_{\text{vib},j}\right),\end{aligned} \tag{2.1}$$

we have applied the rotating wave approximation. Upon diagonalization of this Hamiltonian, we get normal modes: lower and upper polaritons, and $N-1$ dark modes with frequencies ω_-, ω_+

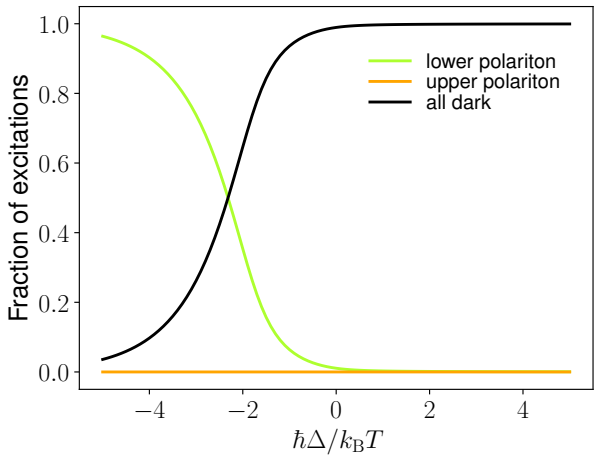

Figure 2.2. Polariton condensation transition. Fraction of excitations in different modes as a function of cavity detuning $\hbar\Delta = \hbar\omega_{\mathrm{ph}} - \hbar\omega_{\mathrm{vib}}$ while keeping the pumping rate P_- fixed. The black curve includes the excitations in all dark modes taken together while the green and orange curves show the fraction excitations in the lower and upper polariton, respectively. The condensation transition takes place close to $\hbar\Delta \approx -1.5k_{\mathrm{B}}T$. Here, the lower polariton is pumped with rate $P_- = 0.16N\Gamma_\downarrow$, the light-matter coupling $2\hbar g\sqrt{N} = 0.72k_{\mathrm{B}}T$, the temperature $k_{\mathrm{B}}T = 0.1389\hbar\omega_{\mathrm{vib}}$ ($T = 298$K when $\hbar\omega_{\mathrm{vib}} = 185$ meV), number of molecules $N = 10^7$ and cavity leakage rate $\kappa = \Gamma_\downarrow$.

and ω_{D}^k, respectively:

$$\begin{aligned} \omega_\pm &= \omega_{\mathrm{vib}} + \frac{\Delta \pm \Omega}{2}, \\ \omega_{\mathrm{D}}^k &= \omega_{\mathrm{vib}} \qquad\qquad 2 \le k \le N, \end{aligned} \tag{2.2}$$

where $\Omega = \sqrt{\Delta^2 + 4g^2N}$ is the Rabi splitting and $\Delta = \omega_{\mathrm{ph}} - \omega_{\mathrm{vib}}$ the detuning between cavity and molecular vibrations. To model polariton population dynamics, we use Boltzmann rate equations where the polariton system is weakly coupled to a low-frequency solvent bath, which enables scattering between modes [43]. These rate equations also account for final-state stimulation,

$$\frac{dn_i}{dt} = \sum_j \Big(W_{ij} n_j (1 + n_i) - W_{ji}(1 + n_j) n_i \Big) - \gamma_i n_i + P_i, \tag{2.3}$$

where n_i is the population, γ_i is the decay rate and P_i is the external pumping rate of the i^{th} mode. The scattering rate from mode j to i, W_{ij}, satisfies detailed balance: $W_{ij}/W_{ji} = e^{-\beta(\epsilon_i - \epsilon_j)}$. Here, $\beta = 1/(k_{\mathrm{B}}T)$, k_B is the Boltzmann constant, T is the temperature and $\epsilon_i = \hbar\omega_i$ where ω_i is the

frequency of the i^{th} mode. The decay from different modes is $\gamma_i = |c^i_{\text{vib}}|^2\Gamma_\downarrow + |c^i_{\text{ph}}|^2\kappa$, where $|c^i_{\text{vib}}|^2$ and $|c^i_{\text{ph}}|^2$ are the molecular and photon fraction, respectively, $\Gamma_\downarrow$ is the decay rate of the molecular vibrations, and κ is the cavity leakage rate.

Two factors play a determining role in the condensation threshold: (i) the rate of scattering between polariton and dark modes relative to losses from the system, *i.e.* the rate of thermalization, and (ii) the abundance of modes close in energy to the condensing mode [44]. For all calculations, we assume fast thermalization. As mentioned in (ii), the presence of many modes close to the lower polariton would deter condensation by distributing the energy pumped into the system among all these modes. Thus, the energetic proximity between the dark state manifold, which has a large density of states (DOS), and the lower polariton poses one of the biggest challenges for polariton condensation under VSC.

The distribution of excitations between the polariton and dark modes is shown in Fig. 2.2 for different detunings and we observe a condensation transition at $\hbar\Delta \approx -1.5k_{\text{B}}T$ (see Supplementary Note 2 for details). Above the condensation threshold, a large fraction of excitations reside in the lower polariton $\frac{n_-}{(\sum_{k=2}^{\infty} n^k_{\text{D}})} \gg \frac{1}{(N-1)e^{-\beta\hbar(\Omega-\Delta)/2}}$.

The average population per molecule at the condensation threshold $\bar{n} = P_{\text{th}}/N\Gamma_\downarrow$ is a good measure of the feasibility of vibrational polariton condensation. For instance, demanding population inversion, $\bar{n} > 0.5$, would be experimentally difficult to achieve in general. In Fig. 2.3, we plot $\bar{n}$ for different light-matter coupling strengths, $2\hbar g\sqrt{N}$, and detunings, $\hbar\Delta$. Here, we numerically obtain P_{th} as the pumping rate when 10% of the excitations are in the lower polariton. The threshold obtained this way closely corresponds with the theoretical condition for condensation

$$\bar{n}^k_{\text{D}} > n_{\text{solvent}}\Big(\frac{\hbar(\Omega-\Delta)}{2}\Big), \tag{2.4}$$

where, $\bar{n}^k_{\text{D}} = \frac{1}{N-1}\sum_{k=2}^{N} n^k_{\text{D}}$ is the average occupation of a dark mode, and $n_{\text{solvent}}(E)$ is the Bose-Einstein population of a solvent mode with energy E at room temperature T_{room} [44]. The energy difference between the lower polariton and the dark state reservoir $\hbar(\Omega-\Delta)/2$ determines

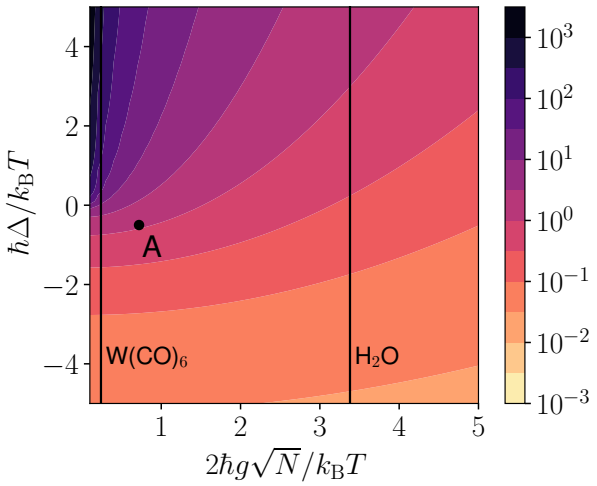

Figure 2.3. Polariton condensation threshold. Numerically obtained average population per molecule at the condensation threshold $\bar{n} = P_{\text{th}}/N\Gamma_{\downarrow}$ (10% of the excitations are in the lower polariton), for a range of light-matter coupling strengths $2\hbar g\sqrt{N}$ and cavity detunings $\hbar\Delta = \hbar\omega_{\text{ph}} - \hbar\omega_{\text{vib}}$. In the black and purple regions of the plot ($\Delta > 0$ and $2\hbar g\sqrt{N}/k_BT < 2$), the threshold for condensation is high, $\bar{n} \gg 1$, and polariton condensation is difficult to achieve experimentally. The threshold for condensation is much lower, $\bar{n} < 0.1$, for the lighter colored (yellow, orange) regions. In our plot above only the upper polariton is pumped and we use cavity leakage rate $\kappa = \Gamma_{\downarrow}$. The vertical lines correspond to $2\hbar g\sqrt{N}/k_BT$ at room temperature for H_2O ($2\hbar g\sqrt{N} \approx 700\text{cm}^{-1}$) and $W(CO)_6$ ($2\hbar g\sqrt{N} \approx 50\text{cm}^{-1}$). Calculations in Fig. 2.4-2.6 are presented for the conditions in point A.

the condensation threshold. From Fig. 3 we see that vibrational polariton condensation is feasible for water even at room temperature for up to zero detuning.

Our model does not include disorder; as a result, all dark modes are degenerate at frequency ω_{vib}, but in experimental systems, inhomogeneous broadening of transitions can lead to non-zero density of dark states even at the bottom of the lower polariton branch [45]. This fact will affect the condensation threshold, and should be considered in the future while looking for experimental systems that can demonstrate vibrational polariton condensation. Stimulating the lower polariton directly by shining a resonant laser on it [30] or using a Raman scattering scheme [46] can help overcome this issue by dynamically lowering the condensation threshold.

2.2.2 Chemical reactions and vibrational polariton condensation

Electron transfer has been theoretically studied under both ESC [47, 48] and VSC [49, 50]. Here, we look at how vibrational polariton condensation affects the rate of intramolecular nonadiabatic electron transfer using the VSC version [49] of the Marcus-Levich-Jortner (MLJ) model [51–53].

Our system consists of N molecules placed inside an optical cavity supporting a single photon mode with bosonic operator $\hat{a}_{\text{ph}}$ and frequency ω_{ph}. The molecules can be in the reactant R or product P electronic state; for the i^{th} molecule, these states are denoted by $|\text{R}_i\rangle$ and $|\text{P}_i\rangle$, respectively. Each electronic state is dressed with a high-frequency intramolecular vibrational mode with bosonic operator $\hat{a}_{x,i}$ and frequency ω_{vib} where $x = \text{R}, \text{P}$; this mode couples to the photon mode. The equilibrium geometry of this vibrational mode depends on the electronic state according to,

$$\hat{a}_{\text{R},i} = \hat{D}_i^\dagger \hat{a}_{\text{P},i} \hat{D}_i, \tag{2.5}$$

where $\hat{D}_i = \exp\Big((\hat{a}_{\text{P},i}^\dagger - \hat{a}_{\text{P},i})\sqrt{S}\Big)$ and S is the Huang-Rhys factor.

Apart from the intramolecular vibrations, an effective low-frequency solvent mode surrounding each molecule facilitates ET. It is treated classically, with $\mathbf{q}_{\text{S},i}$ and $\mathbf{p}_{\text{S},i}$ being its position and momentum.

The Hamiltonian $\hat{H}$ for the full system is a generalization of Eq. (2.1) to account for the chemical reaction,

$$\hat{H} = \hat{H}_0 + \hat{V}_{\text{react}}, \tag{2.6}$$

and

$$\begin{aligned} \hat{H}_0 =& \hat{H}_{\text{ph}} + \sum_{i=1}^{N} \sum_{x=\text{R,P}} (\hat{H}_{x,i} + \hat{V}_{x,i}) \, |x_i\rangle \langle x_i| \,, \\ \hat{V}_{\text{react}} =& \sum_{i=1}^{N} J_{\text{RP}} \Big(|\text{R}_i\rangle \langle \text{P}_i| + |\text{P}_i\rangle \langle \text{R}_i| \Big). \end{aligned} \tag{2.7}$$

where $\hat{H}_0$ describes the photon ($\hat{H}_{\text{ph}}$), intramolecular vibrations and solvent modes of the i^{th}

molecule ($\hat{H}_{x,i}$), and light-matter couplings ($\hat{V}_{x,i}$). The diabatic coupling $\hat{V}_{\text{react}}$ is a perturbation that couples R and P electronic states with coupling strength J_{RP}. We have taken the dipole moment to be zero when the vibrational coordinate is in its equilibrium position in both R and P electronic states. Relaxing this assumption will add terms of the form $c_x(\hat{a}_{\text{ph}} + \hat{a}_{\text{ph}}) \left|x_i\right\rangle \left\langle x_i\right|$ to the Hamiltonian and will not affect the reaction rates calculated.

$$\begin{aligned}
\hat{H}_{\text{ph}} &= \hbar\omega_{\text{ph}}\left(\hat{a}^\dagger_{\text{ph}}\hat{a}_{\text{ph}} + \frac{1}{2}\right), \\
\hat{H}_{\text{R},i} &= \hbar\omega_{\text{vib}}\left(\hat{a}^\dagger_{\text{R},i}\hat{a}_{\text{R},i} + \frac{1}{2}\right) + \frac{1}{2}\hbar\omega_{\text{S}}\left(|\mathbf{p}_{\text{S},i}|^2 + |\mathbf{q}_{\text{S},i} + \mathbf{d}_{\text{S}}|^2\right), \\
\hat{H}_{\text{P},i} &= \hbar\omega_{\text{vib}}\left(\hat{a}^\dagger_{\text{P},i}\hat{a}_{\text{P},i} + \frac{1}{2}\right) + \frac{1}{2}\hbar\omega_{\text{S}}\left(|\mathbf{p}_{\text{S},i}|^2 + |\mathbf{q}_{\text{S},i}|^2\right) + \Delta G, \\
\hat{V}_{x,i} &= \hbar g_x(\hat{a}^\dagger_{x,i}\hat{a}_{\text{ph}} + \hat{a}^\dagger_{\text{ph}}\hat{a}_{x,i}),
\end{aligned} \tag{2.8}$$

where ΔG is the free-energy difference of each individual molecule reaction.

We construct potential energy surfaces (PES) by parametrically diagonalizing $\hat{H}_0$ as a function of the solvent coordinate $\mathbf{q}_{\text{S},i}$. The operators $\hat{N}_{\text{R}} = \sum_{i=1}^{N} \left|\text{R}_i\right\rangle \left\langle \text{R}_i\right|$ and $\hat{N}_{\text{P}} = \sum_{i=1}^{N} \left|\text{P}_i\right\rangle \left\langle \text{P}_i\right|$ commute with H_0 and correspond to the number of R and P molecules, respectively. While dynamics under $\hat{H}_0$ conserves $N_{\text{R}}, N_{\text{P}}$, the effect of $\hat{V}_{\text{react}}$ is to induce reactive transitions that modify those quantities while keeping $N = N_{\text{R}} + N_{\text{P}}$ constant. We assign the label $1 \le i \le N_{\text{R}}$ to R molecules, and $N_{\text{R}} + 1 \le i \le N$ to P molecules. We also reorganize the intramolecular vibrations into a single bright mode,

$$\hat{a}_{\text{B}(N_{\text{R}},N_{\text{P}})} = \frac{1}{\sqrt{g_{\text{R}}^2 N_{\text{R}} + g_{\text{P}}^2 N_{\text{P}}}}\left(g_{\text{R}}\sum_{i=1}^{N_{\text{R}}}\hat{a}_{\text{R},i} + g_{\text{P}}\sum_{i=N_{\text{R}}+1}^{N}\hat{a}_{\text{P},i}\right), \tag{2.9}$$

that possesses the correct symmetry to couple with light and $N - 1$ dark modes (D_k),

$$\hat{a}^k_{\text{D}(N_{\text{R}},N_{\text{P}})} = \sum_{i=1}^{N_{\text{R}}} c_{k,i}\hat{a}_{\text{R},i} + \sum_{i=N_{\text{R}}+1}^{N} c_{k,i}\hat{a}_{\text{P},i}, \tag{2.10}$$

labeled by an additional index $2 \le k \le N$, which do not couple with light. The dark

modes are orthogonal to the bright mode $g_{\mathrm{R}} \sum_{i=1}^{N_{\mathrm{R}}} c_{k,i} + g_{\mathrm{P}} \sum_{i=N_{\mathrm{R}}+1}^{N} c_{k,i} = 0$, and to each other $\sum_{i=1}^{N} c_{k,i} c^*_{k',i} = \delta_{k,k'}$. Unless mentioned otherwise, the number of R and P molecules is N_{R} and N_{P}, respectively, and for brevity, we will drop $(N_{\mathrm{R}}, N_{\mathrm{P}})$ dependence in the subscript. The bright and photon modes combine to form the upper polariton (UP) $\hat{a}_+$, and lower polariton (LP) $\hat{a}_-$, modes:

$$\begin{aligned} \hat{a}_+ &= \cos\theta \hat{a}_{\mathrm{ph}} + \sin\theta \hat{a}_{\mathrm{B}}, \\ \hat{a}_- &= \sin\theta \hat{a}_{\mathrm{ph}} - \cos\theta \hat{a}_{\mathrm{B}}, \end{aligned} \tag{2.11}$$

with mixing angle,

$$\theta = \tan^{-1}\left[\frac{\Omega - \Delta}{2\sqrt{g_{\mathrm{R}}^2 N_{\mathrm{R}} + g_{\mathrm{P}}^2 N_{\mathrm{P}}}}\right], \tag{2.12}$$

where $\Omega = \sqrt{\Delta^2 + 4(g_{\mathrm{R}}^2 N_{\mathrm{R}} + g_{\mathrm{P}}^2 N_{\mathrm{P}})}$ is the Rabi splitting, and $\Delta = \omega_{\mathrm{ph}} - \omega_{\mathrm{vib}}$ the detuning between cavity and molecular vibrations. The eigenstates of $\hat{H}_0$ are the dark, upper and lower polariton modes with frequencies given in Eq. (2.2).

According to the MLJ theory, the rate constant for ET outside of an optical cavity depends on properties of the intramolecular and solvent modes [51–53]. Under laser driving, this rate constant is,

$$k_{\mathrm{R}\to\mathrm{P}}^{\mathrm{IR}} = \sum_{n=0}^{\infty} P_{\bar{n}}(n) k_{\mathrm{R}\to\mathrm{P}}(n) \tag{2.13}$$

where

$$\begin{aligned} k_{\mathrm{R}\to\mathrm{P}}(n) =& \sqrt{\frac{\pi}{\lambda_{\mathrm{S}} k_{\mathrm{B}} T}} \frac{|J_{\mathrm{RP}}|^2}{\hbar} \sum_{f=-n}^{\infty} |\langle n|n+f\rangle'|^2 \exp\left(-\frac{E_f^{\ddagger}}{k_{\mathrm{B}} T}\right), \\ P_{\bar{n}}(n) =& e^{-\bar{n}} \frac{\bar{n}^n}{n!}, \\ E_f^{\ddagger} =& \frac{(\Delta G + \lambda_{\mathrm{S}} + f\hbar\omega_{\mathrm{vib}})^2}{4\lambda_{\mathrm{S}}}, \\ \langle n|n+f\rangle' =& \langle n| \hat{D}_i |n+f\rangle . \end{aligned} \tag{2.14}$$

Here, $P_{\bar{n}}(n)$ is the Poisson distribution with average mode population $\bar{n}$, λ_{S} is the solvent reorganization energy, $E_f^{\ddagger}$ is the activation energy, and $|\langle n|n+f\rangle'|^2$ is the Franck-Condon (FC) factor, where $|n\rangle$ and $|n+f\rangle'$ are the intramolecular initial and final states, respectively. $P_{\bar{n}}(n)$

has been taken to correspond to the ideal laser driven-damped harmonic oscillator, leading to a coherent state in the vibrational mode. The presence of anharmonic couplings would lead to intramolecular vibrational energy redistribution (IVR) [54], reducing the value of $P_{\bar{n}}(n)$ for high-lying Fock states. However, as we shall see below, even under these ideal circumstances, the condensate can outcompete the laser-driven situation in terms of reactivity. We thus expect the benefits of the condensate to be enhanced when IVR processes are taken into account.

Apart from vibrations within the reacting molecule, under VSC, the ET process also depends on vibrations in all other molecules and the photon mode, and can be represented by,

$$\sum_{k=2}^{N} \mathrm{D}_k + \mathrm{LP} + \mathrm{UP} \rightarrow \sum_{k=2}^{N} \mathrm{D}'_k + \mathrm{LP}' + \mathrm{UP}'. \tag{2.15}$$

Here and hereafter, the primed and unprimed quantities refer to electronic states with $(N_\mathrm{R}, N_\mathrm{P})$ and $(N_\mathrm{R}-1, N_\mathrm{P}+1)$ reactant-product distributions, respectively. The symmetry of the light-matter coupling allows us to use the dark state basis introduced in [55] and [49] to reduce the number of modes involved in the reaction from $N+1$ to three,

$$\mathrm{D}_{\mathrm{R},c} + \mathrm{LP} + \mathrm{UP} \rightarrow \mathrm{D}'_{\mathrm{P},c} + \mathrm{LP}' + \mathrm{UP}'. \tag{2.16}$$

Here, the c^{th} molecule is reacting, while $\mathrm{D}_{x,c}$ and $\mathrm{D}'_{x,c}$ are dark modes highly localized in it, with corresponding operators $\hat{a}_\mathrm{D}^{(R,c)}$ and $\hat{a}_\mathrm{D}^{(P,c)\prime}$ (see Supplementary Note 1).

We perform all our calculations in this subsection using parameters from point A in Fig. 2.3 but while pumping the lower polariton. Here, $\hbar\Delta = -0.5 k_\mathrm{B}T$, $2\hbar g\sqrt{N} = 0.72 k_\mathrm{B}T$, $k_\mathrm{B}T = 0.1389\hbar\omega_\mathrm{vib}$ ($T = 298$K when $\hbar\omega_\mathrm{vib} = 185$ meV) and $N = 10^7$; we choose pumping rate $P_- = 0.08N\Gamma_\downarrow$, which leads to average mode populations $N_+ = 0.064$, $N_- = 1.94 \times 10^4$ and $N_\mathrm{D} = 0.078$ under symmetric coupling $g_\mathrm{R} = g_\mathrm{P} = g$. Here, 2.4% of all excitations reside in the lower polariton. To compare the reaction rates under polariton condensation and outside the cavity under pumping, we take $\bar{n} = 0.08$ in Eq. (2.13). Under condensation, the initial vibrational state

of the system can be described by $\rho = \sum_{n_+,n_-,n_D} P(n_+,n_-,n_D)\,|n_+,n_-,n_D\rangle\,\langle n_+,n_-,n_D|$, where the entries in $|n_+,n_-,n_D\rangle$ label number of quanta in the UP, LP and $D_{R,c}$ modes, respectively. The results from the rate equations Eq. (2.3) provide us only with the average steady-state mode populations, N_+, N_- and N_D, and not the distribution $P(n_+,n_-,n_D)$. For simplicity, we assume the semiclassical approximation $P(n_+,n_-,n_D) \approx \delta_{n_+,0} P^{\rm th}_{N_D}(n_D)\delta_{n_-,N_-}$, where $P^{\rm th}_{N_D}(n)$ is the thermal distribution with average population N_D. This approximation is reasonable for populations $N_+ < N_D \ll 1 \ll N_-$,

$$\rho = \sum_{n_D} P^{\rm th}_{N_D}(n_D)\,|0,N_-,n_D\rangle\,\langle 0,N_-,n_D|\,. \tag{2.17}$$

The product vibrational states are $|\nu_+,\nu_-,\nu_D\rangle'$.

We assume that cavity leakage and rate of scattering between modes is much faster than the rate of the chemical reaction. For a cavity with $\sim$ 100 ps lifetime and ET reactions with $1/k_{R\to P} \sim 10^6 - 10^2$ ps [56], this assumption is valid. Therefore, if the populations of polariton modes change during the course of reaction, they quickly reach a steady state before the next molecule reacts. Similarly, we also assume that the polariton and dark mode populations reach a steady state before the backward reaction takes place while computing the rate constant $k^{\rm cond}_{P\to R}$. Generalizing the cavity MLJ theory presented in [49], we calculate the rate constant

$$k^{\rm cond}_{R\to P} = \sum_{n=0}^{\infty} P^{\rm th}_{N_D}(n) k^{\rm cond}_{R\to P}(n) \tag{2.18}$$

for the forward reaction under polariton condensation, where

$$\begin{aligned} k^{\rm cond}_{R\to P}(n) &= \sqrt{\frac{\pi}{\lambda_S k_B T}}\frac{|J_{RP}|^2}{\hbar}\sum_{\nu_+=0}^{\infty}\sum_{\nu_-=0}^{\infty}\sum_{\nu_D=0}^{\infty} W^{f,n}_{\nu_+,\nu_-,\nu_D}, \\ W^{f,n}_{\nu_+,\nu_-,\nu_D} &= |F^{f,n}_{\nu_+,\nu_-,\nu_D}|^2 \times \exp\left(-\frac{E^{f,n\ddagger}_{\nu_+,\nu_-,\nu_D}}{k_B T}\right). \end{aligned} \tag{2.19}$$

The FC factor $|F^{f,n}_{\nu_+,\nu_-,\nu_D}|^2 = |\,\langle 0,N_-,n|\nu_+,\nu_-,\nu_D\rangle'\,|^2$, and activation energy $E^{f,n\ddagger}_{\nu_+,\nu_-,\nu_D}$ play an

important role in determining the rate constant.

While many methods have been developed for computing multimode FC factors [57–59], the focus has been on increasing the number of modes while keeping their occupation small. The current problem, however, offers a new technical challenge: the large occupation of LP makes the aforementioned methods computationally expensive. Instead, we draw inspiration from previous work that employs generating functions [58] and combine those techniques with the powerful Lagrange-Bürmann formula [60] to obtain analytical expressions for the required three-dimensional FC factors (see details in Supplementary Section S3).

The activation energies for the various channels of reactivity are,

$$E^{f,n\ddagger}_{\nu_+,\nu_-,\nu_\mathrm{D}} = \frac{(E_\mathrm{P}^{\nu_+,\nu_-,\nu_\mathrm{D}} - E_\mathrm{R}^{0,N_-,n} + \lambda_\mathrm{S})^2}{4\lambda_\mathrm{S}}, \tag{2.20}$$

where

$$\begin{aligned} E_\mathrm{P}^{\nu_+,\nu_-,\nu_\mathrm{D}} =& \Delta G + \hbar\Bigg[\omega'_+\left(\nu_+ + \frac{1}{2}\right) \\ &+ \omega'_-\left(\nu_- + \frac{1}{2}\right) + \omega_\mathrm{vib}\left(\nu_\mathrm{D} + \frac{1}{2}\right)\Bigg], \\ E_\mathrm{R}^{0,N_-,n} =& \hbar\left[\omega_+\frac{1}{2} + \omega_-\left(N_- + \frac{1}{2}\right) + \omega_\mathrm{vib}\left(n + \frac{1}{2}\right)\right]. \end{aligned} \tag{2.21}$$

When condensation takes place, the number of quanta in the lower polariton $N_- \sim 10^5$ is so large that the summation in $k^\mathrm{cond}_{\mathrm{R}\to\mathrm{P}}(n)$ becomes difficult to estimate. To simplify the computation and gain intuition, we group channels into sets with same change in total number of intramolecular vibrational quanta $f = \nu_+ + \nu_- + \nu_\mathrm{D} - N_- - n$ upon ET. The closeness in energy between PES with same f, and hence similar activation barriers, is the rationale for this grouping. $k^\mathrm{cond}_{\mathrm{R}\to\mathrm{P}}(n)$ then goes from a free summation over three indices ν_+, ν_- and ν_D into a summation

over four indices f, ν_+, ν_- and ν_D with the constraint $\nu_+ + \nu_- + \nu_\mathrm{D} = N_- + n + f$,

$$k^{\mathrm{cond}}_{\mathrm{R}\to\mathrm{P}}(n) = \sqrt{\frac{\pi}{\lambda_\mathrm{S} k_\mathrm{B} T}} \frac{|J_\mathrm{RP}|^2}{\hbar} \sum_{f=-N_- -n}^{\infty} \sum_{\nu_+,\nu_-,\nu_\mathrm{D}}^{\nu_+ + \nu_- + \nu_\mathrm{D} = N_- + n + f} W^{f,n}_{\nu_+,\nu_-,\nu_\mathrm{D}}. \tag{2.22}$$

To understand the qualitative difference between reactions under polariton condensation and external pumping without SC, in Fig 2.4a-b we plot the PESs (not to scale) showing the forward reaction under symmetric light-matter coupling and zero detuning. The yellow (black) parabolas in Fig. 2.4a-b represent PESs for a molecule in electronic state $|\mathrm{R}\rangle$ ($|\mathrm{P}\rangle$) and vibrational state $|2\rangle$ ($|2+f\rangle'$) in Fig. 2.4a and $|0, N_-, 2\rangle$ ($|0, N_-, 2+f\rangle'$) in Fig. 2.4b. The red parabolas in Fig. 2.4b are additional final PESs provided by the vibrational polariton condensate (hereafter referred to solely as "condensate") that account for all other final vibrational states $|\nu_+, \nu_-, \nu_\mathrm{D}\rangle'$.

The net rate of ET is,

$$\frac{dN_\mathrm{R}}{dt} = -k^z_{\mathrm{R}\to\mathrm{P}} N_\mathrm{R} + k^z_{\mathrm{P}\to\mathrm{R}} N_\mathrm{P}, \tag{2.23}$$

where $k^z_{\mathrm{R}\to\mathrm{P}}$ and $k^z_{\mathrm{P}\to R}$ ($z = \mathrm{IR}, \mathrm{cond}$) are the rate constants for the forward and backward reactions, respectively, which are themselves functions of N_R and N_P when $g_\mathrm{R} \neq g_\mathrm{P}$. We find the steady state solution $N^{\mathrm{ss}}_\mathrm{R}$ from this equation and compute the reaction yield $N^{\mathrm{ss}}_\mathrm{P}/N$.

The difference in yield between the condensate and bare case is particularly large when $\lambda_\mathrm{S} \ll \hbar\omega_\mathrm{vib} < |\Delta G|$ (see Fig. 2.4c-d for symmetric coupling $g_\mathrm{R} = g_\mathrm{P}$). To understand the underlying reason, we define the dominant channel f_min as the one with minimum activation barrier outside of the cavity.

$$\frac{1}{k_\mathrm{B}T}\frac{dE^\ddagger_f}{df} = \frac{\hbar\omega_\mathrm{vib}}{k_\mathrm{B}T}\left(\frac{\Delta G + \lambda_\mathrm{S} + f\hbar\omega_\mathrm{vib}}{2\lambda_\mathrm{S}}\right) \tag{2.24}$$

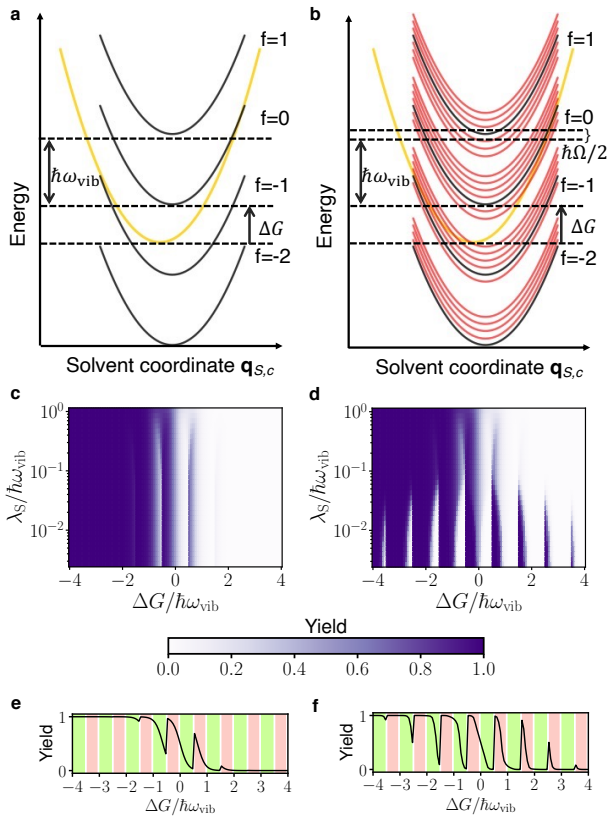

Figure 2.4. Potential energy surfaces (not to scale) and reaction yield. a, c, e are results for a laser driven system without light-matter strong coupling (SC) and b, d, f are for the same system under SC and 2.4% of the population in the lower polariton (condensation). All these plots are for symmetric light-matter coupling $g_{\rm R} = g_{\rm P}$. a, b For a clearer qualitative picture, we plot the PESs under zero detuning $\Delta = 0$. Initial (yellow) and final (black) PESs for a molecule undergoing the forward reaction with solvent coordinate $\mathbf{q}_{\rm S,c}$. While the energy separation between black PESs is $\hbar\omega_{\rm vib}$, the condensate provides many additional final PESs (red, separated by $\hbar\Omega/2$ at resonance). c Reaction yield $N_{\rm P}^{\rm ss}/N$ at temperature $k_{\rm B}T = 0.1389\hbar\omega_{\rm vib}$ ($T = 298$K when $\hbar\omega_{\rm vib} = 185$ meV), Huang-Rhys factor $S = 3.5$, and average occupation of the intramolecular vibrational mode $\bar{n} = 0.08$. d Reaction yield $N_{\rm P}^{\rm ss}/N$ with $\Delta = -0.0695\omega_{\rm vib}$, $2g_{\rm R}\sqrt{N} = 2g_{\rm P}\sqrt{N} = 0.1\omega_{\rm vib}$, $P_- = 0.08N\Gamma_\downarrow$, $N = 10^7$, temperature and Huang-Rhys factor are the same as c. The contributions of the red PESs through the condensate provide a broader tunability of reaction yields with respect to ΔG than under laser driving without SC. Notice that originally endergonic (exergonic) reactions in the absence of optical pumping can become exergonic (endergonic) under the featured nonequilibrium conditions. e, f A cross-section of plot (c-d) when $\lambda_{\rm S} = 10^{-2}\hbar\omega_{\rm vib}$. The pink shaded regions correspond to cases where the dominant forward (backward) channel is in the inverted (normal) regime; the opposite is true for the green shaded regions. The condensate amplifies the forward (backward) reaction in the pink (green) shaded regions.

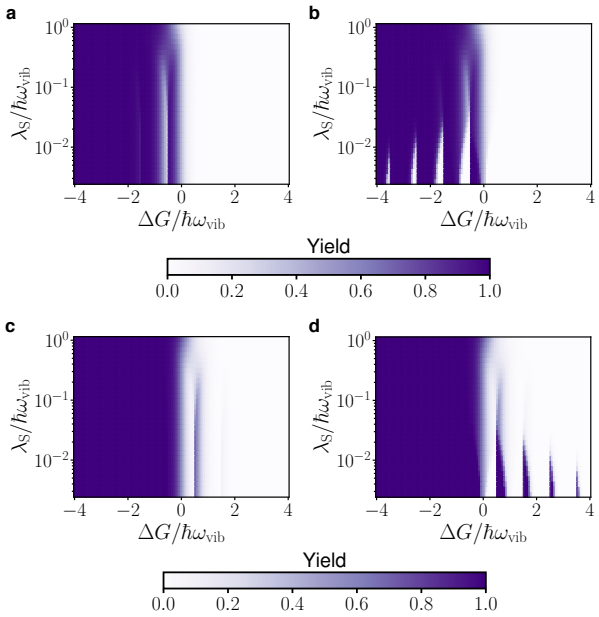

Figure 2.5. Reaction yield for asymmetric light-matter coupling. a (c) The yield of the reaction when only the product (reactant) weakly couples with light. b (d) Analogous plots under strong coupling $2g_P\sqrt{N} = 0.1\omega_{vib}$, $g_R = 0$ ($g_P = 0$, $2g_R\sqrt{N} = 0.1\omega_{vib}$). We use parameters $\Delta = -0.0695\omega_{vib}$, $k_BT = 0.1389\hbar\omega_{vib}$ ($T = 298$K when $\hbar\omega_{vib} = 185$ meV), $S = 3.5$, $P_- = 0.08N\Gamma_\downarrow$ and $N = 10^7$. We assume the same scattering parameters W_{ij} and decay rates $\Gamma_\downarrow$, κ as in Fig. 2.2.

Setting the derivative in Eq. (2.24) equal to zero and taking into account the discrete nature of f, we find the dominant channel, $f_{\min} = \left\lceil \frac{-\Delta G - \lambda_S}{\hbar\omega_{vib}} \right\rceil$ or $\left\lfloor \frac{-\Delta G - \lambda_S}{\hbar\omega_{vib}} \right\rfloor$. When $\lambda_S \ll \hbar\omega_{vib}, |\Delta G|$, this channel contributes most to the rate constant because $\frac{1}{k_B T}\left|\frac{dE_f^\ddagger}{df}\right| \gg 1$. We define Marcus normal $\left.\frac{dE_f^\ddagger}{df}\right|_{f_{\min}} > 0$ and inverted $\left.\frac{dE_f^\ddagger}{df}\right|_{f_{\min}} < 0$ regimes with respect to the dominant channel. If the dominant forward channel is in the inverted regime, the dominant backward channel (which can be found by replacing $\Delta G \to -\Delta G$ in Eq. (2.24)) will be in the normal regime when $\lambda_S \ll \hbar\omega_{vib}, |\Delta G|$.

In Fig. 2.4d, we see periodic yield modification in ΔG with period $\sim \hbar\omega_{vib}$, which decays for large $\Delta G/\hbar\omega_{vib}$ due to concomitant decline in FC factor for large changes in the number of vibrational quanta between the initial and final states. Outside of the cavity, we only see the first fringe (Fig. 2.4c). To observe the full periodic structure in yield, we need large occupation of higher vibrational states which requires very large pumping rates outside of the cavity. However, under polariton condensation, the macroscopic population of the lower polariton enables these interesting periodic features to be observed at room temperature with experimentally attainable pumping rates. Additionally, polariton condensation not only modifies the reaction yield under symmetric light-matter coupling strengths, as seen in Fig. 2.4, it also changes the yield when the reactant and product asymmetrically couple with light (Fig. 2.5).

Condensation provides many additional channels for the forward and backward reactions (separated by $\sim \hbar\Omega/2$, see red curves in Fig. 2.4b, showing only the forward channels at resonance $\Delta = 0$) due to transfer of quanta between the polariton and dark modes during the reaction. Condensation speeds up the reaction when the dominant channel is either in the inverted or in the normal regime (Fig. 2.6b). This is the case because there are additional channels with energy both higher (benefiting the inverted regime) and lower (benefiting the normal regime) than the dominant channel (see red curves in Fig. 2.4b). Apart from reduced activation energy, the additional channels provided by the condensate also have large enough FC factors to affect the rate constant. Reaction channels that involve changes in the number of quanta in the LP during

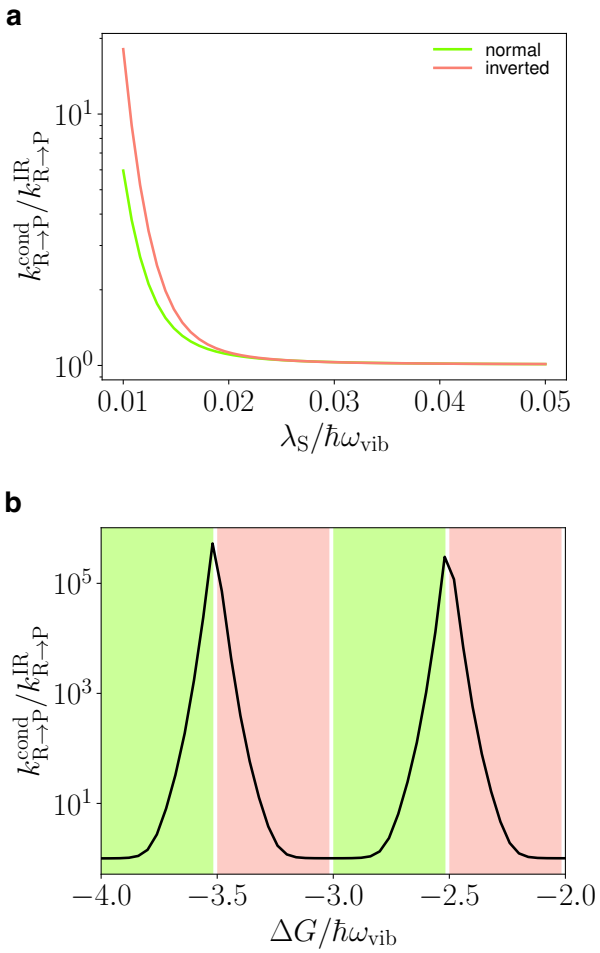

Figure 2.6. Rate constant. Ratio of the rate constants inside $k^{\mathrm{cond}}_{\mathrm{R}\to\mathrm{P}}$ and outside $k^{\mathrm{IR}}_{\mathrm{R}\to\mathrm{P}}$ of the cavity under laser excitation with $\Delta = -0.0695\omega_{\mathrm{vib}}$, $k_{\mathrm{B}}T = 0.1389\hbar\omega_{\mathrm{vib}}$ ($T = 298$K when $\hbar\omega_{\mathrm{vib}} = 185$ meV), $S = 3.5$, $2g\sqrt{N} = 0.1\omega_{\mathrm{vib}}$, $P_- = 0.08N\Gamma_\downarrow$ and $N = 10^7$ for symmetric coupling $g_{\mathrm{R}} = g_{\mathrm{P}} = g$. a Relative rate constant as a function of reorganization energy, λ_{S}, with $\Delta G = -3.33\hbar\omega_{\mathrm{vib}}$ (the pink curve; here, the dominant channel lies in the inverted regime) and $\Delta G = -3.73\hbar\omega_{\mathrm{vib}}$ (the green curve; here, the dominant channel lies in the normal regime) and b as a function of ΔG with $\lambda_{\mathrm{S}} = 10^{-2}\hbar\omega_{\mathrm{vib}}$. Here, the pink region corresponds to the dominant channel in the inverted regime and the green to the normal regime.

the reaction have significantly larger FC factors ($\sim 10^{20}$ times) under condensation $N_- = 0.1N$ than without any pumping $N_- = 0$ (Fig. S1 in the supplementary information compares them). Changes in the rate constant as a function of λ_S (Fig. 2.6a) and ΔG (Fig. 2.6b) are large for small $\lambda_S/\hbar\omega_{vib}$ and when $\Delta G/\hbar\omega_{vib} = n/2$ where n is an odd integer since activation energy effects are large for these set of parameters.

2.3 Discussion

Our result is a first step towards understanding the effect of Bose-Einstein condensation of polaritons on chemical reactivity. We demonstrate this effect using a simple electron transfer model (MLJ) with molecular vibrations strongly coupled to light. In particular, we show that one can counteract the massive degeneracy of dark modes and enhance polaritonic effects by having a macroscopic occupation of the lower polariton mode *i.e.*, Bose-Einstein condensation. Our results indicate that the latter is feasible for experimentally realizable pump powers and Rabi splittings, despite the close proximity in energy of the dark state manifold with $\hbar\Omega \sim k_B T$. These results can guide the choice of suitable materials for condensation under VSC. While laser driving without SC modifies the reaction yield, this change is amplified by the condensate, due to the availability of many additional reactive channels that differ in energy by $\sim \hbar\Omega/2$ rather than $\sim \hbar\omega_{vib}$. For a wide range of parameters, we find that this leads to a periodic dependence of reaction yield as a function of ΔG (with period $\sim \hbar\omega_{vib}$), rendering a set of originally endergonic reactions exergonic, and vice versa. These effects are substantially weaker under laser driving, and highlight both the energetic (availability of additional channels with lower activation energy) and entropic (redistribution of vibrational energy from the condensate into the polariton and dark modes upon reaction) advantages of exploiting polariton condensates for reactivity. To summarize, vibrational polariton condensation offers a novel strategy to accumulate energy into a well defined normal mode, a holy-grail in the field of vibrational dynamics that has been historically hindered by IVR. Its successful demonstration could revive hopes of "mode selective

chemistry" [61], beyond electron transfer processes. In future work, it will be interesting to explore how the studied phenomena generalize to molecular polariton condensates in different spectral ranges.

Chapter 2, in full, is adapted from the material as it appears in "Driving chemical reactions with polariton condensates," S. Pannir-Sivajothi, J. A. Campos-Gonzalez-Angulo, L. A. Martínez-Martínez, S. Sinha, J. Yuen-Zhou, *Nat. Commun.* **13**, 1–9 (2022) [11]. The dissertation author was the primary investigator and author of this paper.

Chapter 3

Molecular and solid-state topological polaritons induced by population imbalance

3.1 Introduction

Exciton-polaritons are hybrid excitations that exist in systems where photonic modes couple strongly with optical transitions in materials and their coupling strength exceeds losses [3]. Electronic strong coupling (ESC), where the optical transitions correspond to semiconductor excitons or molecular electronic transitions, has been observed in a wide variety of inorganic and organic materials. While some polariton systems, such as GaAs and CdTe quantum wells in microcavities [3, 62], often require cryogenic temperatures for operation, due to their small exciton binding energies, organic materials [1] along with others such as GaN [4], ZnO [63], perovskites [10, 64], and transition metal dichalcogenides (TMD) [5, 65] can achieve ESC at room temperature when placed in Fabry-Perot cavities. In particular, organic exciton-polaritons have received attention for their ability to modify chemical reactivity [66], demonstrate polariton condensation at room temperature [26, 28], improve photoconductivity [67], and display topological properties [68, 69].

Exciton-polariton systems are versatile platforms for topological applications as their hybrid nature provides the unique opportunity to take advantage of the nonlinearities and magnetic response of the material component while still enjoying benefits of the coherence properties of the photonic part [70–72]. In the presence of photonic lattices, they also offer the possibility of

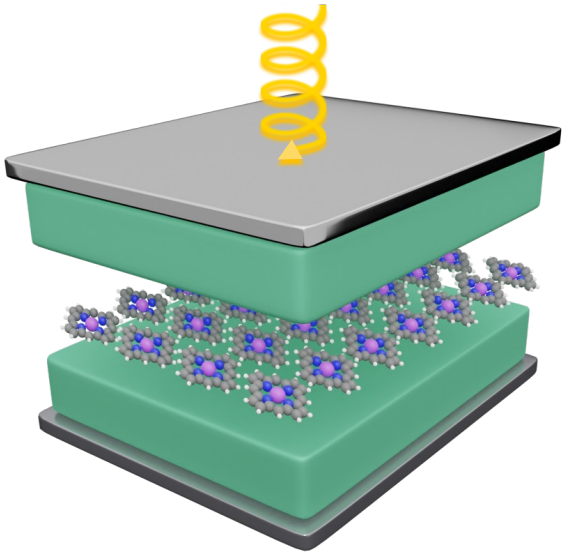

Figure 3.1. Illustration of the system under study. Porphyrin (molecules at the center) and perylene (green blocks) placed within a Fabry-Perot cavity and pumped with circularly polarized light.

unidirectional transport of energy through edge states that are robust to disorder [73]. A few approaches are frequently used to achieve topological exciton-polariton bands. In one of the approaches, the non-trivial topology resides in the winding light-matter coupling rather than individual photon or exciton components [73, 74]. However, it is limited in application due to the requirement of large magnetic fields to break time-reversal symmetry (TRS) and low temperatures to achieve Zeeman splitting in the exciton component which exceeds the exciton linewidth. In another approach, TRS is preserved and a quantum spin hall insulator analogue is created in a polariton system [75]. This approach does not require a large magnetic field, however, there, a topological polariton system is created by coupling a topologically non-trivial photonic lattice with a topologically trivial exciton system and the interesting topology is almost entirely encoded in the photonic component of the polariton [75, 76]. Both the approaches mentioned above were experimentally realized in polariton lattices. More recently, polaritons in Fabry-Perot cavities have emerged as a viable platform for topological polaritonics. Several experiments have demonstrated measurement and control of the Berry curvature of exciton-polariton and photon bands in these systems [77–80]. Our work will focus on these Fabry-Perot cavity systems.

In this work, we theoretically propose a scheme for generating topological polaritons that combines advantages of both the approaches mentioned above. Specifically, we exploit the primary nonlinearity of organic exciton-polaritons, saturation [26], to achieve this. Here, the light-matter coupling contains the non-trivial topology instead of the individual photon or exciton components and optical pumping with circularly polarized light breaks TRS instead of a large magnetic field.

Breaking TRS in a system using the helicity of light is an idea that has been demonstrated in several other contexts; it has been used to achieve all-optical non-reciprocity [81, 82] and theoretical results suggest that it can also induce optical-activity in achiral molecules [83]. Additionally, a similar idea that relies on breaking TRS using circularly polarized light has been previously proposed for polariton lattices by Bleu *et al.* [84].

We focus on the topological properties of polaritons formed by the coupling of Frenkel excitons hosted in organic semiconductors with photon modes in a Fabry-Perot cavity. Here, optical pumping with circularly polarized light saturates certain electronic transitions and breaks TRS in the system; this results in non-zero Chern numbers of polariton bands. Our scheme relies on the contraction of Rabi splitting due to saturation, and we find modified Berry curvature and Chern number of the bands under circularly polarized pumping. The Berry curvature of the more photonic sections of the bands computed in our work can be experimentally measured using pump-probe spectroscopy. Furthermore, the applicability of our scheme is not limited to organic polariton systems. It only requires certain key ingredients: transitions that can be selectively excited with circularly polarized light, saturation effects, and Rabi splitting contraction. To highlight this, we compute the Berry curvature of two other systems under strong coupling and optical pumping: (a) Ce:YAG and (b) monolayer MoS_2. Our work provides a viable strategy to induce non-reciprocal behavior in standard microcavity polaritons, leading to the optical tuning of isolators and circulators [81], as well as fabrication of elliptically-polarized lasers and condensates [85].

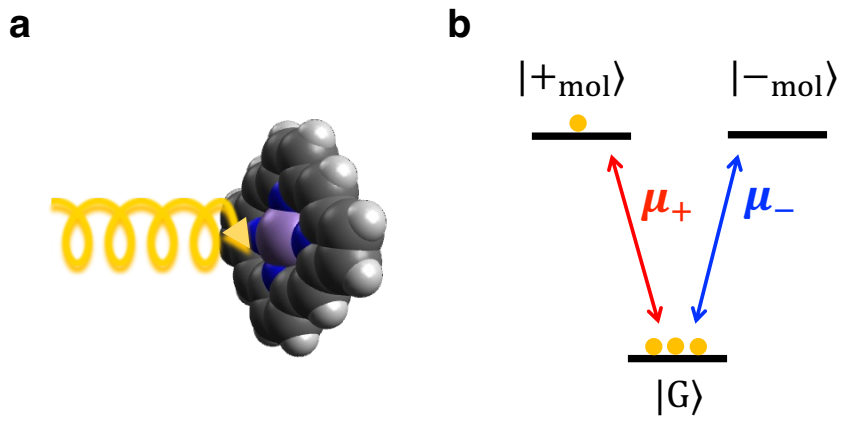

Figure 3.2. Three-level model of a metalloporphyrin molecule. (a) Illustration of circularly polarized light exciting a metalloporphyrin molecule. (b) Three-level model of porphyrin with a ground state $|\mathrm{G}\rangle$ and two degenerate excited states $|+_{\mathrm{mol}}\rangle, |-_{\mathrm{mol}}\rangle$. The transition dipole moment for a transition from $|\mathrm{G}\rangle$ to $|\pm_{\mathrm{mol}}\rangle$ is $\boldsymbol{\mu}_\pm = \mu_0(\hat{\mathbf{x}} \pm i\hat{\mathbf{y}})/\sqrt{2}$. The number of yellow circles at each state represents the fraction of molecules in that state. Here, the ratio of the fraction of molecules in the ground, f_{G}, and $|\pm_{\mathrm{mol}}\rangle$ excited states, $f_\pm$, is $f_{\mathrm{G}} : f_+ : f_- = 3 : 1 : 0$. Such population ratios can be achieved through pumping with circularly polarized light.

3.2 Results

3.2.1 Model

In our theoretical study, we consider a Fabry-Perot cavity containing a thin film of porphyrin molecules at the center and a bulk perylene crystal filling the rest of the volume (Fig. 3.1). The porphyrin and perylene molecules are not treated on an equal footing in our model; while the molecular transitions of porphyrin are considered explicitly in the Hamiltonian, those of the perylene crystal are not, and they can be accounted for through effective cavity modes [79]. This is a valid approximation because we focus on photon modes with frequencies close to those of electronic transitions in porphyrin (~ 3.81eV) [86, 87] and far off-resonant from the transitions of perylene (~ 2.98eV) [88]. Here, the birefringent perylene crystal plays the role of providing anisotropy and emergent optical activity to the cavity modes [79].

We model each porphyrin molecule as a three-level electronic system with a ground state $|\mathrm{G}\rangle$ and two excited states $|+_{\mathrm{mol}}\rangle$ and $|-_{\mathrm{mol}}\rangle$ (see Fig. 3.2b) [89, 90]. In the absence of a magnetic field, the two excited states are degenerate and the energy difference between the

ground and excited states is $\hbar\omega_e = 3.81$eV [91]. The transition dipole moments for transitions from $|G\rangle$ to $|+_{mol}\rangle$ and $|-_{mol}\rangle$ are $\boldsymbol{\mu}_+ = \mu_0(\hat{\mathbf{x}} + i\hat{\mathbf{y}})/\sqrt{2}$ and $\boldsymbol{\mu}_- = \mu_0(\hat{\mathbf{x}} - i\hat{\mathbf{y}})/\sqrt{2}$, respectively, with $\mu_0 = 2.84$D [91]. Here, $\hat{\mathbf{x}}$ and $\hat{\mathbf{y}}$ are unit vectors along the x and y directions. Using circular polarized light, the $|+_{mol}\rangle$ or $|-_{mol}\rangle$ states can be selectively excited.

In our model, we consider a thin film of metalloporphyrins or metallophtalocyanines arranged in a square lattice with nearest neighbor spacing a. The choice of lattice is irrelevant because later we will take the continuum limit $a \to 0$ as we are only interested in length scales much larger than the intermolecular spacing. Additionally, we use periodic boundary conditions along the x and y directions and consider a box of size $L_x \times L_y$. Each molecule is labeled with the index $\mathbf{m} = (m_x, m_y)$ that specifies its location in a $N_x \times N_y$ array of molecules where $L_{x/y} = aN_{x/y}$; here, the molecule's position is given by $\mathbf{r}_\mathbf{m} = m_x a\hat{\mathbf{x}} + m_y a\hat{\mathbf{y}}$. States of the $\mathbf{m}^{\text{th}}$ molecule are then written as $|\mathbf{m}, G\rangle$, $|\mathbf{m}, +_{mol}\rangle$ and $|\mathbf{m}, -_{mol}\rangle$. The creation operator $\hat{\sigma}^\dagger_{\mathbf{m},\pm} = |\mathbf{m}, \pm_{mol}\rangle\langle\mathbf{m}, G| \otimes_{\mathbf{n}\neq\mathbf{m}} \mathbb{I}_\mathbf{n}$ excites the $\mathbf{m}^{\text{th}}$ molecule from $|\mathbf{m}, G\rangle$ to $|\mathbf{m}, \pm_{mol}\rangle$. Here, $\mathbb{I}_\mathbf{n} = |\mathbf{n}, G\rangle\langle\mathbf{n}, G| + |\mathbf{n}, +_{mol}\rangle\langle\mathbf{n}, +_{mol}| + |\mathbf{n}, -_{mol}\rangle\langle\mathbf{n}, -_{mol}|$ is the identity operator for $\mathbf{n}^{\text{th}}$ molecule. These molecular operators satisfy commutation relations (a generalization of the commutation relations of paulion operators [92, 93]),

$$\left[\hat{\sigma}_{\mathbf{n},\pm}, \hat{\sigma}^\dagger_{\mathbf{m},\pm}\right] = \delta_{\mathbf{m},\mathbf{n}}(1 - \hat{\sigma}^\dagger_{\mathbf{n},\mp}\hat{\sigma}_{\mathbf{n},\mp} - 2\hat{\sigma}^\dagger_{\mathbf{n},\pm}\hat{\sigma}_{\mathbf{n},\pm}). \tag{3.1}$$

We model the effective photon modes of a Fabry-Perot cavity filled with perylene as in Ren *et al*. [79] For the photon modes of a Fabry-Perot cavity, the component of wave vector orthogonal to the mirrors $k_z = 2n_z\pi/L_z$ is quantized, where L_z is the effective distance between the mirrors of the cavity and n_z is the mode index [94]. For a given n_z, the modes are labeled by the in-plane wave vector $\mathbf{k} = k_x\hat{\mathbf{x}} + k_y\hat{\mathbf{y}}$ and polarization α; the creation operators associated with these modes are $\hat{a}^\dagger_{\mathbf{k},\alpha}$ and they satisfy bosonic commutation relations $\left[\hat{a}_{\mathbf{k},\alpha}, \hat{a}^\dagger_{\mathbf{k}',\alpha'}\right] = \delta_{\alpha,\alpha'}\delta_{\mathbf{k},\mathbf{k}'}$. As a result of in-plane translational invariance of the cavity and periodic boundary conditions along the x and y directions, $k_x = 2l_x\pi/L_x$ and $k_y = 2l_y\pi/L_y$ take a discrete but infinite set of

values $l_x, l_y \in \mathbb{Z}$. Throughout this work, we specify the cavity mode polarization in the circularly polarized basis $\alpha = \pm$.

The Hamiltonian of the full system is

$$\hat{H} = \hat{H}_{\text{mol}} + \hat{H}_{\text{cav}} + \hat{H}_{\text{cav-mol}}, \tag{3.2}$$

where

$$\begin{aligned}
\hat{H}_{\text{mol}} &= \sum_{\mathbf{m}} \left(\hbar\omega_{\text{e}} \hat{\sigma}^{\dagger}_{\mathbf{m},+} \hat{\sigma}_{\mathbf{m},+} + \hbar\omega_{\text{e}} \hat{\sigma}^{\dagger}_{\mathbf{m},-} \hat{\sigma}_{\mathbf{m},-} \right) \\
\hat{H}_{\text{cav}} &= \sum_{\mathbf{k}} \Bigg[\left(E_0 + \frac{\hbar^2 |\mathbf{k}|^2}{2m^*} + \zeta |\mathbf{k}| \cos\phi \right) \hat{a}^{\dagger}_{\mathbf{k},+} \hat{a}_{\mathbf{k},+} \\
&\quad + \left(E_0 + \frac{\hbar^2 |\mathbf{k}|^2}{2m^*} - \zeta |\mathbf{k}| \cos\phi \right) \hat{a}^{\dagger}_{\mathbf{k},-} \hat{a}_{\mathbf{k},-} \\
&\quad + \left(-\beta_0 + \beta |\mathbf{k}|^2 e^{-i2\phi} \right) \hat{a}^{\dagger}_{\mathbf{k},+} \hat{a}_{\mathbf{k},-} \\
&\quad + \left(-\beta_0 + \beta |\mathbf{k}|^2 e^{i2\phi} \right) \hat{a}^{\dagger}_{\mathbf{k},-} \hat{a}_{\mathbf{k},+} \Bigg], \\
\hat{H}_{\text{cav-mol}} &= \sum_{\mathbf{m}} \sum_{\mathbf{k},\alpha} -\hat{\boldsymbol{\mu}}_{\mathbf{m}} \cdot \hat{\mathbf{E}}_{\mathbf{k},\alpha}(\mathbf{r}_{\mathbf{m}}, 0) \\
&\approx \sum_{\mathbf{m}} \sum_{\mathbf{k}} \frac{e^{i\mathbf{k}\cdot\mathbf{r}_{\mathbf{m}}}}{\sqrt{N_x N_y}} \Bigg[(\boldsymbol{\mu}_+ \cdot \mathbf{J}_{\mathbf{k},+}) \hat{\sigma}^{\dagger}_{\mathbf{m},+} \hat{a}_{\mathbf{k},+} \\
&\quad + (\boldsymbol{\mu}_- \cdot \mathbf{J}_{\mathbf{k},+}) \hat{\sigma}^{\dagger}_{\mathbf{m},-} \hat{a}_{\mathbf{k},+} + (\boldsymbol{\mu}_+ \cdot \mathbf{J}_{\mathbf{k},-}) \hat{\sigma}^{\dagger}_{\mathbf{m},+} \hat{a}_{\mathbf{k},-} \\
&\quad + (\boldsymbol{\mu}_- \cdot \mathbf{J}_{\mathbf{k},-}) \hat{\sigma}^{\dagger}_{\mathbf{m},-} \hat{a}_{\mathbf{k},-} \Bigg] + \text{H.c.}
\end{aligned} \tag{3.3}$$

Above, $\hat{H}_{\text{mol}}$ describes the porphyrin molecules, $\hat{H}_{\text{cav}}$ the effective cavity modes (including contributions from the perylene crystal), and $\hat{H}_{\text{cav-mol}}$ the coupling between the porphyrin molecules and effective cavity modes. Here, ϕ is the angle between the in-plane wave vector and the x-axis, *i.e.*, $\cos\phi = k_x/|\mathbf{k}|$. Within $\hat{H}_{\text{cav}}$, β specifies the TE-TM splitting, β_0 quantifies the linear birefringence of the perylene crystal which splits the H-V modes, and ζ describes the emergent optical activity [79]. Additionally, E_0 is the frequency of the cavity modes at $|\mathbf{k}| = 0$ in the absence of the perylene crystal ($\beta_0 = 0$ and $\zeta = 0$), and m^* is the effective mass of the photons

in the absence of perylene ($\beta_0 = 0$ and $\zeta = 0$) and TE-TM splitting ($\beta = 0$). We have made the electric dipole approximation and the rotating-wave approximation in $\hat{H}_{\text{cav-mol}}$. Here, $\hat{\boldsymbol{\mu}}_{\mathbf{m}}$ is the electric dipole operator associated with the $\mathbf{m}^{\text{th}}$ molecule and $\hat{\mathbf{E}}_{\mathbf{k},\alpha}(\mathbf{r}, z)$ is the electric field operator of the mode with polarization α and in-plane wave vector $\mathbf{k}$. In addition, $\boldsymbol{\mu}_{\alpha'} \cdot \mathbf{J}_{\mathbf{k},\alpha}$ is the collective coupling strength of the cavity mode labeled by $\mathbf{k}, \alpha$ and the $|\text{G}\rangle$ to $\left|\alpha'_{\text{mol}}\right\rangle$ transition of the molecules (see Section S1 in Supporting Information). In the Hamiltonian, we only include cavity modes with $\mathbf{k}$ that lies within the first Brillouin zone determined by the porphyrin lattice $-\pi/a < k_x, k_y < \pi/a$. We ignore cavity modes with larger wavevectors (Umklapp terms) as they are off-resonant and would have a negligible effect on the bands of our interest.

The photon modes of an empty cavity experience TE-TM splitting due to polarization dependent reflection from the mirrors [95]. While the TE-TM splitting lifts the degeneracy between photon modes at $|\mathbf{k}| \neq 0$, photon modes of both polarizations remain degenerate at $|\mathbf{k}| = 0$ due to rotational symmetry of the cavity mirrors about the z-axis. However, for Berry curvature and Chern invariant to be well-defined, we need the photon/polariton bands to be separated in energy at all $\mathbf{k}$; to achieve this, we include the perylene crystal. The anisotropy and emergent optical activity of the perylene crystal lifts the degeneracy between the photon modes at all $\mathbf{k}$ [79].

To compute the Berry curvature and Chern number, we focus on the first excitation manifold which is spanned by states $|\mathbf{m}, \pm_{\text{mol}}\rangle = \hat{\sigma}^{\dagger}_{\mathbf{m},\pm} |\text{vac}\rangle$ and $|\mathbf{k}, \pm_{\text{cav}}\rangle = \hat{a}^{\dagger}_{\mathbf{k},\pm} |\text{vac}\rangle$. Here, $|\text{vac}\rangle$ is the absolute ground state of the system where the photon modes are empty and all molecules are in their ground states. Rewriting the Hamiltonian with operators $\hat{\sigma}_{\mathbf{k},\alpha}$, where $\hat{\sigma}_{\mathbf{m},\alpha} = \frac{1}{\sqrt{N_x N_y}} \sum_{\mathbf{k}\in\text{BZ}} e^{i\mathbf{k}\cdot\mathbf{r}_{\mathbf{m}}} \hat{\sigma}_{\mathbf{k},\alpha}$ and restricting ourselves to the first excitation manifold, we find $\hat{H}(\mathbf{k}) = \langle \mathbf{k}| \hat{H} |\mathbf{k}\rangle$ to be

$$\hat{H}(\mathbf{k}) = \hat{H}_{\text{mol}}(\mathbf{k}) + \hat{H}_{\text{cav}}(\mathbf{k}) + \hat{H}_{\text{cav-mol}}(\mathbf{k}), \tag{3.4}$$

where,

$$
\begin{aligned}
\hat{H}_{\mathrm{mol}}(\mathbf{k}) =& \hbar\omega_{\mathrm{e}} \left|+_{\mathrm{mol}}\right\rangle \left\langle+_{\mathrm{mol}}\right| + \hbar\omega_{\mathrm{e}} \left|-_{\mathrm{mol}}\right\rangle \left\langle-_{\mathrm{mol}}\right|, \\
\hat{H}_{\mathrm{cav}}(\mathbf{k}) =& \left(E_0 + \frac{\hbar^2|\mathbf{k}|^2}{2m^*} + \zeta|\mathbf{k}|\cos\phi\right) \left|+_{\mathrm{cav}}\right\rangle \left\langle+_{\mathrm{cav}}\right| \\
&+ \left(E_0 + \frac{\hbar^2|\mathbf{k}|^2}{2m^*} - \zeta|\mathbf{k}|\cos\phi\right) \left|-_{\mathrm{cav}}\right\rangle \left\langle-_{\mathrm{cav}}\right| \\
&+ \left(-\beta_0 + \beta|\mathbf{k}|^2 e^{-i2\phi}\right) \left|+_{\mathrm{cav}}\right\rangle \left\langle-_{\mathrm{cav}}\right| \\
&+ \left(-\beta_0 + \beta|\mathbf{k}|^2 e^{i2\phi}\right) \left|-_{\mathrm{cav}}\right\rangle \left\langle+_{\mathrm{cav}}\right|, \\
\hat{H}_{\mathrm{cav-mol}}(\mathbf{k}) =& \mathbf{J}_{\mathbf{k},+} \cdot \left(\boldsymbol{\mu}_+ \left|+_{\mathrm{mol}}\right\rangle + \boldsymbol{\mu}_- \left|-_{\mathrm{mol}}\right\rangle\right) \left\langle+_{\mathrm{cav}}\right| \\
&+ \mathbf{J}_{\mathbf{k},-} \cdot \left(\boldsymbol{\mu}_+ \left|+_{\mathrm{mol}}\right\rangle + \boldsymbol{\mu}_- \left|-_{\mathrm{mol}}\right\rangle\right) \left\langle-_{\mathrm{cav}}\right| \\
&+ \mathrm{H.c.}
\end{aligned}
\tag{3.5}
$$

Here, $\mathbf{k}$ lies within the first Brillouin zone determined by the porphyrin lattice $k_x, k_y \in [-\pi/a, \pi/a]$. As we are only interested in length scales much larger than a, we take the continuum limit $a \to 0$ while keeping μ_0/a a constant. Therefore, terms such as the collective light-matter coupling strength, $\mathbf{J}_{\mathbf{k},\alpha} \cdot \boldsymbol{\mu}_{\alpha'}$, remain constant in this limit (see Section S1 in Supporting Information). Moreover, upon taking the continuum limit, $\hat{H}(\mathbf{k})$ does not change; only the range of $\mathbf{k}$ becomes infinitely large, $k_x, k_y \in \mathbb{R}$, that is, our system acquires complete translational invariance in the x-y plane. For such continuous systems, since $k_x, k_y \in \mathbb{R}$ is unbounded, we need to map (k_x, k_y) onto a sphere which is a closed and bounded surface using stereographic projection before we compute Chern numbers [96] (see Section S2 in Supporting Information).

When we diagonalize the Hamiltonian in Eq. 3.5, we obtain four bands which we label with $l = 1, 2, 3, 4$ in increasing order of energy. In Fig. 3.3a we plot the Berry curvature, $\Omega_1(\mathbf{k})$, of the lowest band $l = 1$, and in Fig. 3.3e we plot the $k_y = 0$ slice of the band structure of the two bands lowest in energy, $l = 1, 2$. As expected, in the absence of optical pumping, this system preserves TRS, which can be verified using the condition on Berry curvature $\Omega_l(\mathbf{k}) = -\Omega_l(-\mathbf{k})$, and the Chern numbers of the all the bands $C_l = 0$. Also, note that, the smallest splitting between

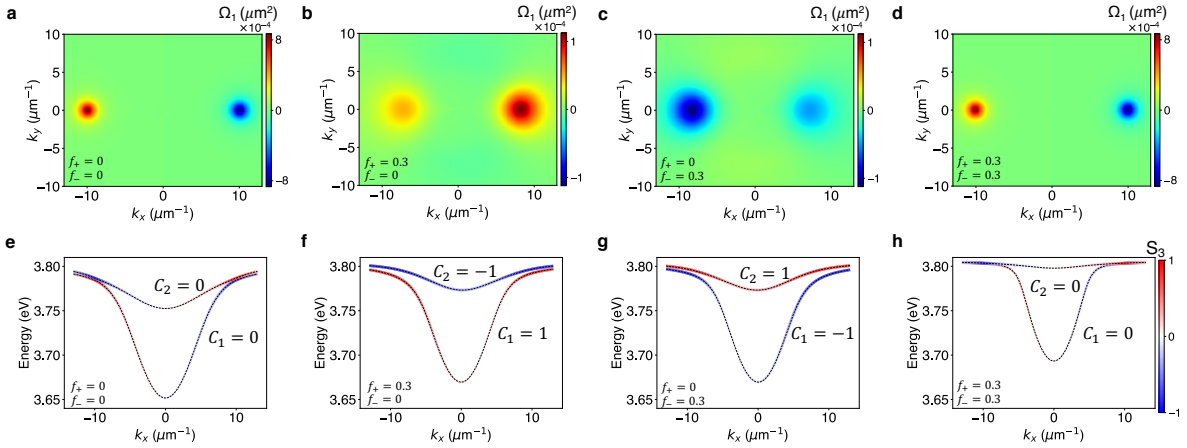

Figure 3.3. Berry curvature and degree of circular polarization of the bands. (a-d) Berry curvature of the lowest energy band, $\Omega_1(\mathbf{k})$, and (e-h) a slice of the band structure at $k_y = 0$ of the lower two bands, under different levels of optical pumping which create populations: (a,e) $f_+ = f_- = 0$, (b,f) $f_+ = 0.3$, $f_- = 0$, (c,g) $f_+ = 0$, $f_- = 0.3$, and (d,h) $f_+ = f_- = 0.3$. (e-h) The colors of the band indicate the value of the Stokes parameter, $S_3(\mathbf{k})$, which measures the degree of circular polarization of a mode (Eq. 3.8). The Chern numbers C_1 and C_2 of the bands are also specified and are non-zero under time-reversal symmetry (TRS) breaking, that is, when $f_+ \neq f_-$. We used parameters $\beta_0 = 0.1$eV, $\beta = 9 \times 10^{-4}$eVμm^2, $\zeta = 2.5 \times 10^{-3}eV\mu$m, $m^* = 125\hbar^2$eV$^{-1}\mu$m^{-2}, $E_0 = 3.80$eV and $\hbar\omega_e = 3.81$eV (see Section S4 in Supporting Information for details).

the lower two bands within $-13\mu\text{m}^{-1} < k_x, k_y < 13\mu\text{m}^{-1}$ is ~ 2.8meV which is larger than the linewidth of the transition in porphyrin at 4K (~ 0.5meV) [97, 98].

3.2.2 Optical pumping

Optical pumping can saturate the electronic transitions of a system. This leads to reduction in the effective light-matter coupling strength, and, therefore, Rabi splitting contraction [26, 99, 100]. For instance, when the pump excites a fraction of molecules, f_E, to the excited state and the remaining population stays in the ground state, f_G, it results in Rabi splitting contraction proportional to $\sqrt{f_G - f_E} = \sqrt{1 - 2f_E}$ [101].

In our system, when the molecules are optically pumped, a fraction, f_+, of the molecules occupy the $|+_{\text{mol}}\rangle$ state, another fraction, f_-, occupy the $|-_{\text{mol}}\rangle$ state, and the remaining fraction, f_G, are in the ground state $|G\rangle$. The Rabi contraction corresponding to the $|G\rangle$ to $|+_{\text{mol}}\rangle$ transition should then be proportional to $\sqrt{f_G - f_+}$ which equals $\sqrt{1 - f_- - 2f_+}$ since $f_G + f_+ + f_- = 1$.

Similarly, the contraction should be proportional to $\sqrt{1 - f_+ - 2f_-}$ for the $|\mathrm{G}\rangle$ to $|{-_{\mathrm{mol}}}\rangle$ transition. This difference in light-matter coupling when $f_+ \neq f_-$ effectively introduces 2D chirality into the system [102].

To derive an effective Hamiltonian under optical pumping, we use Heisenberg equations of motion and make a mean-field approximation following the approach of Ribeiro *et al.* [101] (see Section S3 in Supporting Information). We then obtain the effective Hamiltonian,

$$\hat{H}^{\mathrm{eff}}(\mathbf{k}) = \hat{H}^{\mathrm{eff}}_{\mathrm{mol}}(\mathbf{k}) + \hat{H}^{\mathrm{eff}}_{\mathrm{cav}}(\mathbf{k}) + \hat{H}^{\mathrm{eff}}_{\mathrm{cav-mol}}(\mathbf{k}), \tag{3.6}$$

where,

$$\begin{aligned}
\hat{H}^{\mathrm{eff}}_{\mathrm{mol}}(\mathbf{k}) =& \hbar\omega_{\mathrm{e}} \left|{+_{\mathrm{mol}}}\right\rangle' \left\langle{+_{\mathrm{mol}}}\right|' + \hbar\omega_{\mathrm{e}} \left|{-_{\mathrm{mol}}}\right\rangle' \left\langle{-_{\mathrm{mol}}}\right|', \\
\hat{H}^{\mathrm{eff}}_{\mathrm{cav}}(\mathbf{k}) =& \left(E_0 + \frac{\hbar^2|\mathbf{k}|^2}{2m^*} + \zeta|\mathbf{k}|\cos\phi\right) \left|{+_{\mathrm{cav}}}\right\rangle' \left\langle{+_{\mathrm{cav}}}\right|' \\
&+ \left(E_0 + \frac{\hbar^2|\mathbf{k}|^2}{2m^*} - \zeta|\mathbf{k}|\cos\phi\right) \left|{-_{\mathrm{cav}}}\right\rangle' \left\langle{-_{\mathrm{cav}}}\right|' \\
&+ \left(-\beta_0 + \beta|\mathbf{k}|^2 e^{-i2\phi}\right) \left|{+_{\mathrm{cav}}}\right\rangle' \left\langle{-_{\mathrm{cav}}}\right|' \\
&+ \left(-\beta_0 + \beta|\mathbf{k}|^2 e^{i2\phi}\right) \left|{-_{\mathrm{cav}}}\right\rangle' \left\langle{+_{\mathrm{cav}}}\right|', \\
\hat{H}^{\mathrm{eff}}_{\mathrm{cav-mol}}(\mathbf{k}) =& \mathbf{J}_{\mathbf{k},+} \cdot \left(\sqrt{1 - f_- - 2f_+}\boldsymbol{\mu}_+ \left|{+_{\mathrm{mol}}}\right\rangle' \right. \\
&\left. + \sqrt{1 - f_+ - 2f_-}\boldsymbol{\mu}_- \left|{-_{\mathrm{mol}}}\right\rangle'\right) \left\langle{+_{\mathrm{cav}}}\right|' \\
&+ \mathbf{J}_{\mathbf{k},-} \cdot \left(\sqrt{1 - f_- - 2f_+}\boldsymbol{\mu}_+ \left|{+_{\mathrm{mol}}}\right\rangle' \right. \\
&\left. + \sqrt{1 - f_+ - 2f_-}\boldsymbol{\mu}_- \left|{-_{\mathrm{mol}}}\right\rangle'\right) \left\langle{-_{\mathrm{cav}}}\right|' + \mathrm{H.c.}
\end{aligned} \tag{3.7}$$

Here, the states $|\gamma\rangle'$ are different from states $|\gamma\rangle$ in eq. 3.5, where $\gamma = \pm_{\mathrm{mol}}, \pm_{\mathrm{cav}}$. As expected, the light-matter coupling terms are scaled by factors $\sqrt{1 - f_\mp - 2f_\pm}$ which is a consequence of the commutation relation in eq. 3.1 (see Section S3 in Supporting Information).

If the pump pulse is circularly polarized, $f_+ \neq f_-$, the Rabi contraction factor that multiplies the light-matter coupling differs for transitions to the $|{+_{\mathrm{mol}}}\rangle$ and $|{-_{\mathrm{mol}}}\rangle$ states; as a result, time-reversal symmetry is broken. Consequently, when $f_+ > f_-$, we find that bands 1 and

2 have non-zero Chern numbers +1 and -1 (Fig. 3.3f). Under the opposite condition, $f_+ < f_-$, the Chern numbers reverse sign as seen in Fig. 3.3g. When $f_+ = f_-$, TRS is preserved, and all bands have Chern number 0 as seen in Fig. 3.3e and 3.3h. In Fig. 3.3b-c, we plot the computed Berry curvature when $f_+ \neq f_-$ and due to broken TRS, we find $\Omega_l(\mathbf{k}) \neq -\Omega_l(-\mathbf{k})$. Non-zero values of Berry curvature are found at $k_x \sim \pm 8\mu\text{m}^{-1}$, $k_y \sim 0\mu\text{m}^{-1}$ when $f_+ = 0.3$, $f_- = 0$ or $f_+ = 0$, $f_- = 0.3$. To measure the Berry curvature of the bands at these values of $\mathbf{k}$, the linewidths of the cavity modes and the molecular transitions need to be less than 10meV as the energy splittings between the bands are $10 - 15$meV.

We also plot the Stokes parameter, $S_3(\mathbf{k})$, for bands 1 and 2, under pumping with circularly polarized light, in Fig. 3.4. The Stokes parameter, $S_3(\mathbf{k})$, provides information on the degree of circular polarization of the photonic component of an exciton-polariton band and is calculated as

$$S_3(\mathbf{k}) = \frac{|b_{+,\text{cav}}(\mathbf{k})|^2 - |b_{-,\text{cav}}(\mathbf{k})|^2}{|b_{+,\text{cav}}(\mathbf{k})|^2 + |b_{-,\text{cav}}(\mathbf{k})|^2} \tag{3.8}$$

where the eigenvectors of the band are $\left|u_{l,\mathbf{k}}\right\rangle = b_{+,\text{cav}}(\mathbf{k})\,|{+_{\text{cav}}}\rangle + b_{-,\text{cav}}(\mathbf{k})\,|{-_{\text{cav}}}\rangle + b_{+,\text{mol}}(\mathbf{k})\,|{+_{\text{mol}}}\rangle + b_{-,\text{mol}}(\mathbf{k})\,|{-_{\text{mol}}}\rangle$. In the absence of pumping, we find that within a band, one half of the modes are predominantly σ_+ polarized and the other half are σ_- polarized (Fig. 3.3e). Upon pumping with circularly polarized light, a large number of modes within each band gradually become of the same polarization as $|f_+ - f_-|$ is increased (Fig. 3.3f-g, Fig. 3.4 and Fig. S2).

In experiments, the Berry curvature of photon bands in a Fabry-Perot cavity can be extracted from the components of the Stokes vector [79, 80]. In the case of exciton-polariton bands, the Berry curvature can be measured experimentally using the Stokes vector when the bands of the system can be separated into pairs of bands that are effectively described by separate 2×2 Hamiltonians. At each $\mathbf{k}$, the Stokes vector can describe a state in a two-dimensional Hilbert space; however, the Stokes vector does not contain enough information to fully specify a state in a Hilbert space of dimensions larger than two. Therefore, in our four band model, the Berry curvature (Fig. 3.3a-d) can be experimentally measured by pump-probe spectroscopy

only when the splitting induced by the light-matter coupling is much larger than that induced by the coupling between cavity modes because then the four polariton bands can be separated into two pairs of bands that are effectively described by separate 2×2 Hamiltonians as in [103]. This measurement should be feasible as long as the time delay between the pump and probe pulses is shorter than the time the system takes to depolarize and reach a state with $f_+ = f_-$. The system's depolarization time depends only upon the bare molecular depolarization rate. As the depolarization timescale for porphyrins ranges from 210 fs to 1.6 ps, this measurement should be viable [104].

Population imbalances in the molecule or solid-state system can potentially be experimentally created in a variety of ways. One possibility is to directly excite higher energy material transitions with circularly polarized light that are within the transparency window of the cavity typically known as "non-resonant" pumping [26, 105]. If decay from those higher energy transitions into the relevant excited states happens before depolarization ensues, we will have obtained the desired population imbalances. Another possibility that bypasses the need of incoherent processes is a stimulated electronic Raman scattering with circularly polarized fields, although this scenario might require X-rays [106, 107]. Finally, the population imbalance may also be created by pumping resonantly with a circularly polarized laser at $|\mathbf{k}| = \sqrt{\beta_0/\beta}$, $\phi = 0$. At this angle, the coupling between the circularly polarized cavity modes is zero. Additionally, $|\mathbf{J}_{\mathbf{k},+} \cdot \boldsymbol{\mu}_-| \gg |\mathbf{J}_{\mathbf{k},+} \cdot \boldsymbol{\mu}_+|$ and $|\mathbf{J}_{\mathbf{k},-} \cdot \boldsymbol{\mu}_+| \gg |\mathbf{J}_{\mathbf{k},-} \cdot \boldsymbol{\mu}_-|$ for all $|\mathbf{k}| \ll n_z \pi / L_z$. Therefore, when the polariton mode at this $\mathbf{k}$ is pumped with circularly polarized light, the cavity mode of only the corresponding circular polarization is excited and population is transferred largely to only one of the circularly polarized molecular states. After dephasing into the molecular states (but not depolarization of the latter), the populations of the molecular states would be unequal $f_+ \neq f_-$.

As the Chern numbers of bands 1 and 2 are modified through pumping with circularly polarized light, if we perform a calculation where a region of the system is pumped with σ_+ polarized light ($f_+ \neq 0$ and $f_- = 0$) and an adjacent region is pumped with σ_- polarized light ($f_+ = 0$ and $f_- \neq 0$), we expect edge states at the boundary between these regions. However, as

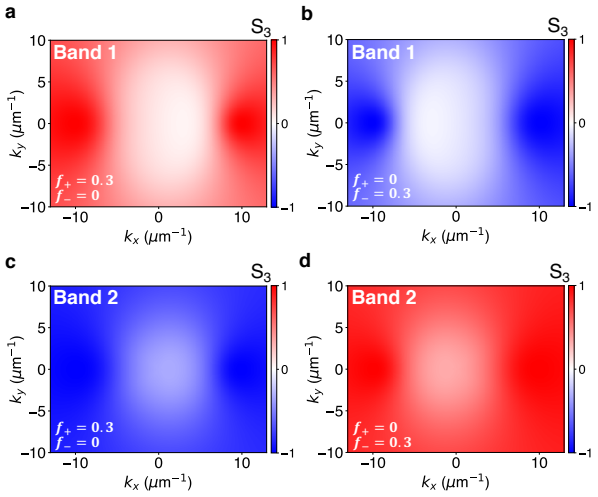

Figure 3.4. Stokes parameter. The Stokes parameter, $S_3(\mathbf{k})$, which is a measure of the degree of circular polarization of a mode (Eq. 3.8), under pumping with (a,c) σ_+ polarized light which creates populations $f_+ = 0.3$, $f_- = 0$ and (b,d) σ_- polarized light which creates populations $f_+ = 0$, $f_- = 0.3$ of the two lowest energy bands (Band 1 and 2 as indicated in the inset). We used parameters $\beta_0 = 0.1\text{eV}$, $\beta = 9 \times 10^{-4}\text{eV}\mu\text{m}^2$, $\zeta = 2.5 \times 10^{-3}\text{eV}\mu\text{m}$, $m^* = 125\hbar^2\text{eV}^{-1}\mu\text{m}^{-2}$, $E_0 = 3.80\text{eV}$ and $\hbar\omega_e = 3.81\text{eV}$ (see Section S4 in Supporting Information for details).

our Hamiltonian does not contain couplings between neighboring molecules, and the position of a molecule does not enter the Hamiltonian anywhere except through the phase of the light-matter coupling $e^{i\mathbf{k}\cdot\mathbf{r}_\mathbf{m}}$, the standard bulk-boundary correspondence is no longer applicable and we do not observe edge states. We do not include plots for these calculations in this work and leave it an open question whether there is an analogous statement for bulk-boundary correspondence in these types of systems. On the other hand, for exciton-polariton systems where nearest-neighbor couplings are present, edge states have been predicted and observed [73, 74].

3.2.3 Other systems

To emphasize that our scheme of saturating electronic transitions with circularly polarized light to modify topological properties is not limited to organic exciton-polariton systems, we compute the Berry curvature of two other polariton systems where porphyrin is replaced with (i) Ce:YAG and (ii) MoS_2 (Fig. 3.5a and 3.5d). Other materials can also be used in place of porphyrins, as long as they have transitions that can be selectively excited with circularly

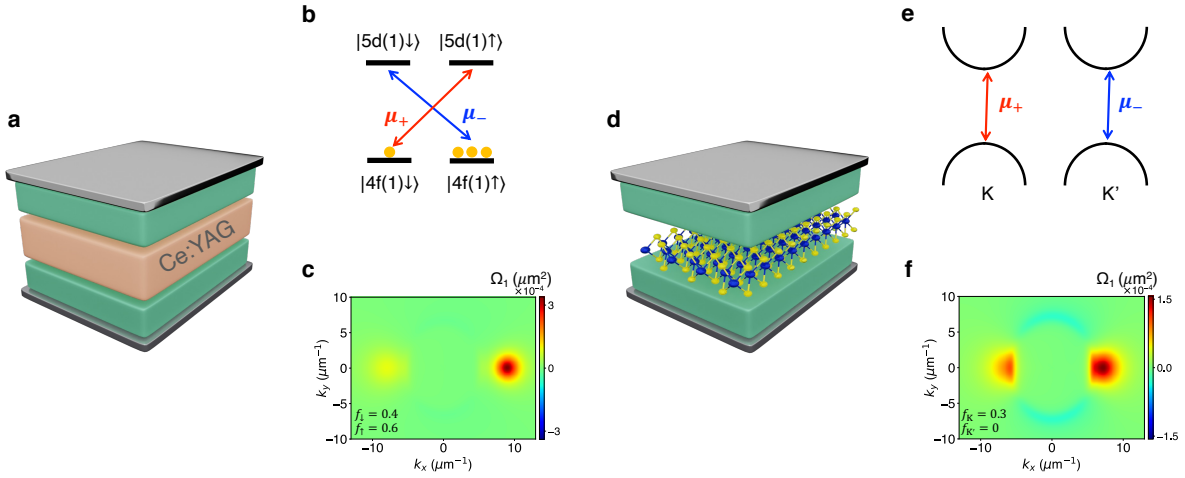

Figure 3.5. Solid-state polariton systems where population imbalance induces non-trivial topology. (a) Illustration of Ce:YAG (salmon block) and perylene (green blocks) within a Fabry-Perot cavity. (b) Atomic levels of Ce^{3+} ions embedded in Yttrium Aluminum garnet (YAG) where the yellow circles indicate the fraction $f_\downarrow$ of Ce^{3+} ions in the $|4f(1)\downarrow\rangle$ state and the fraction $f_\uparrow$ in the $|4f(1)\uparrow\rangle$ state after optical pumping. The transition dipoles $\boldsymbol{\mu}_\pm = \mu_0(\hat{\mathbf{x}} \pm i\hat{\mathbf{y}})/\sqrt{2}$ are also indicated. (c) Berry curvature of the lowest energy band, $\boldsymbol{\Omega}_1(\mathbf{k})$, under pumping with circularly polarized which creates populations $f_\downarrow = 0.4$ and $f_\uparrow = 0.6$. (d) Illustration of monolayer MoS_2 and perylene (green blocks) within a Fabry-Perot cavity. (e) Illustration of A-excitons in the K and K' valleys of monolayer MoS_2. (f) Berry curvature of the lowest energy band, $\boldsymbol{\Omega}_1(\mathbf{k})$, under pumping with circularly polarized which creates exciton populations $f_{\mathrm{K}} = 0.3$ and $f_{\mathrm{K}'} = 0$. We used parameters $\beta_0 = 0.1\mathrm{eV}$, $\beta = 9 \times 10^{-4}\mathrm{eV}\mu\mathrm{m}^2$, $\zeta = 2.5 \times 10^{-3}\mathrm{eV}\mu\mathrm{m}$, $m^* = 125\hbar^2\mathrm{eV}^{-1}\mu\mathrm{m}^{-2}$, (c) $E_0 = 2.50\mathrm{eV}$, $\hbar\omega_{\mathrm{e}} = 2.53\mathrm{eV}$ and (f) $E_0 = 1.80\mathrm{eV}$, $\hbar\omega_{\mathrm{e}} = 1.855\mathrm{eV}$ (see Section S4 in Supporting Information for details).

polarized light and these transitions have large enough transition dipole moments that they can couple strongly to the photon modes of a cavity.

In Yttrium Aluminum garnet (YAG) doped with Cerium, Ce^{3+} ions replace some Y^{3+} and Ce^{3+} has transitions that can be selectively excited with circularly polarized light. Here, each Ce^{3+} has two possible ground states, one with the electron in spin up $|4f(1)\uparrow\rangle$, and the other with it in spin down $|4f(1)\downarrow\rangle$. Similarly, it has a degenerate pair of excited spin states $|5d(1)\uparrow\rangle$ and $|5d(1)\downarrow\rangle$. The $|4f(1)\downarrow\rangle \leftrightarrow |5d(1)\uparrow\rangle$ transition has ~ 400 times larger oscillator strength for excitation with σ_+ polarized light than with σ_- polarized light, therefore, we take the transition dipole moment to be $\boldsymbol{\mu}_+$ (Fig. 3.5b) [108]. Similarly, we take the transition dipole to be $\boldsymbol{\mu}_-$ for the $|4f(1)\uparrow\rangle \leftrightarrow |5d(1)\downarrow\rangle$ transition (Fig. 3.5b). The transitions in Ce:YAG do couple to photon modes, however, to the best of our knowledge, strong coupling has not been reported in the literature [109, 110]. Nevertheless, strong light-matter coupling has been achieved with a similar system: Nd^{3+} doped YSO and YVO crystals [111, 112], and based on our calculations, with a 0.1μm thick sample of Ce:YAG at concentration 1% Ce^{3+} (relative to Y^{3+}), we should be able to attain strong coupling with photon modes in a Fabry-Perot cavity (see Section S4 in Supporting Information).

Under thermal equilibrium, the populations of the $|4f(1)\uparrow\rangle$ and $|4f(1)\downarrow\rangle$ states are equal. However, under pumping with pulses of σ_+ polarization, in the presence of a small magnetic field ~ 0.049T, the population of $|4f(1)\uparrow\rangle$ will exceed that of $|4f(1)\downarrow\rangle$ because population is selectively removed from $|4f(1)\downarrow\rangle$ and added to $|5d(1)\uparrow\rangle$ by the circularly polarized pulses, but decay from the excited $|5d(1)\uparrow\rangle$ state to the two ground states has equal probability [113]. In principle, a magnetic field is not required; however, as we do not know the spin relaxation time in the absence of the magnetic field, we report the magnetic field used in the experimental study [113]. Under optical pumping with circularly polarized light, the $5d$ states will have very small populations which we take to be zero, while the $|4f(1)\downarrow\rangle$ and $|4f(1)\uparrow\rangle$ states will have unequal populations $f_\downarrow$ and $f_\uparrow$, respectively; here, $f_\downarrow + f_\uparrow = 1$. Optically pumped Ce:YAG can then be modeled using the effective Hamiltonian in eq. B.15 and B.16, with $|\pm_{\text{mol}}\rangle' \rightarrow |5d(1)\uparrow/\downarrow\rangle$

and $\sqrt{1-f_{\mp}-2f_{\pm}} \rightarrow \sqrt{f_{\downarrow/\uparrow}}$. The large spin relaxation time of $\sim$ 4.5 ms makes this system particularly well-suited for our scheme because it maintains $f_{\downarrow} \neq f_{\uparrow}$, and hence non-zero Chern invariants, for an extended period of time [113]. In Fig. 3.5c we plot Berry curvature of the lowest band of a perylene filled cavity strongly coupled with Ce:YAG, where $f_{\downarrow} = 0.4$ and $f_{\uparrow} = 0.6$ (see Section S4 in Supporting Information for values of other parameters).

TMDs, such as single-layer MoS_2, display optically controllable valley polarization and could also be used in place of porphyrins [114–116]. Due to lack of inversion symmetry in these systems, the K and K' valleys are inequivalent; this results in optical selection rules that allow selective creation of excitons at K and K' valleys with σ_+ and σ_- polarized light, respectively [117, 118]. Additionally, strong light-matter coupling has been observed when monolayer MoS_2 is placed within a Fabry-Perot cavity [5,65]. This system has depolarization times of $\sim$ 200fs - 5ps making it possible to measure Berry curvature using pump-probe spectroscopy before depolarization occurs [119,120]. We model this exciton-polariton system (Fig. 3.5d) using eq. B.15 and eq. B.16 (we focus on the A-exciton, see Section S4 in Supporting Information for parameters) with $|+_{\mathrm{mol}}\rangle \rightarrow |\mathrm{K}\rangle$, $|-_{\mathrm{mol}}\rangle \rightarrow |\mathrm{K}'\rangle$ and $\sqrt{1-f_{\mp}-2f_{\pm}} \rightarrow \sqrt{1-2f_{\mathrm{K/K}'}}$. In Fig. 3.5f we plot the Berry curvature of the lowest band when $f_{\mathrm{K}} = 0.3$ and $f_{\mathrm{K}'} = 0$. Unfortunately, significant Rabi contraction upon optical pumping has not been experimentally observed in these systems which will make it challenging to observe Berry curvature as in Fig. 3.5f since our model relies on saturation effects. However, for exciton polaritons formed from monolayer TMDs, even if Rabi contraction through resonant optical pumping may not produce the intended effect, off-resonant optical pumping can break the degeneracy of excitons in the K and K' valleys through optical stark effect [121], and this may have interesting consequences for the Berry curvature. Additionally, if bilayer MoS_2 is used in place of monolayer MoS_2, effects on the Berry curvature described in our work may be more pronounced as bilayer MoS_2 hosts interlayer excitons which possess large optical nonlinearities; specifically, they display saturation and Rabi contraction under strong coupling [122, 123].

Finally, so far we have only considered replacing porphyrin with a different material,

such as MoS_2 or Ce:YAG. In addition to this, perylene can also be replaced with other suitable materials. In our work, we choose to use a cavity filled with perylene because we do not want degeneracy at any **k** within the photon bands. Other systems also satisfy this requirement and could be used instead. For instance, we could use an electrically tunable, highly anisotropic, liquid-crystal cavity with well separated H and V polarized photon modes [78, 124]. A perovskite cavity is another potential candidate due to its high anisotropy, and optical pumping may help lift the degeneracy of polariton modes in this system [103]. Additionally, other photonic structures can also be used instead of a cavity, as long as the photon bands are not degenerate at any **k** and have non-zero light-matter coupling at all **k**.

In our analysis, we have disregarded the explicit role of vibrational modes, which is a reasonable assumption for rigid molecular systems (such as porphyrins and phthalocyanines [125]) and solid-state systems as their electron-phonon (vibronic) couplings tend to be small.

3.3 Conclusion

In summary, we show that TRS can be broken in organic exciton-polariton systems through selectively saturating electronic transitions with a circularly polarized pump and that the resulting bands possess non-zero Chern invariants. In particular, we demonstrate this theoretically for a Fabry-Perot cavity filled with porphyrin and perylene. The Berry curvature of the more photonic parts of the bands of this system can be measured experimentally using pump-probe spectroscopy, as long as the time delay is shorter than the depolarization time for porphyrin (210fs-1.6ps) [104], and this will reveal non-zero Berry curvature and Chern number under circularly polarized pumping. Our scheme relies on Rabi contraction from saturation of optical transitions. It is important to note that edge states do not emerge in our system despite non-zero Chern invariants as our model does not contain sufficient positional information about the molecules or the unit cells. Bleu *et al*. [84] have previously proposed breaking TRS in inorganic exciton-polariton systems through pumping with circularly polarized light, however, their work relies on polariton

condensation and having patterned lattices. Finally, we demonstrate that saturating electronic transitions to modify topology is not limited to organic systems. To illustrate this, we calculate the Berry curvature and Chern numbers of exciton-polariton bands of two other systems under optical pumping: (a) Ce:YAG and (b) monolayer MoS_2, and find similar results as the organic exciton-polariton case. In view of recent developments on electrically tuning the Berry curvature of liquid-crystal and perovskite filled cavities [78, 80], our work provides an additional control knob to optically tune the Berry curvature of exciton-polariton systems using circularly polarized light. Additionally, ultrafast control of topological properties of systems with light may find use in nonreciprocal and nonlinear optoelectronic devices.

Chapter 3, in full, is adapted from the material as it appears in "Molecular and solid-state topological polaritons induced by population imbalance," S. Pannir-Sivajothi, N. P. Stern, J. Yuen-Zhou, *Nanophotonics* **12**, 3109–3119 (2023) [12]. The dissertation author was the primary investigator and author of this paper.

Chapter 4

Heat flow under vibrational strong coupling

4.1 Introduction

Several experiments have shown modification of chemical reactivity when molecules are placed within Fabry-Perot cavities and the vibrations of the molecules collectively strongly couple to the photon mode, even in the absence of optical pumping [14, 16, 126]. A few experiments have also reported no change in chemical reactivity under such conditions [18, 19, 127]. There is no clear consensus on the types of reactions that could be modified by collective vibrational strong coupling or on the mechanism underlying this modification.

Our experimental collaborators use an open cavity system and study the dehydration of $CuSO_4.5H_2O$ to $CuSO_4.3H_2O$ under collective vibrational strong coupling, where the OH stretch of the molecules couple strongly to the photon mode (see Fig. 4.1). In experiments with Fabry-Perot cavities, the concentrations of molecules are monitored through shifts in frequencies of higher-order cavity modes due to change in refractive index [126] or through changes in Rabi splitting [16]. The open cavity system used by our collaborators has the advantage that the concentration of reactants and products can be monitored directly through Raman microscopy.

In Fig. 4.1 we illustrate the experimental setup. This open cavity system contains copper sulfate pentahydrate deposited onto a nanocavity. The system is heated from below using a heating stage and our collaborators observed a reduction in stage temperature required for the

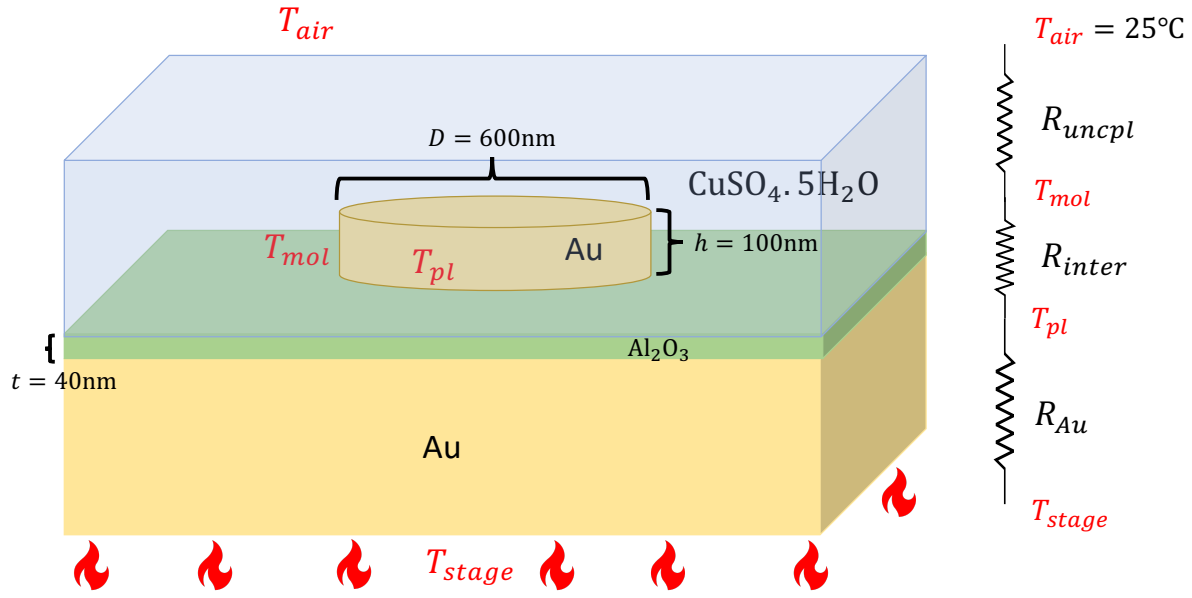

Figure 4.1. Illustration of the experimental open cavity setup with the heating stage in the bottom. A schematic of the one-dimensional heat flow model is depicted with the resistances on the right.

dehydration of copper sulfate pentahydrate to trihydrate under vibrational strong coupling at resonance. In Fig. 4.2 we reproduce their experimental results that show a reduction in the stage temperature required for dehydration under vibrational strong coupling (VSC).

Previous theoretical studies of phase transitions under collective strong coupling predict no significant change in transition temperatures due to VSC [128]. As the present work lies within the collective strong coupling regime, with $\sim 10^6$ coupled H_2O molecules, we similarly expect no significant change in the transition temperature for the $CuSO_4.5H_2O$ to $CuSO_4.3H_2O$ transformation. There is, however, no contradiction with the experimental results. Rather, we hypothesize that VSC resonantly enhances thermal energy transport into the molecular system, giving rise to the clear apparent decrease in the onset temperature for dehydration. Because of the open cavity architecture, where one end of the system is in contact with the heating stage and the other end in contact with room temperature air, there is a thermal gradient between the heated Au nanocavity substrate, the deposited molecular film, and the surrounding room

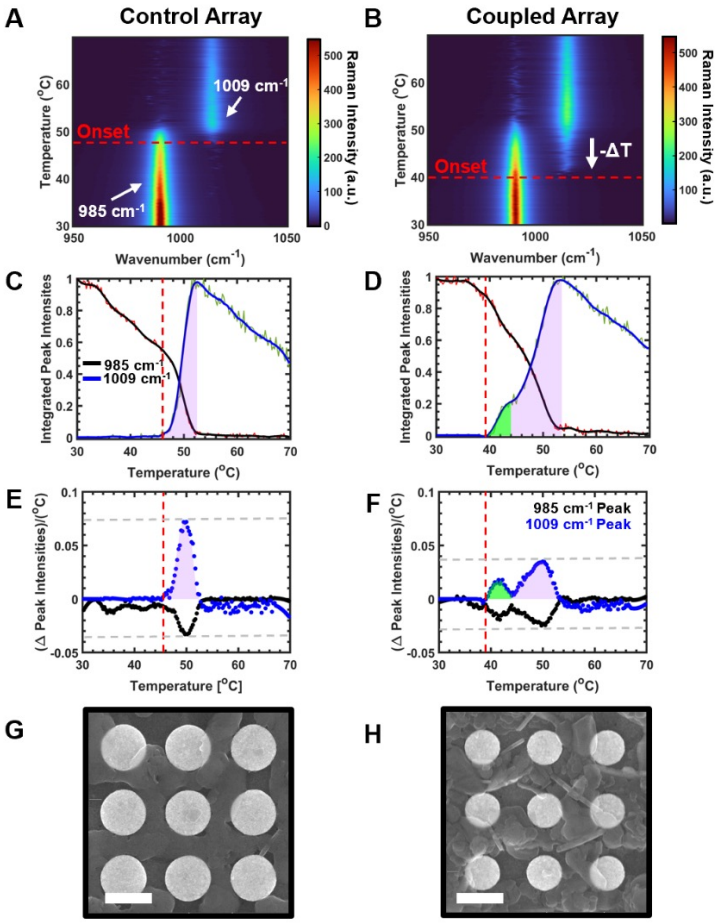

Figure 4.2. Molecular Raman spectra of $CuSO_4.5H_2O$. Molecular Raman spectra of $CuSO_4.5H_2O$ deposited on (**A**) spectrally detuned control and (**B**) resonant nanocavity arrays strongly coupled with the symmetric and asymmetric stretch of H_2O during stage heating ramps (0.5°C/min). The sulfate stretch of $CuSO_4.5H_2O$ (985 cm^{-1}) or $CuSO_4.3H_2O$ (1009 cm^{-1}) indicates the onset temperature for dehydration (red dashed) and the decrease in onset temperature ($-\Delta T$) on the resonant array. (**C**) – (**D**) Integrated counts (red = 985 cm^{-1}, green = 1009 cm^{-1}) and smoothed trend lines (black, blue), as well as the differential signal (**E**) – (**F**). Unperturbed chemical species (purple shading) and species with decreased onset temperature (green shading) are apparent on the resonant array. The grey dashed lines indicate the maximum change in peak intensities. SEM images highlight the differences in morphology of $CuSO_4.5H_2O$ deposited on control arrays (**G**) or resonant arrays (**H**) after multiple dehydration and rehydration cycles.

temperature air. VSC can reduce the thermal contact resistance between the nanocavity structure and the molecular film by providing an alternate path for direct energy transfer that resonantly outcompetes all other energy dissipation pathways. The result is a decrease in their temperature difference. We use a heat transfer model to support this interpretation. According to our model, energy transfer through polaritons is most efficient close to resonance, in agreement with the experimental results (see Fig. 4.5). However, we still expect qualitative behavior that is similar in the limit of weak light-matter coupling, as the role of the cavity is to enhance radiative heat transfer into the molecules [129]. The minimum light-matter coupling that would be sufficient to induce a stage temperature depression would in general depend on the specific thermal resistance characteristic of the interface.

4.2 Heat flow model

As the present work lies within this collective strong coupling regime with $N \sim 10^6$, we expect the transition temperature for the $CuSO_4.5H_2O$ to $CuSO_4.3H_2O$ transformation does not change under strong coupling. However, if there is a large contact resistance at the interface between the Al_2O_3 layer/Au disk and the pentahydrate crystal in the absence of strong light-matter coupling, VSC can reduce this contact resistance by providing an alternate path for energy transfer between them, reducing their temperature difference. We hypothesize that a lower heating stage temperature is observed for dehydration under VSC not due to a modification in the molecular transition temperature but because polariton modes provide an additional efficient channel for energy transport between the heating stage and the molecules which, in turn, decreases the temperature difference between them.

We use a one-dimensional heat transfer model (Fig. 4.3) to support our claim. Fourier's law of heat conduction relates the heat flux q''(in units of $Js^{-1}m^{-2}$) with a temperature gradient, $q'' = -\kappa\nabla T \approx \kappa(T_1 - T_2)/L$, where κ is the thermal conductivity, T_1 and T_2 are the temperature at different ends of the slab, and L is the thickness of the slab. The heat flowing through the slab

at steady state, q (in units of Js^{-1}), is then related to the temperature at the two ends of the slab T_1 and T_2 , $q = q''A = (T_1 - T_2)/R$, where $R = L/\kappa A$ is the thermal resistance of the slab. An analogy can be made with electrical circuits at steady state [130]; in fact, the last equation is analogous to current flow and Ohm's law, $I = (V_1 - V_2)/R_{electric}$, where $R_{electric}$ is the electric resistance, I is the current and $V_{1/2}$ are the voltages at the two ends of the resistor.

For every slab with constant thermal properties, we can associate a thermal resistance, $R = L/\kappa A$, where L is the thickness of the slab and A is the cross-sectional area across which heat flows. It is important to note that the analogy with electrical circuits holds only because there is no internal energy generation in our system.

In addition to the resistance across homogeneous slabs, we assume that there is a large thermal contact resistance, R_{inter}, at the interface between the Al_2O_3 layer and the molecules in the absence of strong light-matter coupling; therefore, there is a discontinuity in temperature across this interface. We consider two small regions on either side of the interface with uniform temperature: (i) the left side of the interface (brown region in Fig. 4.3A) which contains the Al_2O_3 layer at temperature T_{pl}, and (ii) the right side of the interface (dark blue region in Fig. 4.3A) that contains a small fraction of molecules near the interface at temperature T_{mol}. The heat flowing through this interface, q, is related to the temperature on either side of the interface, T_{pl} and T_{mol}, through $q = \left(T_{pl} - T_{mol}\right)/R_{inter}$.

There are three major regions in our system where there is a temperature drop: (i) the Au slab, which contains the Au mirror, with thermal resistance R_{Au} (yellow region in Fig. 4.3A), (ii) the molecular slab, which contains all the $CuSO_4.5H_2O$ molecules excluding those very close to the interface, with thermal resistance R_{uncpl} (light blue region in Fig. 4.3A), and (iii) the interface between the Al_2O_3 layer and the molecules with a thermal resistance R_{inter} (Fig. 4.3A).

In the absence of the Au disks and strong light-matter coupling, we apply energy conservation, $C\frac{dT}{dt} = q_{in} - q_{out}$, to the two small regions on either side of the interface (marked in brown and dark blue in Fig. 4.3A) [131]. Here, C is the heat capacity of the small region and

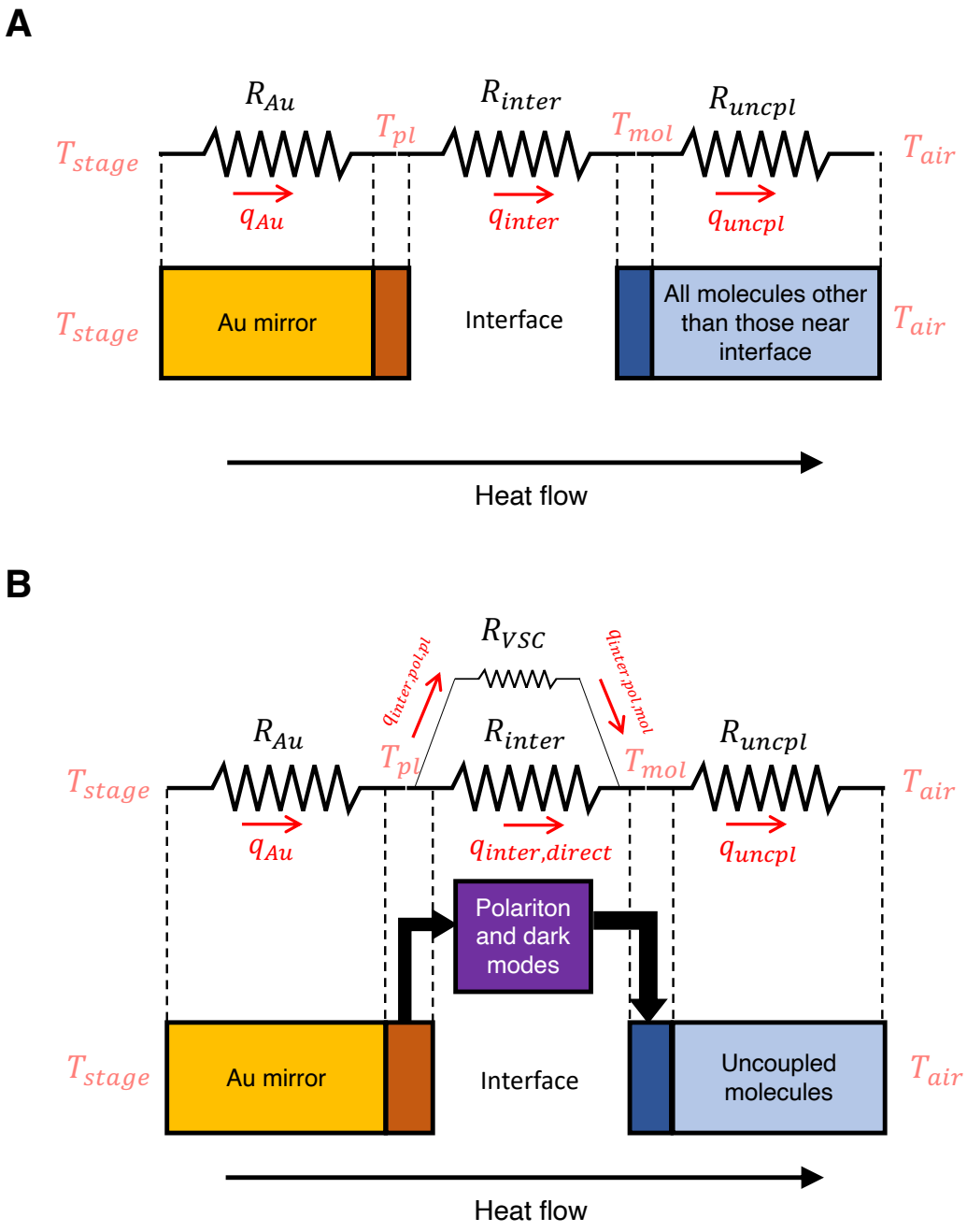

Figure 4.3. Schematic of the one-dimensional energy flow model used in our calculations for (A) the case without strong light-matter coupling and (B) the case with strong light matter coupling. In the case of a large contact resistance at the interface between the molecules and the Al2O3 layer/Au disk, R_{inter}, there is a large temperature difference between T_{pl} and T_{mol} in the uncoupled case. Strong coupling can provide an additional efficient channel for flow of energy through the interface if $R_{VSC} \ll R_{inter}$ and reduce the difference in temperature between T_{pl} and T_{mol}; this effectively leads to a lower heating stage temperature required for dehydration in the strongly coupled case compared to the uncoupled one.

q_{in} (q_{out}) is the heat flowing into (out of) it. This gives us the following two equations,

$$\begin{aligned} C_{pl}\frac{dT_{pl}}{dt} &= q_{Au} - q_{inter} \\ C_{mol}\frac{dT_{mol}}{dt} &= q_{inter} - q_{uncpl} \end{aligned} \tag{4.1}$$

where C_{pl} and C_{mol} are the heat capacities of the small regions on the left and right side of the interface, respectively. Here, q_{Au} is the heat flowing through the gold slab, q_{inter} is the heat flowing through the interface, and q_{uncpl} is the heat flowing through the molecules (see Fig. 4.3A). At steady state, $\frac{dT}{dt} = 0$, $q_{Au} = \frac{T_{stage}-T_{pl}}{R_{Au}}$, $q_{inter} = \frac{T_{pl}-T_{mol}}{R_{inter}}$, and $q_{uncpl} = \frac{T_{mol}-T_{air}}{R_{uncpl}}$, where T_{stage} is the temperature of the heating stage and T_{air} is the temperature of the air. This reduces the energy conservation equations to,

$$\begin{aligned} C_{pl}\frac{dT_{pl}}{dt} &= 0 = \frac{T_{stage} - T_{pl}}{R_{Au}} - \frac{T_{pl} - T_{mol}}{R_{inter}} \\ C_{mol}\frac{dT_{mol}}{dt} &= 0 = \frac{T_{pl} - T_{mol}}{R_{inter}} - \frac{T_{mol} - T_{air}}{R_{uncpl}} \end{aligned} \tag{4.2}$$

From these two equations, for known values of the resistances and T_{air}, we can extract the T_{stage} required such that the molecules reach their fixed transition temperature T_{trns} by setting $T_{mol} = T_{trns}$.

Similarly, for the strong coupling case, there are three major regions in our system where there is a temperature drop: (i) the Au slab, which contains the Au mirror, with thermal resistance R_{Au} (yellow region in Fig. 4.3B), (ii) the uncoupled molecular slab, which contains all the $CuSO_4.5H_2O$ molecules that are not strongly coupled to the plasmonic structure, with thermal resistance R_{uncpl} (light blue region in Fig. 4.3B), and (iii) the interface between the plasmonic structure and the molecules with a thermal resistance R'_{inter} which differs from R_{inter} due to strong coupling.

As our intention is to qualitatively understand experimental trends, for simplicity, we include a single vibrational mode per molecule which strongly couples to the plasmonic mode

in our model instead of two vibrational modes. We take the frequency of this mode to be $\omega_{vm} = 3242\text{cm}^{-1}$ and its collective coupling strength to the plasmon to be a function of the plasmon frequency $g_{vm}\left(\omega_{pl}\right) = g^0_{vm}\left(\omega_{pl}/\omega_{vm}\right)^{3/2}$ with $g^0_{vm} = 222\text{cm}^{-1}$.

The plasmonic and vibrational modes involved in strong coupling should be taken as part of the interface as they are involved in transferring energy between other uncoupled modes of the plasmonic structure and strongly coupled molecules. We consider two small regions on either side of the interface: (i) the left side of the interface (brown region in Fig. 4.3B) that contains the Al_2O_3 layer + Au disk (excluding the strongly coupled plasmon mode) at temperature T_{pl} which we call the plasmonic bath, and (ii) the right side of the interface (dark blue region in Fig. 4.3B) that contains the molecules strongly coupled to the plasmonic mode (excluding the molecular vibrations involved in strong coupling) at temperature T_{mol} which we refer to as the molecular bath. We expect that in addition to the regular contact resistance, R_{inter}, between the plasmonic and molecular baths, there is an additional parallel polariton channel for energy transport across the interface with resistance R_{VSC}. This can reduce the new total resistance across the interface $R'_{inter} = \frac{R_{inter}\,R_{VSC}}{R_{inter}+R_{VSC}} \approx R_{VSC}$ in the case when $R_{VSC} \ll R_{inter}$ (Fig. 4.3B).

The energy conservation equation applied to the two small regions on either side of the interface for the strong coupling case results in

$$\begin{aligned} C'_{pl}\frac{dT_{pl}}{dt} &= q_{Au} - q_{inter,direct} - q_{inter,pol,pl} \\ C'_{mol}\frac{dT_{mol}}{dt} &= q_{inter,direct} + q_{inter,pol,mol} - q_{uncpl}. \end{aligned} \tag{4.3}$$

Here, C'_{pl} and C'_{mol} are the heat capacities of the plasmonic and molecular baths, respectively, q_{Au} is the energy flowing through the gold slab, and q_{uncpl} is the heat flowing through the uncoupled molecules. Additionally, $q_{inter,pol,pl}$ is the energy flowing from the plasmonic bath into the polariton and dark modes, $q_{inter,pol,mol}$ is the energy flowing from the polariton and dark modes into the molecular bath, and $q_{inter,direct}$ is the energy flowing from the plasmonic bath into the molecular bath directly through all other modes of the system without involving

the strongly coupled modes. At steady state, $\frac{dT}{dt} = 0$, $q_{Au} = \frac{T_{stage}-T_{pl}}{R_{Au}}$, $q_{inter,direct} = \frac{T_{pl}-T_{mol}}{R_{inter}}$, and $q_{uncpl} = \frac{T_{mol}-T_{air}}{R_{uncpl}}$

$$\begin{aligned} 0 =& \frac{T_{stage} - T_{pl}}{R_{Au}} - \frac{T_{pl} - T_{mol}}{R_{inter}} - q_{inter,pol,pl} \\ 0 =& \frac{T_{pl} - T_{mol}}{R_{inter}} - \frac{T_{mol} - T_{air}}{R_{uncpl}} + q_{inter,pol,mol} \end{aligned} \tag{4.4}$$

To obtain $q_{inter,pol,pl}$ and $q_{inter,pol,mol}$, we write rate equations for the populations of the polariton and dark modes [43],

$$\begin{aligned} \frac{dn_{UP}}{dt} =& -\left|c_{pl}^{UP}\right|^2 \gamma'_{pl} \left[n_{UP} - \bar{n}_{BE}\left(\omega_{UP}, T_{pl}\right)\right] \\ & -\left|c_{vm}^{UP}\right|^2 \gamma'_{vm} \left[n_{UP} - \bar{n}_{BE}\left(\omega_{UP}, T_{mol}\right)\right] \\ & -\left|c_{vm}^{UP}\right|^2 \frac{(N-1)}{N} R_{UP\to D,avg} - \left|c_{vm}^{UP}\right|^2 \left|c_{vm}^{LP}\right|^2 \frac{1}{N} R_{UP\to LP} \\ \frac{dn_{LP}}{dt} =& -\left|c_{pl}^{LP}\right|^2 \gamma'_{pl} \left[n_{LP} - \bar{n}_{BE}\left(\omega_{LP}, T_{pl}\right)\right] - \left|c_{vm}^{LP}\right|^2 \gamma'_{vm} \left[n_{LP} - \bar{n}_{BE}\left(\omega_{LP}, T_{mol}\right)\right] \\ & -\left|c_{vm}^{LP}\right|^2 \frac{(N-1)}{N} R_{LP\to D,avg} + \left|c_{vm}^{UP}\right|^2 \left|c_{vm}^{LP}\right|^2 \frac{1}{N} R_{UP\to LP} \\ (N-1)\frac{dn_{D,avg}}{dt} =& -\gamma'_{vm}(N-1)\left[n_{D,avg} - \bar{n}_{BE}\left(\omega_{vm}, T_{mol}\right)\right] + \left|c_{vm}^{UP}\right|^2 \frac{(N-1)}{N} R_{UP\to D,avg} \\ & +\left|c_{vm}^{LP}\right|^2 \frac{(N-1)}{N} R_{LP\to D,avg} \end{aligned} \tag{4.5}$$

where

$$\begin{aligned} R_{UP\to D,avg} =& J\left(\omega_{UP} - \omega_{vm}\right)\Big\{n_{UP}\left(n_{D,avg}+1\right)\left[\bar{n}_{BE}\left(\omega_{UP}-\omega_{vm}, T_{mol}\right)+1\right] \\ & - n_{D,avg}\bar{n}_{BE}\left(\omega_{UP}-\omega_{vm}, T_{mol}\right)\left(n_{UP}+1\right)\Big\} \\ R_{LP\to D,avg} =& J\left(\omega_{vm} - \omega_{LP}\right)\Big\{n_{LP}\left(n_{D,avg}+1\right)\bar{n}_{BE}\left(\omega_{vm}-\omega_{LP}, T_{mol}\right) \\ & - n_{D,avg}\left[\bar{n}_{BE}\left(\omega_{vm}-\omega_{LP}, T_{mol}\right)+1\right]\left(n_{LP}+1\right)\Big\} \\ R_{UP\to LP} =& J\left(\omega_{UP} - \omega_{LP}\right)\Big\{n_{UP}(n_{LP}+1)[\bar{n}_{BE}(\omega_{UP}-\omega_{LP}, T_{mol})+1] \\ & - n_{LP}\bar{n}_{BE}(\omega_{UP}-\omega_{LP}, T_{mol})(n_{UP}+1)\Big\} \end{aligned} \tag{4.6}$$

Here, n_{UP} and n_{LP} are the populations of the upper and lower polariton modes, respectively, $n_{D,avg}$

is the average population of each dark mode, and $\left|c_i^k\right|^2$ is the molecular, $i = vm$, or plasmonic, $i = pl$, Hopfield coefficient of mode $k = UP, LP$. Additionally, $\bar{n}_{BE}(\omega, T) = \left(e^{\hbar\omega/k_B T} - 1\right)^{-1}$ is the Bose-Einstein occupation of a mode with frequency ω at temperature T, $J(\omega)$ is the spectral density, N is the number of molecules, ω_{UP} and ω_{LP} are the frequencies of the upper and lower polariton modes, respectively, γ'_{vm} and γ'_{pl} are the non-radiative decay rates of the vibrational and plasmonic modes, respectively.

The molecular and plasmonic non-radiative decay terms for the polaritons in Eq. 4.4 are of the form $\left|c_i^k\right|^2 \gamma'_i \left[n_k \left(\bar{n}_{BE}(\omega_k, T_i) + 1\right) - \bar{n}_{BE}(\omega_k, T_i)(n_k + 1)\right] \approx \left|c_i^k\right|^2 \gamma'_i \left[n_k - \bar{n}_{BE}(\omega_k, T_i)\right]$ where we can make this approximation because $\hbar\omega_k \gg k_B T_i$ and therefore $n_k, \bar{n}_{BE}(\omega_k, T_i) \ll 1$. Note that we do not make similar approximations in Eq. 4.5 as the frequencies of the phonon modes involved in these processes are comparable to $k_B T_{mol}$. The plasmonic and molecular non-radiative decay terms contribute to the energy exchange of polariton and dark modes with the plasmonic and molecular baths and will be included in $q_{inter,pol,pl}$ and $q_{inter,pol,mol}$. Additionally, the terms in Eq. 4.4 involving $R_{i\to j}$ correspond to the rates at which excitations go from mode i to j. During this process phonons are either absorbed from or emitted into the molecular bath and this contributes to $q_{inter,pol,mol}$.

$$
\begin{aligned}
q_{inter,pol,pl} =& -\hbar\omega_{UP}\left|c_{pl}^{UP}\right|^2 \gamma'_{pl}\ \left[n_{UP} - \bar{n}_{BE}\left(\omega_{UP}, T_{pl}\right)\right] \\
& -\hbar\omega_{LP}\left|c_{pl}^{LP}\right|^2 \gamma'_{pl}\ \left[n_{LP} - \bar{n}_{BE}\left(\omega_{LP}, T_{pl}\right)\right] \\
q_{inter,pol,mol} =& \hbar\omega_{UP}\left|c_{vm}^{UP}\right|^2 \gamma'_{vm}\left[n_{UP} - \bar{n}_{BE}(\omega_{UP}, T_{mol})\right] \\
& + \hbar\omega_{LP}\left|c_{vm}^{LP}\right|^2 \gamma'_{vm}\left[n_{LP} - \bar{n}_{BE}(\omega_{LP}, T_{mol})\right] \\
& + \hbar\omega_{vm}(N-1)\gamma'_{vm}\left[n_{D,avg} - \bar{n}_{BE}(\omega_{vm}, T_{mol})\right] \\
& + \hbar\left(\omega_{UP} - \omega_{vm}\right)\left|c_{vm}^{UP}\right|^2 \frac{(N-1)}{N} R_{UP\to D,avg} \\
& + \hbar\left(\omega_{UP} - \omega_{LP}\right)\left|c_{vm}^{UP}\right|^2 \left|c_{vm}^{LP}\right|^2 \frac{1}{N} R_{UP\to LP} \\
& - \hbar\left(\omega_{vm} - \omega_{LP}\right)\left|c_{vm}^{LP}\right|^2 \frac{(N-1)}{N} R_{LP\to D,avg}
\end{aligned}
\tag{4.7}
$$

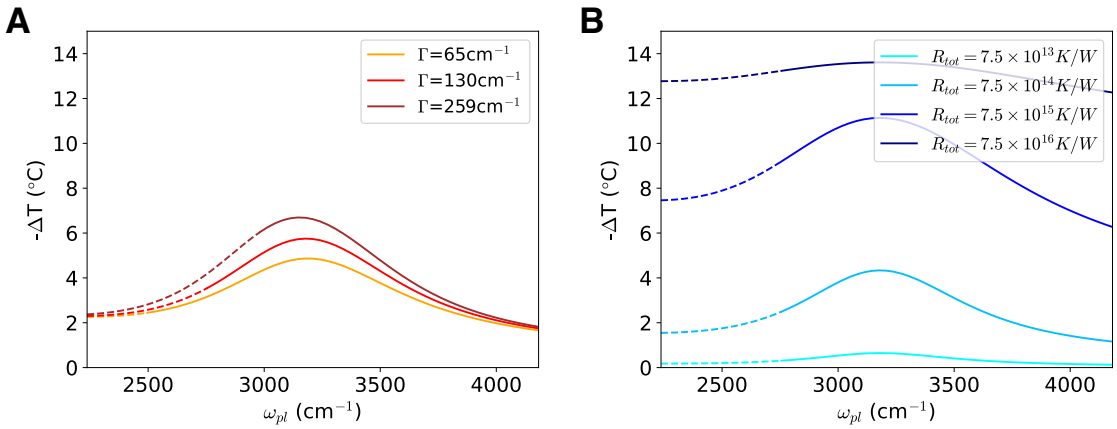

Figure 4.4. The temperature of the heating stage required for dehydration under strong coupling relative to the uncoupled case for different thermal contact resistance values. The temperature of the heating stage required for dehydration under strong coupling relative to the uncoupled case $-\Delta T = 50°C - T_{stage}$ is plotted as a function of the frequency of the plasmon mode ω_{pl} for (A) different values of the coefficient multiplying the spectral density Γ with $R_{tot} = 1.2 \times 10^{15}$K/W and (B) different values of the total thermal resistance in the absence of strong coupling R_{tot} with $\Gamma = 130\text{cm}^{-1}$. The dashed lines indicate parameters where our equations may not give physically relevant results as the rate of transfer of excitations from the upper polariton to all dark modes exceeds the frequency difference between them and Eq. 4.5 are not valid.

To obtain the steady-state heating stage temperature T_{stage}, we set Eq. 4.5 to zero and solve them along with Eq. 4.4 when the molecular temperature equals the fixed transition temperature $T_{mol} = T_{trns} = 36°\text{C}$. As we have five equations and five unknowns: T_{stage}, T_{pl}, n_{UP}, n_{LP}, and $n_{D,avg}$, we can solve this system of nonlinear equations numerically. Additionally, we expect $q_{inter,pol,pl} = q_{inter,pol,mol}$ which we verify numerically. From here on, we use $q_{inter,pol}$ in place of $q_{inter,pol,pl}$ and $q_{inter,pol,mol}$. We define the resistance $R_{VSC} = \left(T_{pl} - T_{mol}\right)/q_{inter,pol}$. The resistance R_{VSC} depends on the coupling strength g_{vm} and the detuning $\Delta = \omega_{vm} - \omega_{pl}$.

For our calculations, we need to choose values for the nonradiative population decay parameters, γ'_{pl} and γ'_{vm}. For bulk water, the vibrational relaxation time of the OH stretching mode is $\sim 260\text{fs}$ (129cm^{-1}) [132, 133]; however, the same stretching mode takes much longer to vibrationally relax $\sim 2 - 8\text{ps}$ ($4 - 16\text{cm}^{-1}$) in a crystalline hydrate [134–137]. Hence, we choose a molecular decay rate $\gamma'_{vm} = 10\text{cm}^{-1}$ which lies within this range $4 - 16\text{cm}^{-1}$. In addition, we choose $\gamma'_{pl} = 50\text{cm}^{-1}$ for the plasmonic nonradiative decay rate.

In the case without strong coupling, the total resistance of the system is $R_{tot} = R_{Au} + R_{inter} + R_{uncpl}$ (Fig. 4.3). The absolute values of these resistances are not known from the experiment; however, their ratios can be estimated from experimental parameters. The total resistance, R_{tot}, can be varied to fit experimental results. We take the molecular transition temperature to be $T_{trns} = 36°\text{C}$, which is the lowest stage temperature recorded for the onset of the phase transition (which occurs under VSC), and thus, according to our model, the actual transition temperature when heat conduction between the stage and the molecules is optimized. The air temperature is taken to be equal room temperature $T_{air} = 25°\text{C}$. From the experiment, we know that the chemical transformation occurs when $T_{stage} = T_{stage,out} = 50°C$ in the absence of the Au disks. The relationship between the resistances can be obtained by recognizing that the heat flows q_i are equal between the stage and the molecules, and the molecules and the air, $(T_{trns} - T_{air}) / R_{uncpl} = \left(T_{stage,out} - T_{trns}\right) / (R_{Au} + R_{inter})$ and we have $R_{inter} = \alpha R_{uncpl} - R_{Au}$ where $\alpha = \frac{T_{stage,out} - T_{trns}}{T_{trns} - T_{air}} = 1.27$. We take the thermal resistance of the gold mirror to be much smaller than that of other parts of the system $R_{Au} = 10^{-3} R_{tot}$. Therefore, we use $R_{Au} = 10^{-3} R_{tot}$, $R_{uncpl} = R_{tot}/(1 + \alpha)$ and $R_{inter} = \left(\frac{\alpha}{1+\alpha} - 10^{-3}\right) R_{tot}$ for all our calculations with $\alpha = 1.27$. We plot the computed decrease in the heating stage temperature for dehydration $-\Delta T = 50°C - T_{stage}$ under strong coupling for different values R_{tot} in Fig. 4.4B. We see that the effect of strong coupling increases as we increase R_{tot} because R_{inter} will increase and most of the heat will flow through R_{VSC} as it will be smaller than R_{inter}. On the other hand, when R_{tot} is small, and hence R_{inter} is small, most of the heat will flow through the direct channel, R_{inter}, instead of through the polariton and dark modes, R_{VSC}.

We use a Debye spectral density $J(\omega) = \frac{\Gamma \omega_c \omega}{\omega_c^2 + \omega^2}$ in our calculations with $\omega_c = 500\text{cm}^{-1}$ [138]. Along with R_{tot}, we vary the coefficient Γ to fit experimental results. We plot the change in heating stage temperature required for the dehydration for different values of Γ in Fig. 4.4A. We observe that for larger values of Γ a lower heating stage temperature is required to achieve dehydration; this effect is particularly large at resonance $\omega_{pl} = \omega_{vm}$. The factor Γ is proportional to the rate of energy flow between the polariton and dark modes and the larger it is, the more

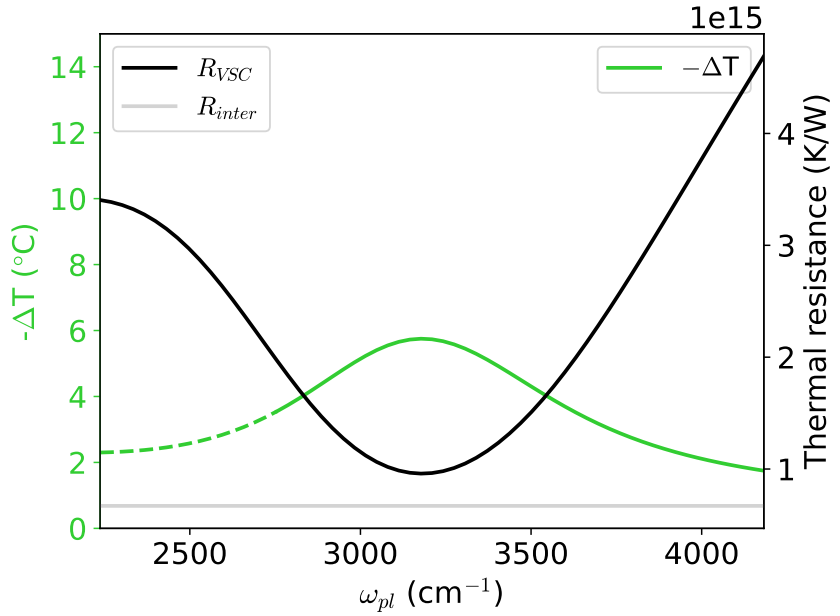

Figure 4.5. The temperature of the heating stage required for dehydration under strong coupling relative to the uncoupled case. The temperature of the heating stage required for dehydration under strong coupling relative to the uncoupled case $-\Delta T = 50°C - T_{stage}$ is plotted in green as a function of the frequency of the plasmon mode, ω_{pl}. In black, we plot the thermal contact resistance due to the polariton channel, R_{VSC}, and in grey, we plot the thermal contact resistance for transport of energy through all other modes of the system, R_{inter}. The dashed lines indicate parameters where our equations may not give physically relevant results as the rate of transfer of excitations from the upper polariton to all dark modes exceeds the frequency difference between them and Eq. 4.5 are not valid.

efficient the polariton and dark modes become at transferring energy between the plasmonic and molecular baths. Importantly, Eq. 4.5 are valid only when the rate of transfer of excitations between the different modes is smaller than the frequency difference between the modes. The dashed lines in Fig. 4.4 and Fig. 4.5 indicate parameters where this condition is not satisfied; specifically, the rate of transfer of excitations from the upper polariton to all the dark modes exceeds their frequency difference $\omega_{UP} - \omega_{vm}$.

Finally, in Fig. 4.5, we plot the lowering of the heating stage temperature required for dehydration with parameters $R_{tot} = 1.2 \times 10^{15}$K/W, $\Gamma = 130\text{cm}^{-1}$, $N = 10^6$, $\gamma'_{vm} = 10\text{cm}^{-1}$, $\gamma'_{pl} = 50\text{cm}^{-1}$, $\omega_c = 500\text{cm}^{-1}$, $\alpha = 1.27$, $R_{Au} = 10^{-3} R_{tot}$, $T_{trns} = 36°C$, and $T_{air} = 25°C$. We clearly observe that the effect is largest on resonance $\omega_{pl} \approx \omega_{vm}$. We also plot R_{VSC} in this figure

and it is consistent with our expectations that it will be smallest at resonance.

The present model has been developed assuming VSC. However, we still expect qualitative behavior that is similar in the limit of weak light-matter coupling, as the role of the cavity is to enhance radiative heat transfer into the molecules. The code is available at https://github.com/SindhanaPS/Thermal_Resistance_Model.

Chapter 4, in part, has been submitted for publication as it appears in "Sub-wavelength chemical imaging of a modified reaction due to vibrational strong coupling," Z. Brawley, J. E. Yim*, S. Pannir-Sivajothi*, Y. R. Poh, J. Yuen-Zhou, and M. Sheldon, ChemRxiv preprint (2023) [20]. The dissertation author led the theoretical section of this paper (* indicates equal contribution).

Chapter 5

Franck-Condon spectroscopy as quantum metrology

5.1 Introduction

The displaced harmonic oscillator is one of the simplest models that produces vibronic progressions in electronic absorption spectrum [139]. This model contains a pair of electronic states – the ground, $|G\rangle$, and the excited, $|E\rangle$, – and one vibrational degree of freedom modeled as a harmonic oscillator with creation operator $\hat{a}^\dagger$. The equilibrium position of the harmonic oscillator determines the bond length of the molecule in a given electronic state. The Hamiltonian for this model is

$$\begin{aligned}\hat{H}_0 = |E\rangle\langle E| \left[\hbar\Omega + \hbar\omega_{\mathrm{v}}(\hat{a}^\dagger - \sqrt{S})(\hat{a} - \sqrt{S}) + \frac{\hbar\omega_{\mathrm{v}}}{2}\right] \\ + |G\rangle\langle G| \hbar\omega_{\mathrm{v}}\left(\hat{a}^\dagger\hat{a} + \frac{1}{2}\right)\end{aligned} \tag{5.1}$$

where Ω is the frequency of the bare electronic transition, ω_{v} is the frequency of the vibrational mode, and S is the Huang-Rhys factor that quantifies the coupling between the electronic and vibrational degrees of freedom. Additionally, the Huang-Rhys factor is also related to the change in bond length between the two electronic states, Δd, through $\hbar\omega_{\mathrm{v}}S = \frac{1}{2}m\omega_{\mathrm{v}}^2(\Delta d)^2$.

The absorption cross section, $A(\omega)$, of this model can be obtained by adding a perturbative light-matter coupling term $\hat{V}(t) = -\varepsilon(t)(\mu_{GE}|G\rangle\langle E| + \mu_{EG}|E\rangle\langle G|)$ to the bare Hamiltonian

$\hat{H}_0$ and applying first-order time-dependent perturbation theory. Here, $\varepsilon(t) = \varepsilon_0 \sin \omega t$ is the electric field of the monochromatic electromagnetic wave with frequency ω used to probe the system, and μ_{GE} is the transition dipole moment of the molecule. The absorption cross section $A(\omega) = (\frac{4\pi^2|\mu_{EG}|^2\Omega}{\epsilon_0 \hbar c})C(\omega)$ where

$$C(\omega) = \left(\frac{\omega}{\Omega}\right) \sum_{f=-\nu}^{\infty} |\, \langle \nu | \nu + f \rangle' \,|^2 \delta(\omega - \Omega - f\omega_{\mathrm{v}}) \tag{5.2}$$

is the scaled absorption cross section, $|\nu\rangle$ is the initial vibrational state of the system and is an eigenstate of the harmonic oscillator associated with annihilation operator $\hat{a}$, and $|\nu + f\rangle'$ are eigenstates of the displaced harmonic oscillator associated with annihilation operator $\hat{a} - \sqrt{S}$. From the absorption cross section, the Franck-Condon factor $|\, \langle \nu | n \rangle' \,|^2$ can be extracted; here, ν and n are non-negative integers. The Franck-Condon factors also form a probability distribution

$$P_\nu(n; S) = |\, \langle \nu | n \rangle' \,|^2, \tag{5.3}$$

and it is useful to think about them this way.

Usually, in absorption spectra, the initial state is taken to be the ground vibrational state $|0\rangle$ because $k_B T \ll \hbar\omega_{\mathrm{v}}$ for these high-frequency vibrational modes at room temperature and the thermal occupation of higher vibrational states is negligible. As a result, the Franck-Condon factors starting from $|0\rangle$,

$$|\, \langle 0 | n \rangle' \,|^2 = e^{-S} \frac{S^n}{n!}, \tag{5.4}$$

are textbook material. Franck-Condon factors have been studied in detail in the literature with results ranging from analytical expressions [140, 141] to efficient algorithms that compute multidimensional Franck-Condon overlaps in polyatomic molecules [142]. However, taking the initial state to be a high Fock state $|\nu\rangle$ with $\nu > 0$ leads to interesting results that have, surprisingly, not been explored so far. The deceptively simple displaced harmonic oscillator model offers potential schemes for quantum metrology.

5.2 Results

5.2.1 Small S: quantum metrology

Normally, the Huang-Rhys factor can be obtained from the heights of the vibronic peaks in the experimentally measured spectrum. This is done by extracting the Franck-Condon overlap squared $P_0(n;S) = e^{-S}\frac{S^n}{n!}$ and because it is a Poisson distribution, S can be extracted from either the mean $\bar{n}_0 = \sum_n nP_0(n;S) = S$ or the variance $\sigma_0^2 = \sum_n (n-\bar{n}_0)^2 P_0(n;S) = S$ [143–147].

When $S \ll 1$, that is, the change in bond length between electronic states, Δd, is much smaller than the width, $\sqrt{\frac{\hbar}{m\omega_v}}$, of the ground vibrational wavefunction $\psi_0(x) = \langle x|0\rangle$ in position-space, the overlap $|\langle 0|0\rangle'|^2 \approx 1$ and hence the heights of the vibrational sidebands are negligible (see Fig. 5.1(b)). Therefore, the absorption spectrum for $S \ll 1$ will look very similar to the $S = 0$ case and it will be difficult to precisely determine the value of S from the spectrum. The natural length-scale $\sqrt{\frac{\hbar}{m\omega_v}}$ of the ground vibrational wavefunction limits the resolution of distance measurements.

In our work, we consider scenarios where the system can be prepared in a higher vibrational Fock state $|\nu\rangle$ initially instead of the ground state $|0\rangle$. Therefore, to understand the potential enhancements in distance resolution that can be obtained from this, we define a new length-scale l_ν associated with the vibrational Fock state $|\nu\rangle$ which is like an 'average' wavelength of the wavefunction $\psi_\nu(x) = \langle x|\nu\rangle$. Here, $|x\rangle$ is an eigenstate of the position operator $\hat{x} = \frac{1}{2}\sqrt{\frac{2\hbar}{m\omega_v}}(\hat{a}^\dagger + \hat{a})$ and

$$\frac{l_\nu}{2} = \frac{2X_{\nu,\max}}{\nu+1}, \tag{5.5}$$

where $X_{\nu,\max}$ is the classical turning point of a particle in a harmonic potential with total energy $E_\nu = \hbar\omega_v(\nu + 1/2)$ and satisfies $\frac{1}{2}m\omega_v^2 X_{\nu,\max}^2 = E_\nu$ (see Fig. 5.2(a)). We have used the fact that $\psi_\nu(x)$ has ν nodes. For $\nu \gg 1$, the length-scale becomes

$$l_\nu \approx 4\sqrt{\frac{2\hbar}{m\omega_v}}\sqrt{\frac{1}{\nu}}. \tag{5.6}$$

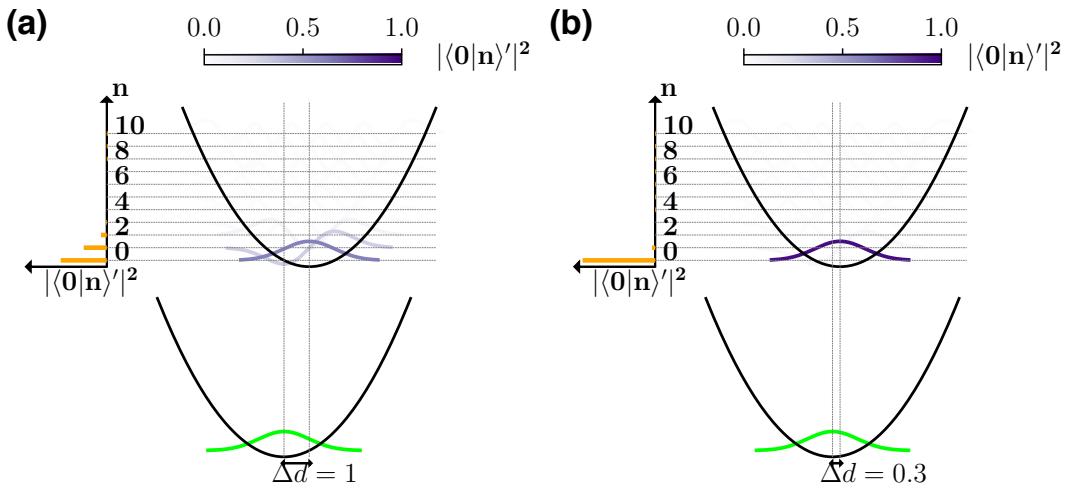

Figure 5.1. Preparing the system in the ground vibraional state initially. The two parabolas are the ground and excited potential energy surfaces. The system is initially in the vibrational ground state $|0\rangle$ (green curve) and we plot the Franck-Condon factors $|\langle 0|n\rangle'|^2$ in orange; here, $|n\rangle'$ are the eigenstates of a harmonic oscillator displaced by Δd from the ground state oscillator. When the displacement $\Delta d \sim \sqrt{\frac{\hbar}{m\omega_v}}$ as in **(a)**, we see significant overlap for $n = 0$ and $n = 1$, whereas, when $\Delta d \ll \sqrt{\frac{\hbar}{m\omega_v}}$ as in **(b)** the overlap is negligible for $n \neq 0$. It would be difficult to precisely estimate the value of the Huang-Rhys factor S from **(b)** as the Franck-Condon factors look very similar to those for $S = 0$.

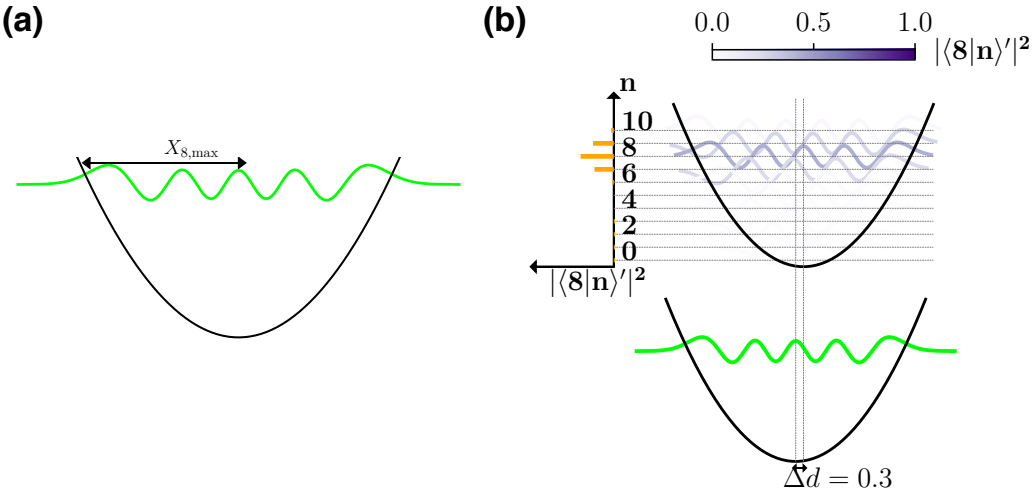

Figure 5.2. Preparing the system in a Fock state $|8\rangle$ initially and the length scale associated l_8. **(a)** The position-space wavefunction $\psi_8(x)$ of Fock state $|8\rangle$ (green) and the classical turning point $X_{8,\mathrm{max}}$ that satisfies $\frac{1}{2}m\omega_{\mathrm{v}}^2 X_{\nu,\mathrm{max}}^2 = \hbar\omega_{\mathrm{v}}(8+1/2)$. From this, the length scale l_ν associated with Fock state $|\nu\rangle$ can be computed, $l_\nu \approx 4\sqrt{\frac{2\hbar}{m\omega_{\mathrm{v}}}}\sqrt{\frac{1}{\nu}}$. **(b)** The Franck-Condon factors $|\langle 8|n\rangle'|^2$ show that even if $\Delta d \ll \sqrt{\frac{\hbar}{m\omega_{\mathrm{v}}}}$ as long as $\Delta d \sim l_8$, the overlap squared $|\langle 8|n\rangle'|^2$ is significant even for $n \neq 8$.

Consequently, preparing the system in a Fock state with large ν may improve distance resolution as l_ν becomes smaller with increasing ν; the ratio $\Delta d/l_\nu$ will play an important role here.

Similar to how the mean and variance of $P_0(n;S)$ are S, the mean and variance of $P_\nu(n;S)$ turn out to be linear functions of S. The mean $\bar{n}_\nu = S + \nu$ and the variance

$$\sigma_\nu^2 = S(2\nu+1) \tag{5.7}$$

(see Supplementary). The value of S can be inferred from the variance or the mean of the probability distribution. However, the advantage in measurement resolution with an initial state with $\nu > 0$ is only present when the variance is used to infer S as the variance scales linearly in ν. If the mean is used, there is no advantage; in fact, it is disadvantageous to use a Fock state with $\nu > 0$ (see Supplementary Fig.).

Let us consider a situation where the precision of the measured absorption cross section

is limited. We obtain the the estimated value of the Huang-Rhys factor $S_{\text{est}} = \sigma^2_{\nu,\text{est}}/(2\nu+1)$ from the variance $\sigma^2_{\nu,\text{est}}$ of the probability distribution $P_{\nu,\text{est}}(n)$ extracted from this measured cross section. If the measured absorption spectrum were known to infinite precision, then $P_{\nu,\text{est}}(n) = P_\nu(n;S)$ and we can exactly determine the Huang-Rhys factor $S_{\text{est}} = S$ starting from any initial state $|\nu\rangle$. However, if the precision of the spectroscopic device is limited due to noise, for instance, if the heights of the stick spectrum $C(\omega)$ are known with confidence only upto the first few decimal places, then S_{est} may not equal S and the closeness of the estimated Huang-Rhys factor to the true one will depend on the initial state $|\nu\rangle$. In Fig. 5.3, we plot S_{est} when $C(\omega)$ is only known upto the first decimal place for initial states $|0\rangle$ (black) and $|10\rangle$ (orange). We round off the true $C(\omega)$ obtained from S to the first decimal place and use its variance to obtain S_{est}.

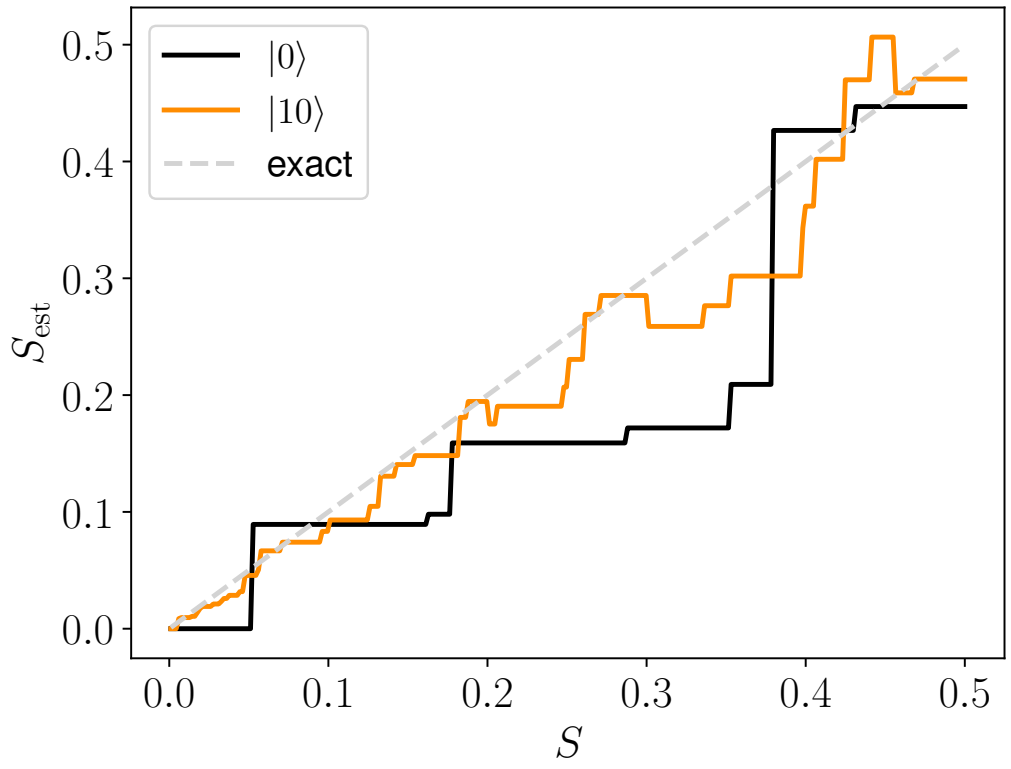

Figure 5.3. The estimated Huang-Rhys factor for a precision-limited absroption cross section measurement. The estimated Huang-Rhys factor S_{est} for different initial vibrational states $|0\rangle$ (black) and $|10\rangle$ (orange). The grey dashed line indicates $S_{est} = S$. Here, S_{est} is obtained from the variance of the distribution $P_{\nu,\text{est}}(n)$ which is extracted from a precision-limited absorption cross section (limited to the first decimal place).

Note how the initial state $|0\rangle$, gives us $S_{\text{est}} = 0$ when $S < 0.05$. This happens because the height of the first vibrational sideband in $C(\omega)$ rounds off to 0.0 when it is smaller than 0.05 and this give us an estimate $S_{est} = 0$. Also notice the step structure of S_{est} for both initial states and how the size of the steps are smaller for $|10\rangle$.

Chapter 5, in full, is currently being prepared for submission for publication of the material. "Franck-Condon spectroscopy as quantum metrology," S. Pannir-Sivajothi, J. Yuen-Zhou. The dissertation author was the primary investigator and author of this material.

Chapter 6

Conclusions

This dissertation uses simple models to identify avenues where strong light-matter coupling could have a large effect on a material property or process. Here, we studied the effect of polariton condensation on chemical reactions under VSC, generation of topological properties in polariton systems through saturating electronic transitions with circularly polarized light, and modification of heat flow under vibrational strong coupling. Additionally, we also considered how small values of the Huang-Rhys factor can be extracted from the electronic absorption spectrum if the system is initially prepared in a higher vibrational Fock state.

First, we looked at the effect of vibrational polariton condensation on an electron transfer process. As polaritons are delocalized over a large ensemble $N \sim 10^{10}$ of molecules and intramolecular electron transfer is a local molecular process, their effect on the process was small and was scaled by factors of $1/N$. We found that under Bose-Einstein condensation of polaritons, the effect of polaritons is enhanced by a factor of N_{ex}, where N_{ex} is the macroscopic population of the polariton modes under condensation. We observed modifications in both the rate and yield of the reaction under polariton condensation.

Second, we investigated the role of selective saturation of electronic transitions using circularly polarized light in modifying the topological properties of a polariton system. Using mean field theory, we derived an effective Hamiltonian for the optically pumped system and found that the light-matter couplings are scaled by factors of $\sqrt{1-2f}$ where f is the excited state

population. This allowed for breaking of time-reversal symmetry in the system through different excited state populations $f_+ \neq f_-$ and modification of the Berry curvature of polariton bands.

Third, we developed a heat transfer model using kinetic rate equations to explain the experimentally observed reduction in required stage temperature for a dehydration reaction under resonance condition with vibrational strong coupling. As this was an open cavity system placed on a heating stage and in contact with room temperature air, we hypothesized that there must be a temperature gradient across the sample and a large temperature drop across the interface between the molecules and the plasmonic structure. Using kinetic rate equations we modeled this system and identified an alternate channel for radiative heat transport across this interface through polaritons.

Apart from systems under strong light-matter coupling, we also studied how changing the initial vibrational state of a molecule has an effect on it electronic absorption spectrum which could be used to measure small values of coupling between electronic and vibrational degrees of freedom. Starting from a higher vibrational Fock state allows us to measure small displacements of the vibrational coordinate between electronic states as it has a smaller length scale associated with it compared to the ground vibrational state.

Finally, many theoretical studies show that the effect of polaritons on chemical reactions are expected to be small. In this dissertation, we demonstrated that strong light-matter coupling could be beneficial for processes other than chemical reactions, such as enhanced radiative heat transport across barriers with large thermal contact resistances, or modification of topological properties by changing the light-matter coupling strength through optical pumping. Furthermore, we show that the small polaritonic effects on chemical reactivity under collective strong coupling can also be enhanced through polariton condensation.

Appendix A

Supplementary Information: Driving chemical reactions with polariton condensates

A.1 Supplementary Note 1

We use a generalization of the dark state basis introduced in [49, 55] to reduce the number of vibrational modes involved in the reaction. The bosonic operator for $\mathrm{D}_{\mathrm{R},c}$, the dark mode highly localized in the c^{th} molecule when it is in electronic state $|R\rangle$ with total number of reactants N_{R} and products N_{P} is

$$\begin{aligned}\hat{a}_{\mathrm{D}}^{(\mathrm{R},c)} =& \sqrt{\frac{g_{\mathrm{P}}^2 N_{\mathrm{P}} + g_{\mathrm{R}}^2 (N_{\mathrm{R}}-1)}{g_{\mathrm{P}}^2 N_{\mathrm{P}} + g_{\mathrm{R}}^2 N_{\mathrm{R}}}}\hat{a}_{\mathrm{R},c} - \frac{g_{\mathrm{R}}^2}{\sqrt{g_{\mathrm{P}}^2 N_{\mathrm{P}} + g_{\mathrm{R}}^2 N_{\mathrm{R}}}} \frac{1}{\sqrt{g_{\mathrm{P}}^2 N_{\mathrm{P}} + g_{\mathrm{R}}^2 (N_{\mathrm{R}}-1)}} \sum_{i\neq c}^{N_{\mathrm{R}}} \hat{a}_{\mathrm{R},i} \\ &- \frac{g_{\mathrm{R}} g_{\mathrm{P}}}{\sqrt{g_{\mathrm{P}}^2 N_{\mathrm{P}} + g_{\mathrm{R}}^2 N_{\mathrm{R}}}} \frac{1}{\sqrt{g_{\mathrm{P}}^2 N_{\mathrm{P}} + g_{\mathrm{R}}^2 (N_{\mathrm{R}}-1)}} \sum_{j=1}^{N_{\mathrm{P}}} \hat{a}_{\mathrm{P},j}.\end{aligned} \tag{A.1}$$

Notice that, when $g_{\mathrm{P}} = 0$, this dark mode will not involve vibrations in the product molecules and when $g_{\mathrm{R}} = 0$, this dark mode will be the same as a vibration localized in the c^{th} molecule $\hat{a}_{\mathrm{D}}^{(\mathrm{R},c)} = \hat{a}_{\mathrm{R},c}$. Similarly, the bosonic operator for $\mathrm{D}'_{\mathrm{P},c}$, the dark mode highly localized in the c^{th} molecule after it has reacted and is in electronic state $|\mathrm{P}\rangle$ with total number of reactants $N_{\mathrm{R}} - 1$

and products $N_\mathrm{P}+1$ is

$$\begin{aligned}\hat{a}_\mathrm{D}^{(\mathrm{P},c)\prime} =& \sqrt{\frac{g_\mathrm{P}^2 N_\mathrm{P} + g_\mathrm{R}^2(N_\mathrm{R}-1)}{g_\mathrm{P}^2(N_\mathrm{P}+1) + g_\mathrm{R}^2(N_\mathrm{R}-1)}}\hat{a}_{\mathrm{P},c} \\ &- \frac{g_\mathrm{R} g_\mathrm{P}}{\sqrt{g_\mathrm{P}^2(N_\mathrm{P}+1) + g_\mathrm{R}^2(N_\mathrm{R}-1)}} \frac{1}{\sqrt{g_\mathrm{P}^2 N_\mathrm{P} + g_\mathrm{R}^2(N_\mathrm{R}-1)}} \sum_{i=1}^{N_\mathrm{R}-1} \hat{a}_{\mathrm{R},i} \\ &- \frac{g_\mathrm{P}^2}{\sqrt{g_\mathrm{P}^2(N_\mathrm{P}+1) + g_\mathrm{R}^2(N_\mathrm{R}-1)}} \frac{1}{\sqrt{g_\mathrm{P}^2 N_\mathrm{P} + g_\mathrm{R}^2(N_\mathrm{R}-1)}} \sum_{j\neq c}^{N_\mathrm{P}+1} \hat{a}_{\mathrm{P},j}.\end{aligned} \tag{A.2}$$

Here, when $g_\mathrm{P}=0$, the dark mode in equation (A.2) will be the same as a vibration localized in the c^{th} molecule $\hat{a}_\mathrm{D}^{(\mathrm{P},c)\prime} = \hat{a}_{\mathrm{P},c}$ and when $g_\mathrm{R}=0$, this dark mode will not involve vibrations in the reactant molecules.

A.2 Supplementary Note 2

We use Boltzmann rate equations as in [43, 148] to model polariton relaxation, and solve for the steady state of $N+1$ coupled differential equations. We assume that the scattering rate W_{ij} between polariton and dark modes is the same for all dark modes, labeled by k, this gives $W_{\mathrm{D}_k+} = W_{\mathrm{D}+}$ and $W_{-\mathrm{D}_k} = W_{-\mathrm{D}}$ [37]. Since our interests lie in the distribution of energy between polariton and dark modes rather than individual dark modes, we can simplify the problem by summing over all dark-mode equations and considering only their total population $n_\mathrm{D} = \sum_{k=2}^{N} n_\mathrm{D}^k$. We have the following rate equations for populations in the lower n_-, upper n_+ polaritons and all dark modes n_D,

$$\begin{aligned}\frac{dn_-}{dt} &= R_{-\mathrm{D}} + R_{-+} - \gamma_- n_- + P_-, \\ \frac{dn_\mathrm{D}}{dt} &= -R_{-\mathrm{D}} + R_{\mathrm{D}+} - \gamma_\mathrm{D}^k n_\mathrm{D}, \\ \frac{dn_+}{dt} &= -R_{-+} - R_{\mathrm{D}+} - \gamma_+ n_+,\end{aligned} \tag{A.3}$$

where

$$
\begin{aligned}
R_{-\mathrm{D}} =& W_{-\mathrm{D}_k}\Big(n_{\mathrm{D}}(1+n_-) - e^{-\beta\hbar(\Omega-\Delta)/2}(N-1+n_{\mathrm{D}})n_-\Big),\\
R_{-+} =& W_{-+}\Big(n_+(1+n_-) - e^{-\beta\hbar\Omega}(1+n_+)n_-\Big),\\
R_{\mathrm{D}+} =& W_{\mathrm{D}_k+}\Big(n_+(N-1+n_{\mathrm{D}}) - e^{-\beta\hbar(\Omega+\Delta)/2}(1+n_+)n_{\mathrm{D}}\Big).
\end{aligned}
\tag{A.4}
$$

The rate coefficients can be expressed as $W_{ij} = \alpha(1+n(\beta E_{ji}))$ and $W_{ji} = \alpha n(\beta E_{ji})$ where α is a temperature independent constant, $n(\beta E_{ji})$ is the average Bose-Einstein population at energy $E_{ji} = E_j - E_i$ where $E_j > E_i$ and inverse temperature $\beta = 1/k_{\mathrm{B}}T$. The rate coefficients W_{ij} should also depend on the low-frequency vibrational density of states, for simplicity, we take the spectral density to be flat.

For all calculations in the main manuscript, we use $\kappa = \Gamma_\downarrow$, $N = 10^7$ and $\alpha = 4.33\times10^{-6}\Gamma_\downarrow$ which corresponds to $(N-1)W_{\mathrm{D}_k-} = 100\Gamma_\downarrow$ ($\sim$ 1 ps) at room temperature for light-matter coupling strength $2\hbar g\sqrt{N} = 18.5$meV at zero detuning $\Delta = 0$. These values are similar to those in experiments $\kappa = 10^{10}$ s^{-1} ($\sim$ 100 ps), $\Gamma_\downarrow = 10^{10}$ s^{-1} ($\sim$ 100 ps), and scattering from LP to all dark modes $(N-1)W_{\mathrm{D}_k-} = 10^{12}$ s^{-1} ($\sim$ 1 ps) [40].

A.3 Supplementary Note 3

Dependence of the FC factors on LP population is shown in Fig. A.1 and they scale much better when the population in LP is large. We obtain an analytical expression for the Franck-Condon factor $|F^{f,0}_{\nu_+,\nu_-,\nu_{\mathrm{D}}}|^2$,

$$
\begin{aligned}
F^{f,0}_{\nu_+,\nu_-,\nu_{\mathrm{D}}} &= \langle 0, N_-, 0|\nu_+, \nu_-, \nu_{\mathrm{D}}\rangle'\\
&= \begin{cases}
\sqrt{e^{-S}S^f}\sqrt{\frac{N_-!}{\nu_+!\nu_-!\nu_{\mathrm{D}}!}}\tilde{w}^{-f} & \\
\Big[q^{N_-}\Big]\left((\tilde{x}+qx)^{\nu_+}(\tilde{y}+yq)^{\nu_-}(\tilde{z}-\tilde{z}q+zq)^{\nu_{\mathrm{D}}}\frac{\exp\left(\frac{-Swq}{1-q-wq}\right)}{(1-q-wq)^{f+1}}\right) & g_{\mathrm{P}}\neq 0\\
(-1)^{\nu_{\mathrm{D}}}\sqrt{\frac{N_-!}{\nu_+!\nu_-!(\nu_{\mathrm{D}}-f)!}}(x+\tilde{x})^{\nu_+}(y+\tilde{y})^{\nu_-}u^{\nu_{\mathrm{D}}-f}\left\langle(\nu_{\mathrm{D}}-f)_{\mathrm{R},c}\middle|(\nu_{\mathrm{D}})_{\mathrm{P},c}\right\rangle & g_{\mathrm{P}}=0
\end{cases}
\end{aligned}
\tag{A.5}
$$

where $[q^n]G(q)$ is the coefficient of q^n when you expand $G(q)$ as a Taylor series, and

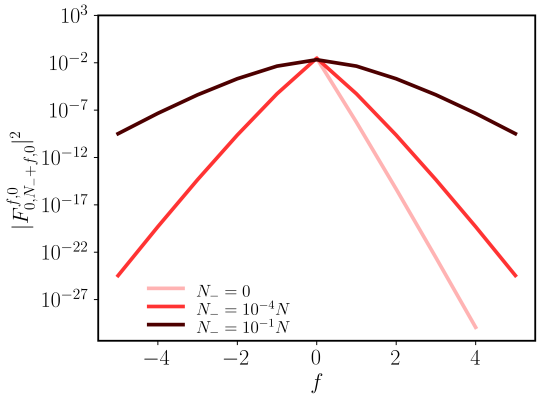

Figure A.1. Franck-Condon (FC) factors for different channels as a function of LP population. Reaction rate changes by the condensate occur due to channels featuring gain/loss f in vibrational quanta in the LP. The contribution of these channels is proportional to the corresponding FC factors and becomes more significant as the LP population N_- increases. Here, we show FC factors for $N_- = 0, 10^{-4}N, 10^{-1}N$ at resonance $\Delta = 0$ with symmetric light-matter coupling $2g_R\sqrt{N} = 2g_P\sqrt{N} = 0.1\omega_{vib}$ and Huang-Rhys factor $S = 3.5$.

$$
\begin{aligned}
u &= \left(-\cos\theta \frac{g_R}{\sqrt{g_R^2 N_R + g_P^2 N_P}} \right), \\
x &= \sin\theta\cos\theta', \\
y &= \sin\theta\sin\theta', \\
z &= \left(g_P \cos\theta \sqrt{\frac{g_R^2(N_R-1) + g_P^2 N_P}{(g_R^2(N_R-1) + g_P^2(N_P+1))(g_R^2 N_R + g_P^2 N_P)}} \right), \\
w &= \left(\frac{g_R g_P}{g_R^2(N_R-1) + g_P^2 N_P} \right), \\
\tilde{x} &= \left(\frac{-\cos\theta\sin\theta'(g_R^2(N_R-1) + g_P^2 N_P)}{\sqrt{g_R^2 N_R + g_P^2 N_P}\sqrt{g_R^2(N_R-1) + g_P^2(N_P+1)}} \right), \\
\tilde{y} &= \left(\frac{\cos\theta\cos\theta'(g_R^2(N_R-1) + g_P^2 N_P)}{\sqrt{g_R^2 N_R + g_P^2 N_P}\sqrt{g_R^2(N_R-1) + g_P^2(N_P+1)}} \right), \\
\tilde{z} &= \left(-\cos\theta \frac{g_R^2(N_R-1) + g_P^2 N_P}{g_P\sqrt{g_R^2 N_R + g_P^2 N_P}} \sqrt{\frac{g_R^2(N_R-1) + g_P^2 N_P}{g_R^2(N_R-1) + g_P^2(N_P+1)}} \right), \\
\tilde{w} &= \left(-\cos\theta \frac{g_R^2(N_R-1) + g_P^2 N_P}{g_P\sqrt{g_R^2 N_R + g_P^2 N_P}} \right).
\end{aligned}
\tag{A.6}
$$

We arrived at the expression in equation (A.5) by using generating functions and the Lagrange-Bürmann formula [60]. We then recursively compute $F^{f,n}_{\nu_+,\nu_-,\nu_\mathrm{D}}$ from $F^{f,0}_{\nu_+,\nu_-,\nu_\mathrm{D}}$ [57]. Using

$$\begin{bmatrix} \hat{a}_+ \\ \hat{a}_- \\ \hat{a}_\mathrm{D}^{(\mathrm{R},c)} \end{bmatrix} = \begin{bmatrix} J_{11} & J_{12} & J_{13} \\ J_{21} & J_{22} & J_{23} \\ J_{31} & J_{32} & J_{33} \end{bmatrix} \begin{bmatrix} \hat{a}'_+ \\ \hat{a}'_- \\ \hat{a}_\mathrm{D}^{(\mathrm{P},c)\prime} \end{bmatrix} + \begin{bmatrix} K_1 \\ K_2 \\ K_3 \end{bmatrix} \tag{A.7}$$

where

$$\begin{aligned}
J_{11} &= \cos\theta\cos\theta' + \sin\theta\sin\theta'\left(\frac{g_\mathrm{R}^2(N_\mathrm{R}-1)+g_\mathrm{P}^2N_\mathrm{P}+g_\mathrm{R}g_\mathrm{P}}{\sqrt{g_\mathrm{R}^2N_\mathrm{R}+g_\mathrm{P}^2N_\mathrm{P}}\sqrt{g_\mathrm{R}^2(N_\mathrm{R}-1)+g_\mathrm{P}^2(N_\mathrm{P}+1)}}\right) \\
J_{12} &= \sin\theta'\cos\theta - \cos\theta'\sin\theta\left(\frac{g_\mathrm{R}^2(N_\mathrm{R}-1)+g_\mathrm{P}^2N_\mathrm{P}+g_\mathrm{R}g_\mathrm{P}}{\sqrt{g_\mathrm{R}^2N_\mathrm{R}+g_\mathrm{P}^2N_\mathrm{P}}\sqrt{g_\mathrm{R}^2(N_\mathrm{R}-1)+g_\mathrm{P}^2(N_\mathrm{P}+1)}}\right) \\
J_{13} &= \sin\theta\left(\frac{(g_\mathrm{R}-g_\mathrm{P})\sqrt{g_\mathrm{R}^2(N_\mathrm{R}-1)+g_\mathrm{P}^2N_\mathrm{P}}}{\sqrt{g_\mathrm{R}^2N_\mathrm{R}+g_\mathrm{P}^2N_\mathrm{P}}\sqrt{g_\mathrm{R}^2(N_\mathrm{R}-1)+g_\mathrm{P}^2(N_\mathrm{P}+1)}}\right) \\
J_{21} &= \cos\theta'\sin\theta - \sin\theta'\cos\theta\left(\frac{g_\mathrm{R}^2(N_\mathrm{R}-1)+g_\mathrm{P}^2N_\mathrm{P}+g_\mathrm{R}g_\mathrm{P}}{\sqrt{g_\mathrm{R}^2N_\mathrm{R}+g_\mathrm{P}^2N_\mathrm{P}}\sqrt{g_\mathrm{R}^2(N_\mathrm{R}-1)+g_\mathrm{P}^2(N_\mathrm{P}+1)}}\right) \\
J_{22} &= \sin\theta\sin\theta' + \cos\theta\cos\theta'\left(\frac{g_\mathrm{R}^2(N_\mathrm{R}-1)+g_\mathrm{P}^2N_\mathrm{P}+g_\mathrm{R}g_\mathrm{P}}{\sqrt{g_\mathrm{R}^2N_\mathrm{R}+g_\mathrm{P}^2N_\mathrm{P}}\sqrt{g_\mathrm{R}^2(N_\mathrm{R}-1)+g_\mathrm{P}^2(N_\mathrm{P}+1)}}\right) \\
J_{23} &= -\cos\theta\left(\frac{(g_\mathrm{R}-g_\mathrm{P})\sqrt{g_\mathrm{R}^2(N_\mathrm{R}-1)+g_\mathrm{P}^2N_\mathrm{P}}}{\sqrt{g_\mathrm{R}^2N_\mathrm{R}+g_\mathrm{P}^2N_\mathrm{P}}\sqrt{g_\mathrm{R}^2(N_\mathrm{R}-1)+g_\mathrm{P}^2(N_\mathrm{P}+1)}}\right)
\end{aligned} \tag{A.8}$$

and

$$
\begin{aligned}
J_{31} &= -\sin\theta' \left(\frac{(g_{\mathrm{R}} - g_{\mathrm{P}})\sqrt{g_{\mathrm{R}}^2(N_{\mathrm{R}}-1) + g_{\mathrm{P}}^2 N_{\mathrm{P}}}}{\sqrt{g_{\mathrm{R}}^2 N_{\mathrm{R}} + g_{\mathrm{P}}^2 N_{\mathrm{P}}}\sqrt{g_{\mathrm{R}}^2(N_{\mathrm{R}}-1) + g_{\mathrm{P}}^2(N_{\mathrm{P}}+1)}} \right) \\
J_{32} &= \cos\theta' \left(\frac{(g_{\mathrm{R}} - g_{\mathrm{P}})\sqrt{g_{\mathrm{R}}^2(N_{\mathrm{R}}-1) + g_{\mathrm{P}}^2 N_{\mathrm{P}}}}{\sqrt{g_{\mathrm{R}}^2 N_{\mathrm{R}} + g_{\mathrm{P}}^2 N_{\mathrm{P}}}\sqrt{g_{\mathrm{R}}^2(N_{\mathrm{R}}-1) + g_{\mathrm{P}}^2(N_{\mathrm{P}}+1)}} \right) \\
J_{33} &= \left(\frac{g_{\mathrm{R}}^2(N_{\mathrm{R}}-1) + g_{\mathrm{P}}^2 N_{\mathrm{P}} + g_{\mathrm{R}} g_{\mathrm{P}}}{\sqrt{g_{\mathrm{R}}^2 N_{\mathrm{R}} + g_{\mathrm{P}}^2 N_{\mathrm{P}}}\sqrt{g_{\mathrm{R}}^2(N_{\mathrm{R}}-1) + g_{\mathrm{P}}^2(N_{\mathrm{P}}+1)}} \right) \\
K_1 &= -\sin\theta \frac{g_{\mathrm{R}}}{\sqrt{g_{\mathrm{R}}^2 N_{\mathrm{R}} + g_{\mathrm{P}}^2 N_{\mathrm{P}}}}\sqrt{S} \\
K_2 &= \cos\theta \frac{g_{\mathrm{R}}}{\sqrt{g_{\mathrm{R}}^2 N_{\mathrm{R}} + g_{\mathrm{P}}^2 N_{\mathrm{P}}}}\sqrt{S} \\
K_3 &= -\sqrt{\frac{g_{\mathrm{R}}^2(N_{\mathrm{R}}-1) + g_{\mathrm{P}}^2 N_{\mathrm{P}}}{g_{\mathrm{R}}^2 N_{\mathrm{R}} + g_{\mathrm{P}}^2 N_{\mathrm{P}}}}\sqrt{S}
\end{aligned}
\tag{A.9}
$$

we get the recursive formula

$$
F^{f,n+1}_{\nu_+,\nu_-,\nu_{\mathrm{D}}} = \frac{1}{\sqrt{n+1}} \left(J_{31}\sqrt{\nu_+} F^{f,n}_{\nu_+-1,\nu_-,\nu_{\mathrm{D}}} + F^{f,n}_{\nu_+,\nu_--1,\nu_{\mathrm{D}}} J_{32}\sqrt{\nu_-} + J_{33}\sqrt{\nu_{\mathrm{D}}} F^{f,n}_{\nu_+,\nu_-,\nu_{\mathrm{D}}-1} + K_3 F^{f-1,n}_{\nu_+,\nu_-,\nu_{\mathrm{D}}} \right).
\tag{A.10}
$$

To derive equation (A.5), we write the initial and final vibrational states in terms of creation/annihilation operators for the upper, lower polaritons and dark modes

$$
F^{f,0}_{\nu_+,\nu_-,\nu_{\mathrm{D}}} = \left\langle 0_+ 0_- 0_{\mathrm{D}}^{(\mathrm{R},c)} \right| \frac{\left(\hat{a}_-\right)^{N_-}}{\sqrt{N_-!}} \frac{\left(\hat{a}_+'^{\dagger}\right)^{\nu_+}}{\sqrt{\nu_+!}} \frac{\left(\hat{a}_-'^{\dagger}\right)^{\nu_-}}{\sqrt{\nu_-!}} \frac{\left(\hat{a}_{\mathrm{D}}^{(\mathrm{P},c)\prime\dagger}\right)^{\nu_{\mathrm{D}}}}{\sqrt{\nu_{\mathrm{D}}!}} \left| 0'_+ 0'_- 0_{\mathrm{D}}^{(\mathrm{P},c)\prime} \right\rangle .
\tag{A.11}
$$

Writing the polariton modes as a linear combination of the photon $\hat{a}_{\mathrm{ph}}$ and bright modes $\hat{a}_{\mathrm{B}(N_{\mathrm{R}},N_{\mathrm{P}})}$,

$\hat{a}_{\mathrm{B}(N_\mathrm{R}-1,N_\mathrm{P}+1)}$,

$$
\begin{aligned}
F^{f,0}_{\nu_+,\nu_-,\nu_\mathrm{D}} =& \frac{1}{\sqrt{N_-!\nu_+!\nu_-!\nu_\mathrm{D}!}} \left\langle 0_\mathrm{ph} 0_{\mathrm{B}(N_\mathrm{R},N_\mathrm{P})} 0_\mathrm{D}^{(\mathrm{R},c)} \right| \left(\sin\theta \hat{a}_\mathrm{ph} - \cos\theta \hat{a}_{\mathrm{B}(N_\mathrm{R},N_\mathrm{P})} \right)^{N_-} \\
& \left(\cos\theta' \hat{a}^\dagger_\mathrm{ph} + \sin\theta' \hat{a}^\dagger_{\mathrm{B}(N_\mathrm{R}-1,N_\mathrm{P}+1)} \right)^{\nu_+} \left(\sin\theta' \hat{a}^\dagger_\mathrm{ph} - \cos\theta' \hat{a}^\dagger_{\mathrm{B}(N_\mathrm{R}-1,N_\mathrm{P}+1)} \right)^{\nu_-} \\
& \left(\hat{a}^{(\mathrm{P},c)\prime\dagger}_\mathrm{D} \right)^{\nu_\mathrm{D}} \left| 0_\mathrm{ph} 0_{\mathrm{B}(N_\mathrm{R}-1,N_\mathrm{P}+1)} 0_\mathrm{D}^{(\mathrm{P},c)\prime} \right\rangle .
\end{aligned}
\tag{A.12}
$$

Here, $\left[\hat{a}_\mathrm{ph}, \hat{a}_{\mathrm{B}(N_\mathrm{R},N_\mathrm{P})}\right] = 0$ and $\left[\hat{a}_\mathrm{ph}, \hat{a}_{\mathrm{B}(N_\mathrm{R}-1,N_\mathrm{P}+1)}\right] = 0$, so we can use the binomial theorem and collect these operators,

$$
\begin{aligned}
F^{f,0}_{\nu_+,\nu_-,\nu_\mathrm{D}} =& \frac{1}{\sqrt{N_-!\nu_+!\nu_-!\nu_\mathrm{D}!}} \sum_{l=0}^{N_-} \sum_{m=0}^{\nu_+} \sum_{n=0}^{\nu_-} \binom{N_-}{l} \binom{\nu_+}{m} \binom{\nu_-}{n} \left\langle 0_\mathrm{ph} 0_{\mathrm{B}(N_\mathrm{R},N_\mathrm{P})} 0_\mathrm{D}^{(\mathrm{R},c)} \right| \left(\sin\theta \hat{a}_\mathrm{ph} \right)^l \\
& \times \left(- \cos\theta \hat{a}_{\mathrm{B}(N_\mathrm{R},N_\mathrm{P})} \right)^{N_- - l} \left(\cos\theta' \hat{a}^\dagger_\mathrm{ph} \right)^m \left(\sin\theta' \hat{a}^\dagger_{\mathrm{B}(N_\mathrm{R}-1,N_\mathrm{P}+1)} \right)^{\nu_+ - m} \left(\sin\theta' \hat{a}^\dagger_\mathrm{ph} \right)^n \\
& \times \left(- \cos\theta' \hat{a}^\dagger_{\mathrm{B}(N_\mathrm{R}-1,N_\mathrm{P}+1)} \right)^{\nu_- - n} \left(\hat{a}^{(\mathrm{P},c)\prime\dagger}_\mathrm{D} \right)^{\nu_\mathrm{D}} \left| 0_\mathrm{ph} 0_{\mathrm{B}(N_\mathrm{R}-1,N_\mathrm{P}+1)} 0_\mathrm{D}^{(\mathrm{P},c)\prime} \right\rangle .
\end{aligned}
\tag{A.13}
$$

The only non-vanishing terms in the above summation will be those with equal number of photon creation and annihilation operators $l = m + n$, since the photon mode does not get displaced during the chemical reaction, the overlap is non-zero only when the initial and final states are exactly the same. Plugging in $l = m + n$ and $\left\langle 0_\mathrm{ph} \right| (\hat{a}_\mathrm{ph})^l (\hat{a}^\dagger_\mathrm{ph})^{m+n} \left| 0_\mathrm{ph} \right\rangle = (m+n)!$

$$
\begin{aligned}
F^{f,0}_{\nu_+,\nu_-,\nu_\mathrm{D}} =& \frac{1}{\sqrt{N_-!\nu_+!\nu_-!\nu_\mathrm{D}!}} \sum_{m=0}^{\nu_+} \sum_{n=0}^{\nu_-} \binom{N_-}{m+n} \binom{\nu_+}{m} \binom{\nu_-}{n} \left(\sin\theta \right)^{m+n} \left(\cos\theta' \right)^m \left(\sin\theta' \right)^n \\
& \left(- \cos\theta \right)^{N_- - m - n} \left(\sin\theta' \right)^{\nu_+ - m} \left(- \cos\theta' \right)^{\nu_- - n} (m+n)! \\
& \left\langle 0_{\mathrm{B}(N_\mathrm{R},N_\mathrm{P})} 0_\mathrm{D}^{(\mathrm{R},c)} \right| \left(\hat{a}_{\mathrm{B}(N_\mathrm{R},N_\mathrm{P})} \right)^{N_- - m - n} \left(\hat{a}^\dagger_{\mathrm{B}(N_\mathrm{R}-1,N_\mathrm{P}+1)} \right)^{(\nu_+ + \nu_-) - (m+n)} \\
& \left(\hat{a}^{(\mathrm{P},c)\prime\dagger}_\mathrm{D} \right)^{\nu_\mathrm{D}} \left| 0_{\mathrm{B}(N_\mathrm{R}-1,N_\mathrm{P}+1)} 0_\mathrm{D}^{(\mathrm{P},c)\prime} \right\rangle
\end{aligned}
\tag{A.14}
$$

Rewriting the initial bright mode $\hat{a}_{\mathrm{B}(N_\mathrm{R},N_\mathrm{P})}$, final bright mode $\hat{a}_{\mathrm{B}(N_\mathrm{R}-1,N_\mathrm{P}+1)}$, and the highly localized final dark mode $\hat{a}^{(\mathrm{P},c)\prime}_\mathrm{D}$ in terms of a bright mode involving all molecules other than the reacting molecule $\hat{a}_{\mathrm{B}(N_\mathrm{R}-1,N_\mathrm{P})} = \frac{1}{\sqrt{g_\mathrm{R}^2(N_\mathrm{R}-1)+g_\mathrm{P}^2 N_\mathrm{P}}} \left[g_\mathrm{R} \sum_{i=1}^{N_\mathrm{R}-1} a_{\mathrm{R},i} + g_\mathrm{P} \sum_{j=1}^{N_\mathrm{P}} a_{\mathrm{P},j} \right]$, and vibrational

modes of this molecule $\hat{a}_{\mathrm{P},c}$ and $\hat{a}_{\mathrm{R},c}$ we obtain

$$
\begin{aligned}
F^{f,0}_{\nu_+,\nu_-,\nu_\mathrm{D}} =& \frac{1}{\sqrt{N_-!\nu_+!\nu_-!\nu_\mathrm{D}!}} \sum_{m=0}^{\nu_+} \sum_{n=0}^{\nu_-} \binom{N_-}{m+n} \binom{\nu_+}{m} \binom{\nu_-}{n} \Big(\sin\theta\Big)^{m+n} \Big(\cos\theta'\Big)^{m} \Big(\sin\theta'\Big)^{n} \\
& \times \Big(-\cos\theta\Big)^{N_- - m - n} \Big(\sin\theta'\Big)^{\nu_+ - m} \Big(-\cos\theta'\Big)^{\nu_- - n} (m+n)! \\
& \times \Big\langle 0_{\mathrm{B}(N_\mathrm{R}-1,N_\mathrm{P})} 0_{\mathrm{R},c} \Big| \Bigg[\sqrt{\frac{g_\mathrm{R}^2(N_\mathrm{R}-1) + g_\mathrm{P}^2 N_\mathrm{P}}{g_\mathrm{R}^2 N_\mathrm{R} + g_\mathrm{P}^2 N_\mathrm{P}}} \hat{a}_{\mathrm{B}(N_\mathrm{R}-1,N_\mathrm{P})} \\
& + \frac{g_\mathrm{R}}{\sqrt{g_\mathrm{R}^2 N_\mathrm{R} + g_\mathrm{P}^2 N_\mathrm{P}}} \hat{a}_{\mathrm{R},c} \Bigg]^{N_- - m - n} \\
& \times \Bigg[\sqrt{\frac{g_\mathrm{R}^2(N_\mathrm{R}-1) + g_\mathrm{P}^2 N_\mathrm{P}}{g_\mathrm{R}^2(N_\mathrm{R}-1) + g_\mathrm{P}^2(N_\mathrm{P}+1)}} \hat{a}^\dagger_{\mathrm{B}(N_\mathrm{R}-1,N_\mathrm{P})} \\
& + \frac{g_\mathrm{P}}{\sqrt{g_\mathrm{R}^2(N_\mathrm{R}-1) + g_\mathrm{P}^2(N_\mathrm{P}+1)}} \hat{a}^\dagger_{\mathrm{P},c} \Bigg]^{(\nu_+ + \nu_-) - (m+n)} \\
& \times \Bigg[- \frac{g_\mathrm{P}}{\sqrt{g_\mathrm{R}^2(N_\mathrm{R}-1) + g_\mathrm{P}^2(N_\mathrm{P}+1)}} \hat{a}^\dagger_{\mathrm{B}(N_\mathrm{R}-1,N_\mathrm{P})} \\
& + \sqrt{\frac{g_\mathrm{R}^2(N_\mathrm{R}-1) + g_\mathrm{P}^2 N_\mathrm{P}}{g_\mathrm{R}^2(N_\mathrm{R}-1) + g_\mathrm{P}^2(N_\mathrm{P}+1)}} \hat{a}^\dagger_{\mathrm{P},c} \Bigg]^{\nu_\mathrm{D}} \Big| 0_{\mathrm{B}(N_\mathrm{R}-1,N_\mathrm{P})} 0_{\mathrm{P},c} \Big\rangle \,.
\end{aligned}
\tag{A.15}
$$

Since $\left[\hat{a}_{\mathrm{B}(N_\mathrm{R}-1,N_\mathrm{P})}, \hat{a}_{\mathrm{R},c}\right] = 0$ and $\left[\hat{a}_{\mathrm{B}(N_\mathrm{R}-1,N_\mathrm{P})}, \hat{a}_{\mathrm{P},c}\right] = 0$, we can use the binomial expansion

again

$$
\begin{aligned}
F^{f,0}_{\nu_+,\nu_-,\nu_\mathrm{D}} =& \frac{1}{\sqrt{N_-!\nu_+!\nu_-!\nu_\mathrm{D}!}} \sum_{m=0}^{\nu_+} \sum_{n=0}^{\nu_-} \sum_{r=0}^{N_--m-n} \sum_{p=0}^{(\nu_++\nu_-)-(m+n)} \sum_{q=0}^{\nu_\mathrm{D}} \binom{N_-}{m+n}\binom{\nu_+}{m}\binom{\nu_-}{n}\binom{N_--m-n}{r} \\
&\times \binom{(\nu_++\nu_-)-(m+n)}{p}\binom{\nu_\mathrm{D}}{q}\Big(\sin\theta\Big)^{m+n}\Big(\cos\theta'\Big)^{m}\Big(\sin\theta'\Big)^{n}(m+n)! \\
&\times \Big(-\cos\theta\Big)^{N_--m-n}\Big(\sin\theta'\Big)^{\nu_+-m}\Big(-\cos\theta'\Big)^{\nu_--n}(-1)^q \\
&\times \left[\frac{g_\mathrm{P}}{\sqrt{g_\mathrm{R}^2(N_\mathrm{R}-1)+g_\mathrm{P}^2(N_\mathrm{P}+1)}}\right]^{(\nu_++\nu_-+q)-(m+n+p)} \\
&\times \left[\sqrt{\frac{g_\mathrm{R}^2(N_\mathrm{R}-1)+g_\mathrm{P}^2N_\mathrm{P}}{g_\mathrm{R}^2(N_\mathrm{R}-1)+g_\mathrm{P}^2(N_\mathrm{P}+1)}}\right]^{\nu_\mathrm{D}+p-q} \\
&\times \left[\sqrt{\frac{g_\mathrm{R}^2(N_\mathrm{R}-1)+g_\mathrm{P}^2N_\mathrm{P}}{g_\mathrm{R}^2N_\mathrm{R}+g_\mathrm{P}^2N_\mathrm{P}}}\right]^{r}\left[\frac{g_\mathrm{R}}{\sqrt{g_\mathrm{R}^2N_\mathrm{R}+g_\mathrm{P}^2N_\mathrm{P}}}\right]^{N_--m-n-r} \Big\langle 0_{\mathrm{B}(N_\mathrm{R}-1,N_\mathrm{P})}0_{\mathrm{R},c}\Big| \\
&\times \Big(\hat{a}_{\mathrm{B}(N_\mathrm{R}-1,N_\mathrm{P})}\Big)^{r}\Big(\hat{a}_{\mathrm{R},c}\Big)^{N_--m-n-r}\Big(\hat{a}^\dagger_{\mathrm{B}(N_\mathrm{R}-1,N_\mathrm{P})}\Big)^{p+q} \\
&\times \Big(\hat{a}^\dagger_{\mathrm{P},c}\Big)^{(\nu_++\nu_-+\nu_\mathrm{D})-(m+n+p+q)} \Big|0_{\mathrm{B}(N_\mathrm{R}-1,N_\mathrm{P})}0_{\mathrm{P},c}\Big\rangle .
\end{aligned}
\tag{A.16}
$$

The vibrational modes of all molecules other than the reacting molecule are not modified by the chemical reaction, therefore, non-zero terms in the summation satisfy $r = p + q$. Plugging in $r = p + q$ and $\Big\langle 0_{\mathrm{B}(N_\mathrm{R}-1,N_\mathrm{P})}\Big| (\hat{a}_{\mathrm{B}(N_\mathrm{R}-1,N_\mathrm{P})})^r (\hat{a}^\dagger_{\mathrm{B}(N_\mathrm{R}-1,N_\mathrm{P})})^{p+q} \Big|0_{\mathrm{B}(N_\mathrm{R}-1,N_\mathrm{P})}\Big\rangle = (p+q)!$,

$$
\begin{aligned}
F^{f,0}_{\nu_+,\nu_-,\nu_{\mathrm{D}}} =& \frac{1}{\sqrt{N_-!\nu_+!\nu_-!\nu_{\mathrm{D}}!}} \sum_{m=0}^{\nu_+} \sum_{n=0}^{\nu_-} \sum_{p=0}^{(\nu_+ + \nu_-)-(m+n)} \sum_{q=0}^{\nu_{\mathrm{D}}} \binom{N_-}{m+n} \binom{\nu_+}{m} \binom{\nu_-}{n} \binom{N_- - (m+n)}{p+q} \binom{\nu_{\mathrm{D}}}{q} \\
& \times \binom{(\nu_+ + \nu_-) - (m+n)}{p} \Big(\sin\theta\Big)^{m+n} \Big(\cos\theta'\Big)^{m} \Big(\sin\theta'\Big)^{n} (m+n)!(p+q)! \\
& \times \Big(-\cos\theta\Big)^{N_- - (m+n)} \Big(\sin\theta'\Big)^{\nu_+ - m} \Big(-\cos\theta'\Big)^{\nu_- - n} (-1)^q \\
& \times \left[\frac{g_{\mathrm{P}}}{\sqrt{g_{\mathrm{R}}^2(N_{\mathrm{R}}-1) + g_{\mathrm{P}}^2(N_{\mathrm{P}}+1)}}\right]^{(\nu_+ + \nu_- + q) - (m+n+p)} \\
& \times \left[\sqrt{\frac{g_{\mathrm{R}}^2(N_{\mathrm{R}}-1) + g_{\mathrm{P}}^2 N_{\mathrm{P}}}{g_{\mathrm{R}}^2(N_{\mathrm{R}}-1) + g_{\mathrm{P}}^2(N_{\mathrm{P}}+1)}}\right]^{\nu_{\mathrm{D}} + p - q} \left[\sqrt{\frac{g_{\mathrm{R}}^2(N_{\mathrm{R}}-1) + g_{\mathrm{P}}^2 N_{\mathrm{P}}}{g_{\mathrm{R}}^2 N_{\mathrm{R}} + g_{\mathrm{P}}^2 N_{\mathrm{P}}}}\right]^{p+q} \\
& \times \left[\frac{g_{\mathrm{R}}}{\sqrt{g_{\mathrm{R}}^2 N_{\mathrm{R}} + g_{\mathrm{P}}^2 N_{\mathrm{P}}}}\right]^{N_- - (m+n+p+q)} \Big\langle 0_{\mathrm{R},c}\Big| \Big(\hat{a}_{\mathrm{R},c}\Big)^{N_- - (m+n+p+q)} \\
& \times \Big(\hat{a}^{\dagger}_{\mathrm{P},c}\Big)^{(\nu_+ + \nu_- + \nu_{\mathrm{D}}) - (m+n+p+q)} \Big|0_{\mathrm{P},c}\Big\rangle
\end{aligned}
\tag{A.17}
$$

Changing variables from $\{m, n, q, p\}$ to $\{i, j, k, h\}$, where $i = \nu_+ - m$, $j = \nu_- - n$, $k = \nu_{\mathrm{D}} - q$,

$h = N_- - m - n - p - q$ and $f = \nu_+ + \nu_- + \nu_D - N_-$,

$$
\begin{aligned}
F^{f,0}_{\nu_+,\nu_-,\nu_D} =& \sqrt{\frac{N_-!}{\nu_+!\nu_-!\nu_D!}}\left(-\cos\theta\frac{g_R^2(N_R-1)+g_P^2N_P}{g_P\sqrt{g_R^2N_R+g_P^2N_P}}\right)^{-f}\sum_{i=0}^{\nu_+}\sum_{j=0}^{\nu_-}\sum_{k=0}^{\nu_D}\sum_{h=k-f}^{i+j+k-f}\binom{\nu_+}{i}\binom{\nu_-}{j}\\
&\times\binom{i+j}{h+f-k}\binom{\nu_D}{k}\left(\frac{g_Rg_P}{g_R^2(N_R-1)+g_P^2N_P}\right)^h\Big(\sin\theta\cos\theta'\Big)^{\nu_+-i}\\
&\left(\frac{-\cos\theta\sin\theta'(g_R^2(N_R-1)+g_P^2N_P)}{\sqrt{g_R^2N_R+g_P^2N_P}\sqrt{g_R^2(N_R-1)+g_P^2(N_P+1)}}\right)^i\Big(\sin\theta\sin\theta'\Big)^{\nu_--j}\\
&\times\left(\frac{\cos\theta\cos\theta'(g_R^2(N_R-1)+g_P^2N_P)}{\sqrt{g_R^2N_R+g_P^2N_P}\sqrt{g_R^2(N_R-1)+g_P^2(N_P+1)}}\right)^j\\
&\times\left(g_P\cos\theta\sqrt{\frac{g_R^2(N_R-1)+g_P^2N_P}{(g_R^2(N_R-1)+g_P^2(N_P+1))(g_R^2N_R+g_P^2N_P)}}\right)^{\nu_D-k}\\
&\times\left(-\cos\theta\frac{g_R^2(N_R-1)+g_P^2N_P}{g_P\sqrt{g_R^2N_R+g_P^2N_P}}\sqrt{\frac{g_R^2(N_R-1)+g_P^2N_P}{g_R^2(N_R-1)+g_P^2(N_P+1)}}\right)^k\\
&\times\frac{1}{h!}\left\langle 0_{R,c}\right|\left(\hat{a}_{R,c}\right)^h\left(\hat{a}^\dagger_{P,c}\right)^{h+f}\left|0_{P,c}\right\rangle
\end{aligned}
\tag{A.18}
$$

The above expression is valid only when $g_P \neq 0$. The case of $g_P = 0$ is explained in Subsection *1*.

Remembering the definitions of variables x, y, z, w and $\tilde{x}, \tilde{y}, \tilde{z}$ from equation (A.6),

$$
\begin{aligned}
F^{f,0}_{\nu_+,\nu_-,\nu_D} =& \sqrt{\frac{N_-!}{\nu_+!\nu_-!\nu_D!}}\tilde{w}^{-f}\sum_{i=0}^{\nu_+}\sum_{j=0}^{\nu_-}\sum_{k=0}^{\nu_D}\sum_{h=k-f}^{i+j+k-f}\binom{\nu_+}{i}\binom{\nu_-}{j}\binom{i+j}{h+f-k}\binom{\nu_D}{k}\\
&\times x^{\nu_+-i}y^{\nu_--j}z^{\nu_D-k}\tilde{x}^i\tilde{y}^j\tilde{z}^kw^h\sqrt{\frac{(h+f)!}{h!}}\left\langle h_{R,c}\middle|(h+f)_{P,c}\right\rangle
\end{aligned}
\tag{A.19}
$$

This is not easy to evaluate because of the summation over h involves the term $\left\langle h_{R,c}\middle|(h+f)_{P,c}\right\rangle$.

Substituting $\left\langle h_{\mathrm{R},c}\middle|(h+f)_{\mathrm{P},c}\right\rangle = \sqrt{\frac{(h+f)!}{h!}}\sqrt{\frac{e^{-S}}{S^f}}\hat{O}_f(S)\sum_{u=0}^{h}\binom{h}{u}\frac{(-S)^u}{u!}$,

$$\begin{aligned}F^{f,0}_{\nu_+,\nu_-,\nu_\mathrm{D}} =&\sqrt{\frac{N_-!}{\nu_+!\nu_-!\nu_\mathrm{D}!}}\tilde{w}^{-f}\sum_{i=0}^{\nu_+}\sum_{j=0}^{\nu_-}\sum_{k=0}^{\nu_\mathrm{D}}\sum_{h=k-f}^{i+j+k-f}\binom{\nu_+}{i}\binom{\nu_-}{j}\binom{i+j}{h+f-k}\binom{\nu_\mathrm{D}}{k}\\&\times x^{\nu_+-i}y^{\nu_--j}z^{\nu_\mathrm{D}-k}\tilde{x}^i\tilde{y}^j\tilde{z}^k w^h\frac{(h+f)!}{h!}\sqrt{\frac{e^{-S}}{S^f}}\hat{O}_f(S)\sum_{u=0}^{h}\binom{h}{u}\frac{(-S)^u}{u!}.\end{aligned} \tag{A.20}$$

Rewriting $(h+f)!w^h/h!$ as $\hat{T}_f(w)w^h$,

$$\begin{aligned}F^{f,0}_{\nu_+,\nu_-,\nu_\mathrm{D}} =&\sqrt{\frac{e^{-S}}{S^f}}\hat{O}_f(S)\sqrt{\frac{N_-!}{\nu_+!\nu_-!\nu_\mathrm{D}!}}\tilde{w}^{-f}\sum_{i=0}^{\nu_+}\sum_{j=0}^{\nu_-}\sum_{k=0}^{\nu_\mathrm{D}}\sum_{h=k-f}^{i+j+k-f}\sum_{u=0}^{h}\binom{\nu_+}{i}\binom{\nu_-}{j}\binom{i+j}{h+f-k}\binom{\nu_\mathrm{D}}{k}\binom{h}{u}\\&\times\frac{(-S)^u}{u!}x^{\nu_+-i}y^{\nu_--j}z^{\nu_\mathrm{D}-k}\tilde{x}^i\tilde{y}^j\tilde{z}^k\hat{T}_f(w)w^h.\end{aligned} \tag{A.21}$$

With the operators $\hat{O}_f(S)$ and $\hat{T}_f(w)$ defined as:

$$\begin{aligned}\hat{O}_f(S) &= \begin{cases}\left(\int dS\right)^f & f\geq 0\\ \left(\frac{d}{dS}\right)^{-f} & f<0\end{cases}\\ \hat{T}_f(w) &= \begin{cases}\left(\frac{d}{dw}\right)^f w^f & f\geq 0\\ \left(\int dw\right)^{-f} w^f & f<0\end{cases}\end{aligned} \tag{A.22}$$

This simplifies to

$$\begin{aligned}F^{f,0}_{\nu_+,\nu_-,\nu_\mathrm{D}} &= \sqrt{\frac{e^{-S}}{S^f}}\sqrt{\frac{N_-!}{\nu_+!\nu_-!\nu_\mathrm{D}!}}\tilde{w}^{-f}\hat{O}_f(S)\hat{T}_f(w)\\&\quad\sum_{i=0}^{\nu_+}\sum_{j=0}^{\nu_-}\sum_{k=0}^{\nu_\mathrm{D}}\sum_{h=k-f}^{i+j+k-f}\sum_{u=0}^{h}\binom{\nu_+}{i}\binom{\nu_-}{j}\binom{i+j}{h+f-k}\binom{\nu_\mathrm{D}}{k}\binom{h}{u}\\&\quad\times\frac{(-S)^u}{u!}x^{\nu_+-i}y^{\nu_--j}z^{\nu_\mathrm{D}-k}\tilde{x}^i\tilde{y}^j\tilde{z}^k w^h,\\&= \sqrt{\frac{e^{-S}}{S^f}}\sqrt{\frac{N_-!}{\nu_+!\nu_-!\nu_\mathrm{D}!}}\tilde{w}^{-f}\hat{O}_f(S)\hat{T}_f(w)M^f_{\nu_+,\nu_-,\nu_\mathrm{D}}.\end{aligned} \tag{A.23}$$

Here we introduce $M^{f}_{\nu_+,\nu_-,\nu_D}$ as the part involving the summation in $F^{f,0}_{\nu_+,\nu_-,\nu_D}$ for more readability. Evaluating $M^{f}_{\nu_+,\nu_-,\nu_D}$,

$$\begin{aligned} M^{f}_{\nu_+,\nu_-,\nu_D} &= \sum_{i=0}^{\nu_+}\sum_{j=0}^{\nu_-}\sum_{k=0}^{\nu_D}\sum_{h=k-f}^{i+j+k-f}\sum_{u=0}^{h}\binom{\nu_+}{i}\binom{\nu_-}{j}\binom{i+j}{i+j+k-f-h}\binom{\nu_D}{k} \\ &\quad\times\binom{h}{u}\frac{(-S)^u}{u!}x^{\nu_+-i}y^{\nu_--j}z^{\nu_D-k}\tilde{x}^i\tilde{y}^j\tilde{z}^k w^h \\ &= \sum_{i=0}^{\nu_+}\binom{\nu_+}{i}\tilde{x}^i x^{\nu_+-i}\sum_{j=0}^{\nu_-}\binom{\nu_-}{j}\tilde{y}^j y^{\nu_--j}\sum_{k=0}^{\nu_D}\binom{\nu_D}{k}\tilde{z}^k z^{\nu_D-k} \\ &\quad\times\sum_{h=k-f}^{i+j+k-f}\binom{i+j}{i+j+k-f-h}w^h\sum_{u=0}^{h}\binom{h}{u}\frac{(-S)^u}{u!} \end{aligned} \tag{A.24}$$

We first focus on evaluating the summation over u. Without $u!$ in the denominator, this would have simply been a binomial expansion. The $u!$ makes it difficult to evaluate, but each term in the summation looks like the product of terms from a binomial $\binom{h}{u}$ and exponential $(-S)^u/u!$ expansion. We can use the powerful combinatorial technique of generating functions to evaluate the summation. Here, t is a dummy variable that we introduce to count the terms,

$$\begin{aligned} M^{f}_{\nu_+,\nu_-,\nu_D} &= \sum_{i=0}^{\nu_+}\binom{\nu_+}{i}\tilde{x}^i x^{\nu_+-i}\sum_{j=0}^{\nu_-}\binom{\nu_-}{j}\tilde{y}^j y^{\nu_--j}\sum_{k=0}^{\nu_D}\binom{\nu_D}{k}\tilde{z}^k z^{\nu_D-k} \\ &\quad\times\sum_{h=k-f}^{i+j+k-f}\binom{i+j}{i+j+k-f-h}w^h([t^h](1+t)^h e^{-St}) \end{aligned} \tag{A.25}$$

Each term in the summation over h is a product of coefficients of two generating functions,

$$\begin{aligned} M^{f}_{\nu_+,\nu_-,\nu_{\mathrm{D}}} &= \sum_{i=0}^{\nu_+} \binom{\nu_+}{i} \tilde{x}^i x^{\nu_+-i} \sum_{j=0}^{\nu_-} \binom{\nu_-}{j} \tilde{y}^j y^{\nu_--j} \sum_{k=0}^{\nu_{\mathrm{D}}} \binom{\nu_{\mathrm{D}}}{k} \tilde{z}^k z^{\nu_{\mathrm{D}}-k} w^{k-f} \\ &\quad \times \sum_{h=k-f}^{i+j+k-f} \binom{i+j}{i+j+k-f-h} w^{h+f-k} ([t^h](1+t)^h e^{-St}) \\ &= \sum_{i=0}^{\nu_+} \binom{\nu_+}{i} \tilde{x}^i x^{\nu_+-i} \sum_{j=0}^{\nu_-} \binom{\nu_-}{j} \tilde{y}^j y^{\nu_--j} \sum_{k=0}^{\nu_{\mathrm{D}}} \binom{\nu_{\mathrm{D}}}{k} \tilde{z}^k z^{\nu_{\mathrm{D}}-k} w^{k-f} \\ &\quad \times \sum_{h=k-f}^{i+j+k-f} ([t^{i+j+k-f-h}](w+t)^{i+j})([t^h](1+t)^h e^{-St}). \end{aligned} \tag{A.26}$$

For notational convenience, let us define

$$c_\alpha = [t^\alpha](w+t)^{i+j}, \qquad d_\beta = [t^\beta](1+t)^\beta e^{-St}. \tag{A.27}$$

Since c_α is zero when $\alpha > i+j$, the lower limit of the summation over h can be shifted from $h = k-f$ to $h = 0$,

$$\sum_{h=k-f}^{i+j+k-f} c_{i+j+k-f-h} d_h = \sum_{h=0}^{i+j+k-f} c_{i+j+k-f-h} d_h. \tag{A.28}$$

This summation over h can be written as the coefficient of the product of two generating function

$$\sum_{h=0}^{i+j+k-f} c_{i+j+k-f-h} d_h = [q^{i+j+k-f}] \left(\sum_{\alpha=0}^{\infty} c_\alpha q^\alpha \right) \left(\sum_{\beta=0}^{\infty} d_\beta q^\beta \right), \tag{A.29}$$

where q is the new dummy variable. Now we will find a closed expression for the generating function

$$C(q) = \sum_{\alpha=0}^{\infty} c_\alpha q^\alpha, \qquad D(q) = \sum_{\beta=0}^{\infty} d_\beta q^\beta. \tag{A.30}$$

Using binomial expansion, we get the closed expression $C(q) = (w+q)^{i+j}$. However, it is much more complicated to obtain a closed expression for $D(q)$. To do so, we use the powerful Lagrange-Bürmann formula, which states that for any generating series $f(t)$ and $g(t)$ such that

$f(0) \neq 0$ and a change of variable $q = t/f(t)$, we have an identity of generating functions in the dummy variable q,

$$\sum_{\beta=0}^{\infty}([t^{\beta}]f(t)^{\beta}g(t))q^{\beta} = \frac{g(t)}{f(t)}\frac{dt}{dq}, \tag{A.31}$$

where t is expressed in terms of q. In our scenario, $f(t) = (1+t)$ and $g(t) = e^{-St}$, hence $q = t/(1+t)$, which gives us

$$t = \frac{q}{1-q} \qquad \frac{dt}{dq} = \frac{1}{(1-q)^2} \tag{A.32}$$

Writing t in terms of q we get $f(t) = \frac{1}{1-q}$ and $g(t) = e^{-Sq/(1-q)}$. Therefore we have

$$\begin{aligned} D(q) &= \frac{e^{-Sq/(1-q)}}{(1-q)^2}(1-q) \\ &= \frac{e^{-Sq/(1-q)}}{(1-q)}. \end{aligned} \tag{A.33}$$

Continuing with the original summation, we now have

$$\begin{aligned} M^{f}_{\nu_+,\nu_-,\nu_{\mathrm{D}}} = &\sum_{i=0}^{\nu_+}\binom{\nu_+}{i}\tilde{x}^i x^{\nu_+-i}\sum_{j=0}^{\nu_-}\binom{\nu_-}{j}\tilde{y}^j y^{\nu_--j} \\ &\times\sum_{k=0}^{\nu_{\mathrm{D}}}\binom{\nu_{\mathrm{D}}}{k}\tilde{z}^k z^{\nu_{\mathrm{D}}-k} w^{k-f}\left([t^{i+j+k-f}](w+t)^{i+j}\frac{e^{-St/(1-t)}}{(1-t)}\right) \end{aligned} \tag{A.34}$$

Note that in the above expression we again replaced q with t. Repeating the calculations using Lagrange-Bürmann formula three more times, for the summation over i, j and k, we get the final compressed expression of the desired summation

$$M^{f}_{\nu_+,\nu_-,\nu_{\mathrm{D}}} = [q^{N_-}]\left((\tilde{x}+qx)^{\nu_+}(\tilde{y}+yq)^{\nu_-}\frac{(\tilde{z}-\tilde{z}q+zq)^{\nu_{\mathrm{D}}}}{(1-q)^f}\frac{\exp\left(\frac{-Swq}{1-q-wq}\right)}{(1-q-wq)}\right). \tag{A.35}$$

Applying operators $\hat{O}_f(S)$ and $\hat{T}_f(w)$ to $M^f_{\nu_+,\nu_-,\nu_\mathrm{D}}$

$$
\begin{aligned}
F^{f,0}_{\nu_+,\nu_-,\nu_\mathrm{D}} &= \sqrt{\frac{e^{-S}}{S^f}}\sqrt{\frac{N_-!}{\nu_+!\nu_-!\nu_\mathrm{D}!}}\tilde{w}^{-f}[q^{N_-}]\Bigg((\tilde{x}+qx)^{\nu_+}(\tilde{y}+yq)^{\nu_-}\frac{(\tilde{z}-\tilde{z}q+zq)^{\nu_\mathrm{D}}}{(1-q)^f} \\
&\quad\times \hat{O}_f(S)\hat{T}_f(w)\frac{\exp\left(\frac{-Swq}{1-q-wq}\right)}{(1-q-wq)}\Bigg) \\
&= \sqrt{e^{-S}S^f}\sqrt{\frac{N_-!}{\nu_+!\nu_-!\nu_\mathrm{D}!}}\tilde{w}^{-f}[q^{N_-}]\Bigg((\tilde{x}+qx)^{\nu_+}(\tilde{y}+yq)^{\nu_-}(\tilde{z}-\tilde{z}q+zq)^{\nu_\mathrm{D}} \\
&\quad\times \frac{\exp\left(\frac{-Swq}{1-q-wq}\right)}{(1-q-wq)^{f+1}}\Bigg)
\end{aligned}
\tag{A.36}
$$

A.3.1 Product not coupled

When $g_\mathrm{P} = 0$, the expression in equation (A.36) does not apply,

$$
\begin{aligned}
F^{f,0}_{\nu_+,\nu_-,\nu_\mathrm{D}} =& \sqrt{\frac{N_-!}{\nu_+!\nu_-!\nu_\mathrm{D}!}}\sum_{m=0}^{\nu_+}\sum_{n=0}^{\nu_-}\sum_{q=0}^{\nu_\mathrm{D}}\sum_{h=\nu_\mathrm{D}-f-q}^{N_--m-n-q}\binom{\nu_+}{m}\binom{\nu_-}{n}\binom{(\nu_+-\nu_-)-(m+n)}{h+q+f-\nu_\mathrm{D}}\binom{\nu_\mathrm{D}}{q} \\
&\times\left(\sin\theta\right)^{m+n}\left(\cos\theta'\right)^{m}\left(\sin\theta'\right)^{n}\left(-\cos\theta\right)^{N_--(m+n)}\left(\sin\theta'\right)^{\nu_+-m}\left(-\cos\theta'\right)^{\nu_--n}(-1)^q \\
&\times\left[\frac{g_\mathrm{P}}{\sqrt{g_\mathrm{R}^2(N_\mathrm{R}-1)+g_\mathrm{P}^2(N_\mathrm{P}+1)}}\right]^{(f+h+2q)-\nu_\mathrm{D}} \\
&\times\left[\sqrt{\frac{g_\mathrm{R}^2(N_\mathrm{R}-1)+g_\mathrm{P}^2N_\mathrm{P}}{g_\mathrm{R}^2(N_\mathrm{R}-1)+g_\mathrm{P}^2(N_\mathrm{P}+1)}}\right]^{\nu_\mathrm{D}+N_--h-m-n-2q}\left[\sqrt{\frac{g_\mathrm{R}^2(N_\mathrm{R}-1)+g_\mathrm{P}^2N_\mathrm{P}}{g_\mathrm{R}^2N_\mathrm{R}+g_\mathrm{P}^2N_\mathrm{P}}}\right]^{N_--h-m-n} \\
&\times\left[\frac{g_\mathrm{R}}{\sqrt{g_\mathrm{R}^2N_\mathrm{R}+g_\mathrm{P}^2N_\mathrm{P}}}\right]^{h}\sqrt{\frac{(h+f)!}{h!}}\left\langle h_{\mathrm{R},c}\middle|(h+f)_{\mathrm{P},c}\right\rangle .
\end{aligned}
\tag{A.37}
$$

Since $g_{\mathrm{P}} = 0$, only terms with $f + h + 2q - \nu_{\mathrm{D}} = 0$ will be non-zero,

$$\begin{aligned} F^{f,0}_{\nu_+,\nu_-,\nu_{\mathrm{D}}} =& \sqrt{\frac{N_-!}{\nu_+!\nu_-!\nu_{\mathrm{D}}!}} \sum_{m=0}^{\nu_+} \sum_{n=0}^{\nu_-} \sum_{q=0}^{\nu_{\mathrm{D}}} \binom{\nu_+}{m} \binom{\nu_-}{n} \binom{(\nu_+ + \nu_-) - (m+n)}{-q} \binom{\nu_{\mathrm{D}}}{q} \Big(\sin\theta\Big)^{m+n} \Big(\cos\theta'\Big)^{m} \\ & \times \Big(\sin\theta'\Big)^{n} \Big(-\cos\theta\Big)^{N_- - (m+n)} \times \Big(\sin\theta'\Big)^{\nu_+ - m} \Big(-\cos\theta'\Big)^{\nu_- - n} (-1)^q \left(\frac{1}{\sqrt{N_{\mathrm{R}}}}\right)^{\nu_{\mathrm{D}} - f - 2q} \\ & \times \left(\sqrt{\frac{N_{\mathrm{R}} - 1}{N_{\mathrm{R}}}}\right)^{N_- + f + 2q - \nu_{\mathrm{D}} - m - n} \sqrt{\frac{(\nu_{\mathrm{D}} - 2q)!}{(\nu_{\mathrm{D}} - 2q - f)!}} \left\langle (\nu_{\mathrm{D}} - 2q - f)_{\mathrm{R},c} \middle| (\nu_{\mathrm{D}} - 2q)_{\mathrm{P},c} \right\rangle . \end{aligned} \tag{A.38}$$

From the above, we see that $q = 0$ because of the binomial coefficient involving $-q$ and

$$\begin{aligned} F^{f,0}_{\nu_+,\nu_-,\nu_{\mathrm{D}}} =& \sqrt{\frac{N_-!}{\nu_+!\nu_-!\nu_{\mathrm{D}}!}} \sum_{m=0}^{\nu_+} \sum_{n=0}^{\nu_-} \binom{\nu_+}{m} \binom{\nu_-}{n} \Big(\sin\theta\Big)^{m+n} \Big(\cos\theta'\Big)^{m} \Big(\sin\theta'\Big)^{n} \Big(-\cos\theta\Big)^{N_- - (m+n)} \\ & \times \Big(\sin\theta'\Big)^{\nu_+ - m} \Big(-\cos\theta'\Big)^{\nu_- - n} \left(\frac{1}{\sqrt{N_{\mathrm{R}}}}\right)^{\nu_{\mathrm{D}} - f} \left(\sqrt{\frac{N_{\mathrm{R}} - 1}{N_{\mathrm{R}}}}\right)^{N_- + f - \nu_{\mathrm{D}} - m - n} \sqrt{\frac{\nu_{\mathrm{D}}!}{(\nu_{\mathrm{D}} - f)!}} \\ & \times \left\langle (\nu_{\mathrm{D}} - f)_{\mathrm{R},c} \middle| (\nu_{\mathrm{D}})_{\mathrm{P},c} \right\rangle . \end{aligned} \tag{A.39}$$

Using the binomial expansion to collect terms, we get

$$F^{f,0}_{\nu_+,\nu_-,\nu_{\mathrm{D}}} = \sqrt{\frac{N_-!}{\nu_+!\nu_-!(\nu_{\mathrm{D}} - f)!}} (x + \tilde{x})^{\nu_+} (y + \tilde{y})^{\nu_-} u^{\nu_{\mathrm{D}} - f} \left\langle (\nu_{\mathrm{D}} - f)_{\mathrm{R},c} \middle| (\nu_{\mathrm{D}})_{\mathrm{P},c} \right\rangle . \tag{A.40}$$

A.3.2 Reactant not coupled

Starting from equation (A.5) and substituting $g_{\mathrm{R}} = 0$, we have $w = 0$,

$$F^{f,0}_{\nu_+,\nu_-,\nu_{\mathrm{D}}} = \sqrt{e^{-S} S^f} \sqrt{\frac{N_-!}{\nu_+!\nu_-!\nu_{\mathrm{D}}!}} \tilde{w}^{-f} \Big[q^{N_-}\Big] \left((\tilde{x} + xq)^{\nu_+} (\tilde{y} + yq)^{\nu_-} (\tilde{z} - \tilde{z}q + zq)^{\nu_{\mathrm{D}}} \frac{1}{(1-q)^{f+1}} \right). \tag{A.41}$$

Changing variable from q to $t = q(1+w)$

$$\begin{aligned} F^{f,0}_{\nu_+,\nu_-,\nu_D} =& \sqrt{e^{-S}S^f}\sqrt{\frac{N_-!}{\nu_+!\nu_-!\nu_D!}}(\tilde{w}(1+w))^{-f}[t^{N_-}]\Bigg(\Big(\tilde{x}(1+w)+xt\Big)^{\nu_+}\Big(\tilde{y}(1+w)+yt\Big)^{\nu_-} \\ & \times\Big(\tilde{z}(1+w)+(z-\tilde{z})t\Big)^{\nu_D}\frac{1}{(1-t)^{f+1}}\Bigg) \\ =& \sqrt{e^{-S}S^f}\sqrt{\frac{N_-!}{\nu_+!\nu_-!\nu_D!}}(\tilde{w}(1+w))^{-f}B^f_{\nu_+,\nu_-,\nu_D}, \end{aligned} \tag{A.42}$$

and we call the part of $F^{f,0}_{\nu_+,\nu_-,\nu_D}$ that involves taking the t^{N_-} coefficient

$$B^f_{\nu_+,\nu_-,\nu_D} = [t^{N_-}]\left(\frac{G_{\nu_+,\nu_-,\nu_D}(t)}{(1-t)^{f+1}}\right), \tag{A.43}$$

where

$$G_{\nu_+,\nu_-,\nu_D}(t) = \Big(\tilde{x}(1+w)+xt\Big)^{\nu_+}\Big(\tilde{y}(1+w)+yt\Big)^{\nu_-}\Big(\tilde{z}(1+w)+(z-\tilde{z})t\Big)^{\nu_D}. \tag{A.44}$$

When $f < 0$, then $\deg(G_{\nu_+,\nu_-,\nu_D}(t)(1-t)^{-f-1}) = N_- - 1$, therefore, $B^f_{\nu_+,\nu_-,\nu_D} = 0$. When $f = 0$, then $\deg(G_{\nu_+,\nu_-,\nu_D}(t)) = N_-$ and we have the following identity

$$[t^{N_-}]\left(\frac{G_{\nu_+,\nu_-,\nu_D}(t)}{(1-t)}\right) = G_{\nu_+,\nu_-,\nu_D}(1). \tag{A.45}$$

Using this identity, we obtain the expression for $B^f_{\nu_+,\nu_-,\nu_D}$ base case $f = 0$,

$$B^0_{\nu_+,\nu_-,\nu_D} = G_{\nu_+,\nu_-,\nu_D}(1). \tag{A.46}$$

Now that we have the result for $f = 0$, let's derive a recursive formula for $B^f_{\nu_+,\nu_-,\nu_D}$ when $f \geq 1$. The coefficient of t^{N_-+1} in a series $\sum_n a_n t^n$ is related to the coefficient of t^{N_-} of the derivative of

the same series. Using this,

$$\begin{aligned}
\left[t^{N_-}\right]\frac{d}{dt}\left(\frac{G_{\nu_+,\nu_-,\nu_\mathrm{D}}(t)}{(1-t)^f}\right) &= (N_-+1)[t^{N_-+1}]\left(\frac{G_{\nu_+,\nu_-,\nu_\mathrm{D}}(t)}{(1-t)^f}\right)\\
[t^{N_-}]\left(\frac{G'_{\nu_+,\nu_-,\nu_\mathrm{D}}(t)}{(1-t)^f}\right)+f[t^{N_-}]\left(\frac{G_{\nu_+,\nu_-,\nu_\mathrm{D}}(t)}{(1-t)^{f+1}}\right) &= (N_-+1)[t^{N_-+1}]\left(\frac{G_{\nu_+,\nu_-,\nu_\mathrm{D}}(t)}{(1-t)^f}\right)\\
fB^f_{\nu_+,\nu_-,\nu_\mathrm{D}} &= (N_-+1)B^{f-1}_{\nu_+,\nu_-,\nu_\mathrm{D}}-[t^{N_-}]\left(\frac{G'_{\nu_+,\nu_-,\nu_\mathrm{D}}(t)}{(1-t)^f}\right)
\end{aligned} \tag{A.47}$$

$$B^f_{\nu_+,\nu_-,\nu_\mathrm{D}}=\frac{1}{f}\left((N_-+1)B^{f-1}_{\nu_+,\nu_-,\nu_\mathrm{D}}-\nu_+xB^{f-1}_{\nu_+-1,\nu_-,\nu_\mathrm{D}}-\nu_-yB^{f-1}_{\nu_+,\nu_--1,\nu_\mathrm{D}}-\nu_\mathrm{D}(z-\tilde{z})B^{f-1}_{\nu_+,\nu_-,\nu_\mathrm{D}-1}\right) \tag{A.48}$$

The expression for $B^f_{\nu_+,\nu_-,\nu_\mathrm{D}}$ for all the different cases,

$$B^f_{\nu_+,\nu_-,\nu_\mathrm{D}}=\begin{cases}0 & f<0\\ G_{\nu_+,\nu_-,\nu_\mathrm{D}}(1) & f=0\\ \frac{1}{f}\Big((N_-+1)B^{f-1}_{\nu_+,\nu_-,\nu_\mathrm{D}}-\nu_+xB^{f-1}_{\nu_+-1,\nu_-,\nu_\mathrm{D}}-\nu_-yB^{f-1}_{\nu_+,\nu_--1,\nu_\mathrm{D}} & \\ -\nu_\mathrm{D}(z-\tilde{z})B^{f-1}_{\nu_+,\nu_-,\nu_\mathrm{D}-1}\Big) & f>0\end{cases} \tag{A.49}$$

A.3.3 Product and reactant equally coupled

For the special case when $g_{\mathrm{R}} = g_{\mathrm{P}}$, we change variable $t = q(1+w)$ and the expression becomes

$$\begin{aligned} F^{f,0}_{\nu_+,\nu_-,\nu_{\mathrm{D}}} =& \sqrt{e^{-S}S^f}\sqrt{\frac{N_-!}{\nu_+!\nu_-!\nu_{\mathrm{D}}!}}(\tilde{w}(1+w))^{-f}[t^{N_-}]\Bigg(\Big(\tilde{x}(1+w)+xt\Big)^{\nu_+}\Big(\tilde{y}(1+w)+yt\Big)^{\nu_-} \\ & \times\Big(\tilde{z}(1+w)+(z-\tilde{z})t\Big)^{\nu_{\mathrm{D}}}\frac{\exp\Big(\frac{-Swt}{(1+w)(1-t)}\Big)}{(1-t)^{f+1}}\Bigg) \\ =& \sqrt{e^{-S}S^f}\sqrt{\frac{Q!}{\nu_+!\nu_-!\nu_{\mathrm{D}}!}}(\tilde{w}(1+w))^{-f}A^f_{\nu_+,\nu_-,\nu_{\mathrm{D}}}, \end{aligned} \tag{A.50}$$

where

$$\begin{aligned} A^f_{\nu_+,\nu_-,\nu_{\mathrm{D}}} =& [t^{N_-}]\Bigg(\Big(\tilde{x}(1+w)+xt\Big)^{\nu_+}\Big(\tilde{y}(1+w)+yt\Big)^{\nu_-}\Big(\tilde{z}(1+w)+(z-\tilde{z})t\Big)^{\nu_{\mathrm{D}}} \\ & \times\frac{\exp\Big(\frac{-Swt}{(1+w)(1-t)}\Big)}{(1-t)^{f+1}}\Bigg). \end{aligned} \tag{A.51}$$

Expanding the exponential,

$$
\begin{aligned}
A^{f}_{\nu_+,\nu_-,\nu_D} =& [t^Q]\Bigg(\Big(\tilde{x}(1+w)+xt\Big)^{\nu_+}\Big(\tilde{y}(1+w)+yt\Big)^{\nu_-}\Big(\tilde{z}(1+w)+(z-\tilde{z})t\Big)^{\nu_D}\frac{1}{(1-t)^{f+1}} \\
&\times \exp\Big(\frac{-Swt}{(1+w)(1-t)}\Big)\Bigg) \\
=& \sum_{n=0}^{\infty}\frac{1}{n!}[t^Q]\Bigg(\Big(\tilde{x}(1+w)+xt\Big)^{\nu_+}\Big(\tilde{y}(1+w)+yt\Big)^{\nu_-}\Big(\tilde{z}(1+w)+(z-\tilde{z})t\Big)^{\nu_D}\frac{1}{(1-t)^{f+1}} \\
&\times \Big(\frac{-Swt}{(1+w)(1-t)}\Big)^{n}\Bigg) \\
=& \sum_{n=0}^{\infty} w^n\frac{1}{n!}\Big(\frac{-S}{1+w}\Big)^{n}[t^Q]\Bigg(\Big(\tilde{x}(1+w)+xt\Big)^{\nu_+}\Big(\tilde{y}(1+w)+yt\Big)^{\nu_-}\Big(\tilde{z}(1+w)+(z-\tilde{z})t\Big)^{\nu_D} \\
&\times \frac{t^n}{(1-t)^{f+1+n}}\Bigg) \\
=& \sum_{n=0}^{\infty} w^n\frac{1}{n!}\Big(\frac{-S}{1+w}\Big)^{n}[t^{Q-n}]\Bigg(\Big(\tilde{x}(1+w)+xt\Big)^{\nu_+}\Big(\tilde{y}(1+w)+yt\Big)^{\nu_-} \\
&\times \Big(\tilde{z}(1+w)+(z-\tilde{z})t\Big)^{\nu_D}\frac{1}{(1-t)^{f+1+n}}\Bigg) \\
=& \sum_{n=0}^{\infty} w^n\frac{1}{n!}\Big(\frac{-S}{1+w}\Big)^{n}B^{f+n}_{\nu_+,\nu_-,\nu_D}
\end{aligned}
\tag{A.52}
$$

For the case when $g_R = g_P$, $w = 1/(N-1)$ is very small when a large number of molecules are coupled to the cavity. Therefore, the summation in $A^{f}_{\nu_+,\nu_-,\nu_D}$ converges quickly and is easy to calculate on a computer.

Appendix B

Supplementary Information: Molecular and solid-state topological polaritons induced by population imbalance

B.1 Light-matter coupling

The light-matter coupling part of the total Hamiltonian under the electric dipole approximation is,

$$\begin{aligned}\hat{H}_{\text{cav-mol}} &= \sum_{\mathbf{m}} \sum_{\mathbf{k},\alpha} -\hat{\boldsymbol{\mu}}_{\mathbf{m}} \cdot \hat{\mathbf{E}}_{\mathbf{k},\alpha}(\mathbf{r}_{\mathbf{m}}, 0), \\ &= \sum_{\mathbf{m}} \sum_{\mathbf{k},\alpha} -\Big[\sum_{\alpha'=\pm} (\boldsymbol{\mu}_{\alpha'} \hat{\sigma}^{\dagger}_{\mathbf{m},\alpha'} + \boldsymbol{\mu}^{*}_{\alpha'} \hat{\sigma}_{\mathbf{m},\alpha'}) \Big] \cdot \hat{\mathbf{E}}_{\mathbf{k},\alpha}(\mathbf{r}_{\mathbf{m}}, 0),\end{aligned} \tag{B.1}$$

where $\boldsymbol{\mu}_{\alpha'} = \boldsymbol{\mu}_{\mathbf{m},\alpha'} = \left\langle \mathbf{m}, \alpha'_{\text{mol}} \right| \hat{\boldsymbol{\mu}} \left| \mathbf{m}, \text{G} \right\rangle$ is independent of $\mathbf{m}$ since we assume that all porphyrin molecules lie flat in the x-y plane and are oriented. The electric field operator of the mode labeled by $\mathbf{k}$ and α is

$$\hat{\mathbf{E}}_{\mathbf{k},\alpha}(\mathbf{r}, z) = \sqrt{\frac{\hbar\omega_{\mathbf{k},\alpha}}{2V\varepsilon\epsilon_0}} \Big(\mathbf{f}^{*}_{\mathbf{k},\alpha}(\mathbf{r}, z) \hat{a}^{\dagger}_{\mathbf{k},\alpha} + \mathbf{f}_{\mathbf{k},\alpha}(\mathbf{r}, z) \hat{a}_{\mathbf{k},\alpha} \Big). \tag{B.2}$$

Here, $V = L_x L_y L_z$ is the volume of the box we consider, where as mentioned in the main manuscript, we apply periodic boundary conditions along the x and y directions. From here on, we will call the in-plane area of the box $A = L_x L_y$. Here, $\mathbf{f}_{\mathbf{k},\alpha}(\mathbf{r}, z)$ is the mode profile and it satisfies [149]

$$\int d\mathbf{r} \int_0^{L_z} dz \mathbf{f}^{*}_{\mathbf{k},\alpha}(\mathbf{r}, z) \mathbf{f}_{\mathbf{k},\alpha}(\mathbf{r}, z) = L_z A. \tag{B.3}$$

For the TE and TM modes [150],

$$\begin{aligned}
\mathbf{f}_{\mathbf{k},\mathrm{TE}}(\mathbf{r},z) =& e^{i\mathbf{k}\cdot\mathbf{r}}\sqrt{2}\sin\left[\frac{n_z\pi}{L_z}\left(z+\frac{L_z}{2}\right)\right]\hat{\phi},\\
\mathbf{f}_{\mathbf{k},\mathrm{TM}}(\mathbf{r},z) =& e^{i\mathbf{k}\cdot\mathbf{r}}\sqrt{\frac{2}{|\mathbf{k}|^2+\left(\frac{n_z\pi}{L_z}\right)^2}}\left\{\left(\frac{n_z\pi}{L_z}\right)\sin\left[\frac{n_z\pi}{L_z}\left(z+\frac{L_z}{2}\right)\right]\hat{\boldsymbol{\rho}}-i|\mathbf{k}|\cos\left[\frac{n_z\pi}{L_z}\left(z+\frac{L_z}{2}\right)\right]\hat{\mathbf{z}}\right\}.
\end{aligned} \tag{B.4}$$

We make the rotating-wave approximation,

$$\begin{aligned}
\hat{H}_{\mathrm{cav-mol}} =& \sum_{\mathbf{m}}\sum_{\mathbf{k},\alpha}-\Big[\sum_{\alpha'=\pm}(\boldsymbol{\mu}_{\alpha'}\hat{\sigma}^{\dagger}_{\mathbf{m},\alpha'}+\boldsymbol{\mu}^{*}_{\alpha'}\hat{\sigma}_{\mathbf{m},\alpha'})\Big]\\
&\cdot\left[\sqrt{\frac{\hbar\omega_{\mathbf{k},\alpha}}{2V\varepsilon\epsilon_0}}\left(\mathbf{f}^{*}_{\mathbf{k},\alpha}(\mathbf{r}_{\mathbf{m}},0)\hat{a}^{\dagger}_{\mathbf{k},\alpha}+\mathbf{f}_{\mathbf{k},\alpha}(\mathbf{r}_{\mathbf{m}},0)\hat{a}_{\mathbf{k},\alpha}\right)\right],\\
\approx& \sum_{\mathbf{m},\alpha'}\sum_{\mathbf{k},\alpha}-\sqrt{\frac{\hbar\omega_{\mathbf{k},\alpha}}{2V\varepsilon\epsilon_0}}\Big[\boldsymbol{\mu}_{\alpha'}\cdot\mathbf{f}_{\mathbf{k},\alpha}(\mathbf{r}_{\mathbf{m}},0)\hat{\sigma}^{\dagger}_{\mathbf{m},\alpha'}\hat{a}_{\mathbf{k},\alpha}+\boldsymbol{\mu}^{*}_{\alpha'}\cdot\mathbf{f}^{*}_{\mathbf{k},\alpha}(\mathbf{r}_{\mathbf{m}},0)\hat{\sigma}_{\mathbf{m},\alpha'}\hat{a}^{\dagger}_{\mathbf{k},\alpha}\Big],\\
=& \sum_{\mathbf{m},\alpha'}\sum_{\mathbf{k},\alpha}\Big[\frac{e^{i\mathbf{k}\cdot\mathbf{r}_{\mathbf{m}}}}{\sqrt{N_xN_y}}(\boldsymbol{\mu}_{\alpha'}\cdot\mathbf{J}_{\mathbf{k},\alpha})\hat{\sigma}^{\dagger}_{\mathbf{m},\alpha'}\hat{a}_{\mathbf{k},\alpha}+\frac{e^{-i\mathbf{k}\cdot\mathbf{r}_{\mathbf{m}}}}{\sqrt{N_xN_y}}(\boldsymbol{\mu}^{*}_{\alpha'}\cdot\mathbf{J}^{*}_{\mathbf{k},\alpha})\hat{\sigma}_{\mathbf{m},\alpha'}\hat{a}^{\dagger}_{\mathbf{k},\alpha}\Big],
\end{aligned} \tag{B.5}$$

where $\mathbf{J}_{\mathbf{k},\alpha}=-\sqrt{N_xN_y}\sqrt{\frac{\hbar\omega_{\mathbf{k},\alpha}}{2V\varepsilon\epsilon_0}}e^{-i\mathbf{k}\cdot\mathbf{r}}\mathbf{f}_{\mathbf{k},\alpha}(\mathbf{r},0)$ and $\boldsymbol{\mu}_{\alpha'}\cdot\mathbf{J}_{\mathbf{k},\alpha}$ is the collective light-matter coupling strength.

The annihilation operators of photon modes polarized along the horizontal (H) or x-axis and vertical (V) or y-axis are $\hat{a}_{\mathbf{k},\mathrm{H}}$ and $\hat{a}_{\mathbf{k},\mathrm{V}}$, respectively. They are related to $\alpha=\pm$ polarized modes through $\hat{a}_{\mathbf{k},\pm}=\frac{1}{\sqrt{2}}(\hat{a}_{\mathbf{k},\mathrm{H}}\mp i\hat{a}_{\mathbf{k},\mathrm{V}})$ [151]. In addition, we assume that they are related to the TM and TE modes through $\hat{a}_{\mathbf{k},\mathrm{TM}}=\cos\phi\hat{a}_{\mathbf{k},\mathrm{H}}+\sin\phi\hat{a}_{\mathbf{k},\mathrm{V}}$ and $\hat{a}_{\mathbf{k},\mathrm{TE}}=-\sin\phi\hat{a}_{\mathbf{k},\mathrm{H}}+\cos\phi\hat{a}_{\mathbf{k},\mathrm{V}}$. Using this, we obtain the relationship between $\hat{a}_{\mathbf{k},\mathrm{TE}}$, $\hat{a}_{\mathbf{k},\mathrm{TM}}$ and $\hat{a}_{\mathbf{k},+}$, $\hat{a}_{\mathbf{k},-}$ modes to be,

$$\begin{aligned}
\hat{a}_{\mathbf{k},\mathrm{TM}} =& \frac{1}{\sqrt{2}}\left(e^{i\phi}\hat{a}_{\mathbf{k},+}+e^{-i\phi}\hat{a}_{\mathbf{k},-}\right),\\
\hat{a}_{\mathbf{k},\mathrm{TE}} =& \frac{1}{\sqrt{2}}\left(ie^{i\phi}\hat{a}_{\mathbf{k},+}-ie^{-i\phi}\hat{a}_{\mathbf{k},-}\right).
\end{aligned} \tag{B.6}$$

It is important to note that, based on these relationships and B.4, the α =H/V modes are not

completely linearly polarized and the $\alpha = \pm$ modes are not completely circularly polarized when $|\mathbf{k}|$ becomes comparable with $n_z\pi/L_z$. We also find,

$$\begin{aligned}\mathbf{J}_{\mathbf{k},+} =& \frac{e^{i\phi}}{\sqrt{2}}\Big(\mathbf{J}_{\mathbf{k},\mathrm{TM}} + i\mathbf{J}_{\mathbf{k},\mathrm{TE}}\Big),\\ \mathbf{J}_{\mathbf{k},-} =& \frac{e^{-i\phi}}{\sqrt{2}}\Big(\mathbf{J}_{\mathbf{k},\mathrm{TM}} - i\mathbf{J}_{\mathbf{k},\mathrm{TE}}\Big).\end{aligned} \tag{B.7}$$

To keep the collective coupling strength $\boldsymbol{\mu}_{\alpha'} \cdot \mathbf{J}_{\mathbf{k},\alpha}$ constant while taking the $a \to 0$ limit, we take the magnitude of the collective transition dipole of the bright state $\sqrt{N_x N_y}\mu_0$ over square root of the quantization area of the photon mode $\sqrt{A}$ to be a constant; that is, we keep $\sqrt{\rho_A}\mu_0 = \mu_0/a$ a constant, where $\rho_A = N_x N_y/A$ is the areal density of quantum emitters.

$$\begin{aligned}\mathbf{J}_{\mathbf{k},\alpha} =& -\sqrt{\rho_A}\sqrt{\frac{\hbar\omega_{\mathbf{k},\alpha}}{2L_z\varepsilon\epsilon_0}}e^{-i\mathbf{k}.\mathbf{r}}\mathbf{f}_{\mathbf{k},\alpha}(\mathbf{r},0)\\ =& -\frac{1}{a}\sqrt{\frac{\hbar\omega_{\mathbf{k},\alpha}}{2L_z\varepsilon\epsilon_0}}e^{-i\mathbf{k}.\mathbf{r}}\mathbf{f}_{\mathbf{k},\alpha}(\mathbf{r},0).\end{aligned} \tag{B.8}$$

B.2 Chern number calculation

For the Chern invariant to be an integer, it is important that the Berry curvature is integrated over a closed and bounded surface [152]. For periodic systems with a finite period, the Brillouin zone is a torus which satisfies this requirement. However, for a continuous system, (k_x, k_y) lies on an unbounded plane; for such systems, Silveirinha [96] proposed mapping this infinitely large plane onto a sphere to compute the Chern number. This is the procedure we follow in our work. We discretize k-space and compute the Berry flux in each plaquette within a square-shaped region in k-space, $-k_{\max} \le k_x, k_y \le k_{\max}$ [152, 153] (Fig. S1a and S1b). The entire region that satisfies the condition $k_x, k_y > k_{\max}$ or $k_x, k_y < -k_{\max}$ is taken as a single giant plaquette (Fig. S1b), and the Berry flux within this region is computed by taking the Berry phase along the boundary of the plaquette but in a direction opposite to that used to compute Berry flux

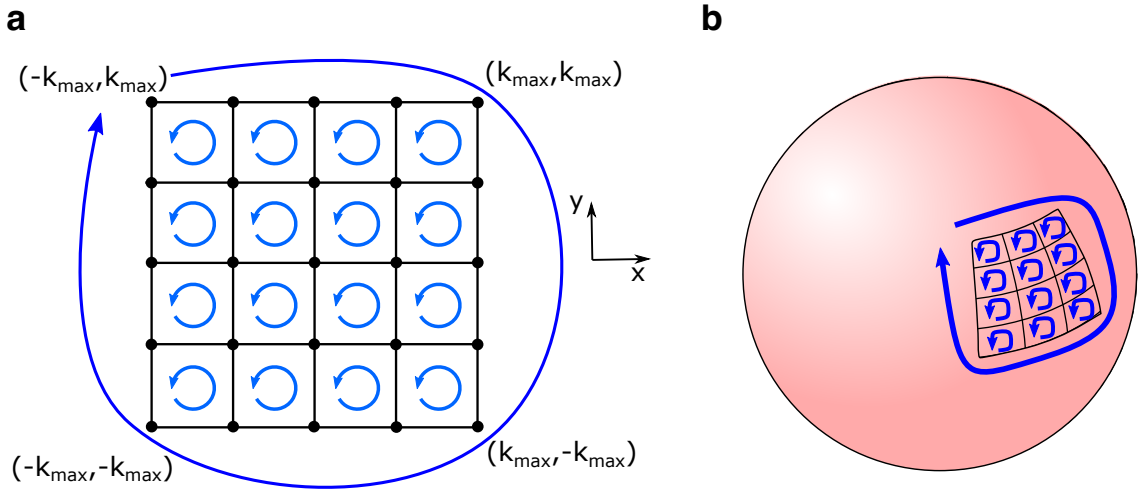

Figure B.1. (a) This is a cartoon figure that demonstrates the way Berry flux and Chern number are computed in our system. The small squares are the plaquettes over which Berry flux is computed. The blue arrows specify the orientation used for Berry flux computation. Note that the direction is opposite for the small squares and the large square. (b) Same as (a), but placed on a sphere. Here, it is more clear that the direction of the arrow for the large square indicates the way Berry flux is computed for the giant plaquette covering the rest of the sphere.

for plaquettes within the square $-k_{\max} \leq k_x, k_y \leq k_{\max}$ as indicated in Fig. S1a and S1b. To ensure that we obtain a converged Chern number, we calculate the Chern number for different $k_{\max}$ and find that, for our system, once $k_{\max} \gtrsim 100\mu\text{m}^{-1}$, the Chern number converges to $C_1 = \pm 1, C_2 = \mp 1, C_3 = 0$, and $C_4 = 0$ when $f_+ \neq f_-$ with $|f_+ - f_-| \gtrsim 0.11$. Smaller differences between f_+ and f_-, $|f_+ - f_-| \lesssim 0.11$ require larger $k_{\max}$ for convergence. This is not a problem for the $f_+ = f_-$ case because the Chern invariant will always be zero due to time-reversal symmetry $\Omega_l(\mathbf{k}) = -\Omega_l(-\mathbf{k})$, and we can use $k_{\max} \approx 100\mu\text{m}^{-1}$ to compute it.

B.3 Optical pumping

The number of excitations in the system $N_{\text{ex}} = \sum_{\mathbf{k},\alpha} a^\dagger_{\mathbf{k},\alpha} a_{\mathbf{k},\alpha} + \sum_{\mathbf{n},\alpha} \sigma^\dagger_{\mathbf{n},\alpha} \sigma_{\mathbf{n},\alpha}$ is a conserved quantity of this Hamiltonian. Therefore, when we have f_+ fraction of molecules in the $|+_{\text{mol}}\rangle$ state and f_- in the $|-_{\text{mol}}\rangle$ state, we will only have to look at the $(f_+ + f_-)N^{\text{th}}$ excitation manifold. Unfortunately, the dimensions of the Hilbert space of this manifold scale as $\binom{N}{(f_+ + f_-)N}$, and this

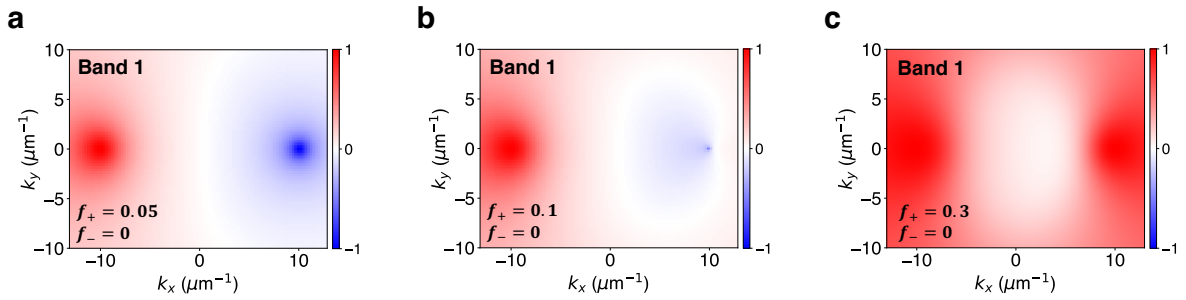

Figure B.2. The Stokes parameter, $S_3(\mathbf{k})$, of the lowest energy band (Band 1) under pumping with σ_+ polarized light which creates populations (a) $f_+ = 0.05$, $f_- = 0$, (b) $f_+ = 0.1$, $f_- = 0$, and (c) $f_+ = 0.3$, $f_- = 0$.

quickly becomes computationally intractable as the system size, N, increases. Using mean-field theory, we reduce this many-body problem to a one-body problem. That is, we derive an effective Hamiltonian for a single excitation in the mean-field of the remaining $(f_+ + f_-)N$ excitations; in this way, we reduce the dimensions of the Hilbert space to that of the first excitation manifold. To do this, we follow a procedure similar to that used by Ribeiro *et al.* [101] and write the Heisenberg equations of motion (EOM) for the operators $\hat{\sigma}_{\mathbf{m},\pm}$ and $\hat{a}_{\mathbf{k},\pm}$,

$$
\begin{aligned}
i\hbar\frac{d\hat{\sigma}_{\mathbf{n},\pm}}{dt} =& \left[\hat{\sigma}_{\mathbf{n},\pm}, \hat{H}_{\text{mol}}\right] + \left[\hat{\sigma}_{\mathbf{n},\pm}, \hat{H}_{\text{cav}}\right] + \left[\hat{\sigma}_{\mathbf{n},\pm}, \hat{H}_{\text{cav-mol}}\right] \\
=& \hbar\omega_e\hat{\sigma}_{\mathbf{n},\pm} + \frac{1}{\sqrt{N_x N_y}}\sum_{\mathbf{k}} e^{i\mathbf{k}\cdot\mathbf{r}_\mathbf{n}}\Big[(1 - \hat{\sigma}^\dagger_{\mathbf{n},\mp}\hat{\sigma}_{\mathbf{n},\mp} - 2\hat{\sigma}^\dagger_{\mathbf{n},\pm}\hat{\sigma}_{\mathbf{n},\pm})\Big(\mathbf{J}_{\mathbf{k},+}\cdot\boldsymbol{\mu}_\pm\hat{a}_{\mathbf{k},+} \\
&+ \mathbf{J}_{\mathbf{k},-}\cdot\boldsymbol{\mu}_\pm\hat{a}_{\mathbf{k},-}\Big) - \hat{\sigma}^\dagger_{\mathbf{n},\mp}\hat{\sigma}_{\mathbf{n},\pm}\Big(\mathbf{J}_{\mathbf{k},+}\cdot\boldsymbol{\mu}_\mp\hat{a}_{\mathbf{k},+} + \mathbf{J}_{\mathbf{k},-}\cdot\boldsymbol{\mu}_\mp\hat{a}_{\mathbf{k},-}\Big)\Big], \\
i\hbar\frac{d\hat{a}_{\mathbf{k},\pm}}{dt} =& \left[\hat{a}_{\mathbf{k},\pm}, \hat{H}_{\text{mol}}\right] + \left[\hat{a}_{\mathbf{k},\pm}, \hat{H}_{\text{cav}}\right] + \left[\hat{a}_{\mathbf{k},\pm}, \hat{H}_{\text{cav-mol}}\right] \\
=& \Big(E_0 + \frac{\hbar^2|\mathbf{k}|^2}{2m^*} \pm \zeta|\mathbf{k}|\cos\phi\Big)\hat{a}_{\mathbf{k},\pm} + \Big(-\beta_0 + \beta|\mathbf{k}|^2 e^{\mp i2\phi}\Big)\hat{a}_{\mp,\mathbf{k}} \\
&+ \frac{1}{\sqrt{N_x N_y}}\sum_{\mathbf{m}} e^{i\mathbf{k}\cdot\mathbf{r}_\mathbf{m}}\Big(\mathbf{J}^*_{\mathbf{k},\pm}\cdot\boldsymbol{\mu}^*_+\hat{\sigma}_{\mathbf{m},+} + \mathbf{J}^*_{\mathbf{k},\pm}\cdot\boldsymbol{\mu}^*_-\hat{\sigma}_{\mathbf{m},-}\Big).
\end{aligned}
\tag{B.9}
$$

We make a mean-field approximation to linearize these EOM. For instance, we use

$mn \approx \bar{m}n$, that is,

$$\begin{aligned}\hat{\sigma}^{\dagger}_{\mathbf{n},+}\hat{\sigma}_{\mathbf{n},+}\hat{a}_{\mathbf{k},+} =&\Big(\langle\hat{\sigma}^{\dagger}_{\mathbf{n},+}\hat{\sigma}_{\mathbf{n},+}\rangle + \hat{\sigma}^{\dagger}_{\mathbf{n},+}\hat{\sigma}_{\mathbf{n},+} - \langle\hat{\sigma}^{\dagger}_{\mathbf{n},+}\hat{\sigma}_{\mathbf{n},+}\rangle\Big)\hat{a}_{\mathbf{k},+}\\ =&\langle\hat{\sigma}^{\dagger}_{\mathbf{n},+}\hat{\sigma}_{\mathbf{n},+}\rangle\hat{a}_{\mathbf{k},+} + (\hat{\sigma}^{\dagger}_{\mathbf{n},+}\hat{\sigma}_{\mathbf{n},+} - \langle\hat{\sigma}^{\dagger}_{\mathbf{n},+}\hat{\sigma}_{\mathbf{n},+}\rangle)\langle\hat{a}_{\mathbf{k},+}\rangle\\ \approx&\langle\hat{\sigma}^{\dagger}_{\mathbf{n},+}\hat{\sigma}_{\mathbf{n},+}\rangle\hat{a}_{\mathbf{k},+},\end{aligned} \tag{B.10}$$

where $\langle\hat{O}\rangle = \mathrm{Tr}\big[\hat{\rho}_0\hat{O}\big]$ with $\hat{\rho}_0 \approx \prod_{\mathbf{m}}\hat{\rho}_{\mathbf{m}}\prod_{\mathbf{k}}\prod_{\alpha=+,-}\hat{\rho}_{\alpha,\mathbf{k}}$ [154]. Here, we assume that after dephasing of the molecular amplitudes, $\hat{\rho}_{\mathbf{m}} = f_{\mathrm{G}}\,|\mathbf{m}, G\rangle\langle\mathbf{m}, G| + f_{+}\,|\mathbf{m}, +_{\mathrm{mol}}\rangle\langle\mathbf{m}, +_{\mathrm{mol}}| + f_{-}\,|\mathbf{m}, -_{\mathrm{mol}}\rangle\langle\mathbf{m}, -_{\mathrm{mol}}|$, $\hat{\rho}_{\alpha,\mathbf{k}} = |\mathbf{k}, \alpha_{\mathrm{cav}}, 0\rangle\langle\mathbf{k}, \alpha_{\mathrm{cav}}, 0|$, and, therefore, $\langle\hat{a}_{\mathbf{k},+}\rangle = 0$. The EOM then become

$$\begin{aligned}i\hbar\frac{d\hat{\sigma}_{\mathbf{n},\pm}}{dt} \approx&\hbar\omega_{\mathrm{e}}\hat{\sigma}_{\mathbf{n},\pm} + \frac{1}{\sqrt{N_xN_y}}(1 - f_{\mp} - 2f_{\pm})\sum_{\mathbf{k}}e^{i\mathbf{k}\cdot\mathbf{r}_{\mathbf{n}}}\Big(\mathbf{J}_{\mathbf{k},+}\cdot\boldsymbol{\mu}_{\pm}\hat{a}_{\mathbf{k},+}\\ &+ \mathbf{J}_{\mathbf{k},-}\cdot\boldsymbol{\mu}_{\pm}\hat{a}_{\mathbf{k},-}\Big),\\ i\hbar\frac{d\hat{a}_{\mathbf{k},\pm}}{dt} =&\Big(E_0 + \frac{\hbar^2|\mathbf{k}|^2}{2m^*} \pm \zeta|\mathbf{k}|\cos\phi\Big)\hat{a}_{\mathbf{k},\pm} + \Big(-\beta_0 + \beta|\mathbf{k}|^2e^{\mp i2\phi}\Big)\hat{a}_{\mp,\mathbf{k}}\\ &+ \frac{1}{\sqrt{N_xN_y}}\sum_{\mathbf{m}}e^{i\mathbf{k}\cdot\mathbf{r}_{\mathbf{m}}}\Big(\mathbf{J}^{*}_{\mathbf{k},\pm}\cdot\boldsymbol{\mu}^{*}_{+}\hat{\sigma}_{\mathbf{m},+} + \mathbf{J}^{*}_{\mathbf{k},\pm}\cdot\boldsymbol{\mu}^{*}_{-}\hat{\sigma}_{\mathbf{m},-}\Big).\end{aligned} \tag{B.11}$$

We define rescaled operators $\hat{\sigma}'_{\mathbf{n},\pm} = \hat{\sigma}_{\mathbf{n},\pm}/\sqrt{1 - f_{\mp} - 2f_{\pm}}$ and rewrite the EOM,

$$\begin{aligned}i\hbar\frac{d\hat{\sigma}'_{\mathbf{n},\pm}}{dt} \approx&\hbar\omega_{\mathrm{e}}\hat{\sigma}'_{\mathbf{n},\pm} + \frac{1}{\sqrt{N_xN_y}}\sqrt{1 - f_{\mp} - 2f_{\pm}}\sum_{\mathbf{k}}e^{i\mathbf{k}\cdot\mathbf{r}_{\mathbf{n}}}\Big(\mathbf{J}_{\mathbf{k},+}\cdot\boldsymbol{\mu}_{\pm}\hat{a}_{\mathbf{k},+}\\ &+ \mathbf{J}_{\mathbf{k},-}\cdot\boldsymbol{\mu}_{\pm}\hat{a}_{\mathbf{k},-}\Big),\\ i\hbar\frac{d\hat{a}_{\mathbf{k},\pm}}{dt} =&\Big(E_0 + \frac{\hbar^2|\mathbf{k}|^2}{2m^*} \pm \zeta|\mathbf{k}|\cos\phi\Big)\hat{a}_{\mathbf{k},\pm} + \Big(-\beta_0 + \beta|\mathbf{k}|^2e^{\mp i2\phi}\Big)\hat{a}_{\mp,\mathbf{k}}\\ &+ \frac{}{\sqrt{N_xN_y}}\sum_{\mathbf{m}}e^{i\mathbf{k}\cdot\mathbf{r}_{\mathbf{m}}}\Big(\sqrt{1 - f_{-} - 2f_{+}}\mathbf{J}^{*}_{\mathbf{k},\pm}\cdot\boldsymbol{\mu}^{*}_{+}\hat{\sigma}'_{\mathbf{m},+} + \sqrt{1 - f_{+} - 2f_{-}}\mathbf{J}^{*}_{\mathbf{k},\pm}\cdot\boldsymbol{\mu}^{*}_{-}\hat{\sigma}'_{\mathbf{m},-}\Big).\end{aligned} \tag{B.12}$$

From these EOM, along with the fact that $\hat{\sigma}'_{\mathbf{n},\pm}$ act effectively as bosonic operators in mean-field, $\Big[\hat{\sigma}'_{\mathbf{n},+}, \hat{\sigma}'^{\dagger}_{\mathbf{n},+}\Big] = \frac{1-\hat{\sigma}^{\dagger}_{\mathbf{n},-}\hat{\sigma}_{\mathbf{n},-}-2\hat{\sigma}^{\dagger}_{\mathbf{n},+}\hat{\sigma}_{\mathbf{n},+}}{1-f_{-}-2f_{+}} \approx \hat{I}$ and $\Big[\hat{\sigma}'_{\mathbf{n},+}, \hat{\sigma}'^{\dagger}_{\mathbf{n},-}\Big] = \frac{-\hat{\sigma}^{\dagger}_{\mathbf{n},-}\hat{\sigma}_{\mathbf{n},+}}{1-f_{-}-2f_{+}} \approx \hat{0}$, where $\hat{I}$ and $\hat{0}$ are the identity and zero operators, we can construct an effective Hamiltonian $\hat{H}^{\mathrm{eff}} = \hat{H}^{\mathrm{eff}}_{\mathrm{mol}} + \hat{H}^{\mathrm{eff}}_{\mathrm{cav}} + \hat{H}^{\mathrm{eff}}_{\mathrm{cav-mol}}$

in $\hat{\sigma}'_{\mathbf{n},\pm}$ and $\hat{a}_{\mathbf{k},\pm}$,

$$
\begin{aligned}
\hat{H}^{\text{eff}}_{\text{mol}} &= \sum_{\mathbf{n}} \Big(\hbar\omega_{\text{e}} \hat{\sigma}'^{\dagger}_{\mathbf{n},+} \hat{\sigma}'_{\mathbf{n},+} + \hbar\omega_{\text{e}} \hat{\sigma}'^{\dagger}_{\mathbf{n},-} \hat{\sigma}'_{\mathbf{n},-} \Big), \\
\hat{H}^{\text{eff}}_{\text{cav}} &= \sum_{\mathbf{k}} \Big(E_0 + \frac{\hbar^2 |\mathbf{k}|^2}{2m^*} + \zeta |\mathbf{k}| \cos\phi \Big) \hat{a}^{\dagger}_{\mathbf{k},+} \hat{a}_{\mathbf{k},+} \\
&\quad + \Big(E_0 + \frac{\hbar^2 |\mathbf{k}|^2}{2m^*} - \zeta |\mathbf{k}| \cos\phi \Big) \hat{a}^{\dagger}_{\mathbf{k},-} \hat{a}_{\mathbf{k},-} + \Big(-\beta_0 + \beta |\mathbf{k}|^2 e^{-i2\phi} \Big) \hat{a}^{\dagger}_{\mathbf{k},+} \hat{a}_{\mathbf{k},-} \\
&\quad + \Big(-\beta_0 + \beta |\mathbf{k}|^2 e^{i2\phi} \Big) \hat{a}^{\dagger}_{\mathbf{k},-} \hat{a}_{\mathbf{k},+}, \\
\hat{H}^{\text{eff}}_{\text{cav-mol}} &= \frac{1}{\sqrt{N_x N_y}} \sum_{\mathbf{m}} \sum_{\mathbf{k}} e^{i\mathbf{k}\cdot\mathbf{r}_{\mathbf{m}}} \Bigg[\sqrt{1 - f_- - 2f_+} \Big(\mathbf{J}_{\mathbf{k},+} \cdot \boldsymbol{\mu}_+ \hat{\sigma}'^{\dagger}_{\mathbf{m},+} \hat{a}_{\mathbf{k},+} \\
&\quad + \mathbf{J}_{\mathbf{k},-} \cdot \boldsymbol{\mu}_+ \hat{\sigma}'^{\dagger}_{\mathbf{m},+} \hat{a}_{\mathbf{k},-} \Big) + \sqrt{1 - f_+ - 2f_-} \Big(\mathbf{J}_{\mathbf{k},+} \cdot \boldsymbol{\mu}_- \hat{\sigma}'^{\dagger}_{\mathbf{m},-} \hat{a}_{\mathbf{k},+} \\
&\quad + \mathbf{J}_{\mathbf{k},-} \cdot \boldsymbol{\mu}_- \hat{\sigma}'^{\dagger}_{\mathbf{m},-} \hat{a}_{\mathbf{k},-} \Big) \Bigg] + \text{H.c.},
\end{aligned}
\tag{B.13}
$$

which is the mean-field Hamiltonian when the system has f_+, f_- excitations. Writing this effective Hamiltonian in k-space,

$$
\begin{aligned}
\hat{H}^{\text{eff}}_{\text{mol}} &= \sum_{\mathbf{k}} \Big[\hbar\omega_{\text{e}} \hat{\sigma}'^{\dagger}_{\mathbf{k},+} \hat{\sigma}'_{\mathbf{k},+} + \hbar\omega_{\text{e}} \hat{\sigma}'^{\dagger}_{\mathbf{k},-} \hat{\sigma}'_{\mathbf{k},-} \Big], \\
\hat{H}^{\text{eff}}_{\text{cav}} &= \sum_{\mathbf{k}} \Big(E_0 + \frac{\hbar^2 |\mathbf{k}|^2}{2m^*} + \zeta |\mathbf{k}| \cos\phi \Big) \hat{a}^{\dagger}_{\mathbf{k},+} \hat{a}_{\mathbf{k},+} + \Big(E_0 + \frac{\hbar^2 |\mathbf{k}|^2}{2m^*} - \zeta |\mathbf{k}| \cos\phi \Big) \hat{a}^{\dagger}_{\mathbf{k},-} \hat{a}_{\mathbf{k},-} \\
&\quad + \Big(-\beta_0 + \beta |\mathbf{k}|^2 e^{-i2\phi} \Big) \hat{a}^{\dagger}_{\mathbf{k},+} \hat{a}_{\mathbf{k},-} + \Big(-\beta_0 + \beta |\mathbf{k}|^2 e^{i2\phi} \Big) \hat{a}^{\dagger}_{\mathbf{k},-} \hat{a}_{\mathbf{k},+}, \\
\hat{H}^{\text{eff}}_{\text{cav-mol}} &= \sum_{\mathbf{k}} \Bigg[\sqrt{1 - f_- - 2f_+} \Big(\mathbf{J}_{\mathbf{k},+} \cdot \boldsymbol{\mu}_+ \hat{\sigma}'^{\dagger}_{\mathbf{k},+} \hat{a}_{\mathbf{k},+} \\
&\quad + \mathbf{J}_{\mathbf{k},-} \cdot \boldsymbol{\mu}_+ \hat{\sigma}'^{\dagger}_{\mathbf{k},+} \hat{a}_{\mathbf{k},-} \Big) + \sqrt{1 - f_+ - 2f_-} \Big(\mathbf{J}_{\mathbf{k},+} \cdot \boldsymbol{\mu}_- \hat{\sigma}'^{\dagger}_{\mathbf{k},-} \hat{a}_{\mathbf{k},+} \\
&\quad + \mathbf{J}_{\mathbf{k},-} \cdot \boldsymbol{\mu}_- \hat{\sigma}'^{\dagger}_{\mathbf{k},-} \hat{a}_{\mathbf{k},-} \Big) \Bigg] + \text{H.c.}
\end{aligned}
\tag{B.14}
$$

We define states $|\mathbf{k}, \pm_{\text{mol}}\rangle'$ and $|\mathbf{k}, \pm_{\text{cav}}\rangle'$ corresponding to operators $\hat{\sigma}'^{\dagger}_{\mathbf{k},\pm}$ and $\hat{a}^{\dagger}_{\mathbf{k},\pm}$, respectively.

Writing the Hamiltonian $\hat{H}^{\text{eff}}(\mathbf{k}) = \langle \mathbf{k}| \hat{H}^{\text{eff}} |\mathbf{k}\rangle$ in the above basis we obtain,

$$\hat{H}^{\text{eff}}(\mathbf{k}) = \hat{H}^{\text{eff}}_{\text{mol}}(\mathbf{k}) + \hat{H}^{\text{eff}}_{\text{cav}}(\mathbf{k}) + \hat{H}^{\text{eff}}_{\text{cav-mol}}(\mathbf{k}), \tag{B.15}$$

where,

$$\begin{aligned}
\hat{H}^{\text{eff}}_{\text{mol}}(\mathbf{k}) =& \hbar\omega_{\text{e}} |+_{\text{mol}}\rangle' \langle +_{\text{mol}}|' + \hbar\omega_{\text{e}} |-_{\text{mol}}\rangle' \langle -_{\text{mol}}|', \\
\hat{H}^{\text{eff}}_{\text{cav}}(\mathbf{k}) =& \left(E_0 + \frac{\hbar^2|\mathbf{k}|^2}{2m^*} + \zeta|\mathbf{k}|\cos\phi\right) |+_{\text{cav}}\rangle' \langle +_{\text{cav}}|' \\
&+ \left(E_0 + \frac{\hbar^2|\mathbf{k}|^2}{2m^*} - \zeta|\mathbf{k}|\cos\phi\right) |-_{\text{cav}}\rangle' \langle -_{\text{cav}}|' \\
&+ \left(-\beta_0 + \beta|\mathbf{k}|^2 e^{-i2\phi}\right) |+_{\text{cav}}\rangle' \langle -_{\text{cav}}|' + \left(-\beta_0 + \beta|\mathbf{k}|^2 e^{i2\phi}\right) |-_{\text{cav}}\rangle' \langle +_{\text{cav}}|', \\
\hat{H}^{\text{eff}}_{\text{cav-mol}}(\mathbf{k}) =& \mathbf{J}_{\mathbf{k},+} \cdot \left(\sqrt{1 - f_- - 2f_+}\boldsymbol{\mu}_+ |+_{\text{mol}}\rangle' + \sqrt{1 - f_+ - 2f_-}\boldsymbol{\mu}_- |-_{\text{mol}}\rangle'\right) \langle +_{\text{cav}}|' \\
&+ \mathbf{J}_{\mathbf{k},-} \cdot \left(\sqrt{1 - f_- - 2f_+}\boldsymbol{\mu}_+ |+_{\text{mol}}\rangle' + \sqrt{1 - f_+ - 2f_-}\boldsymbol{\mu}_- |-_{\text{mol}}\rangle'\right) \langle -_{\text{cav}}|' + \text{H.c.}
\end{aligned} \tag{B.16}$$

Upon pumping with circularly polarized light, the lowest band gradually changes from containing equal number of modes of both circular polarizations to overwhelmingly containing modes of a single polarization as $|f_+ - f_-|$ increases (Fig. B.2).

B.4 Parameters

B.4.1 Perylene filled cavity

We take parameters for the perylene filled cavity $\beta_0 = 0.1\text{eV}$, $\beta = 9 \times 10^{-4}\text{eV}\mu\text{m}^2$, $\zeta = 2.5 \times 10^{-3}\text{eV}\mu\text{m}$, $m^* = 125\hbar^2\text{eV}^{-1}\mu\text{m}^{-2}$, and $L_z = 0.745\mu\text{m}$, where these are similar to those used to model the experiments of Ren *et al.* [79] (Fig. 3, 4, and 5 in main manuscript). On the other hand, we modify E_0 and n_z such that they make the photon modes in our model near resonant with the transition that is strongly coupled to the cavity. For instance, we take $E_0 = 3.80\text{eV}$ and $n_z = 11$ for porphyrin (Fig. 3 and 4); $E_0 = 2.50\text{eV}$ and $n_z = 9$ for Ce:YAG (Fig. 5b-c); and $E_0 = 1.80\text{eV}$ and $n_z = 5$ for MoS_2 (Fig. 5e-f). We assume that perylene has a

similar effect on these different photon modes, as it does on modes with $E_0 \sim 2.27$eV at $\mathbf{k} = 0$ in experiments [79]. This may not necessarily be true, however, as we consider a perylene filled cavity only to achieve frequency separation of photon modes with different polarization, and this can instead be easily achieved with an electrically tunable liquid crystal cavity [78], replacing a perylene filled cavity with a liquid-crystal cavity will not modify the underlying physics of the phenomenon we are interested in, *i.e.*, the idea of using saturation to break TRS will remain intact.

B.4.2 Porphyrin, Ce:YAG, and monolayer MoS_2

We take areal density $\rho_A = 3.55 \times 10^5 \mu\text{m}^{-2}$ ($\sim$ 2000 molecules in 75nm $\times$ 75nm) [155], relative permittivity $\varepsilon = 1.5$ [156], frequency $\hbar\omega_\text{e} = 3.8056$eV and transition dipole $\mu_0 = 1.1184\text{au} \times 2.5417\text{D/au} = 2.84\text{D}$ [91] for the porphyrin film. Also, we consider 100 such porphyrin films stacked one over the other along the z direction within the cavity to achieve strong light-matter coupling, $N_z = 100$. Therefore, the effective areal density of molecules $\rho'_A = N_z\rho_A$ will be used instead of ρ_A while computing $\mathbf{J}_{\mathbf{k},\alpha}$. These are the parameters used to generate Fig. 3 and 4.

Similarly, using density $\rho_\text{YAG} = 5.11\text{g cm}^{-3}$, molar mass $M_\text{YAG} = 738\text{ g mol}^{-1}$, number of Y^{3+} per unit cell $n_{Y^{3+}} = 3$, and concentration of Ce^{3+} (relative to Y^{3+}) $1\% = 10^{-2}$ [157], we obtain the effective areal density of Ce^{3+} ions in a $L'_z = 0.1\mu$m thick layer of Ce:YAG to be $\rho'_A = 10^{-2}L'_z n_{Y^{3+}}\rho_\text{YAG}N_A/M_\text{YAG} = 1.25 \times 10^7 \mu\text{m}^{-2}$. This will be used while computing $\mathbf{J}_{\mathbf{k},\alpha}$ in place of ρ_A. We use relative permittivity $\varepsilon = 12$ [158] and frequency $\hbar\omega_\text{e} = 2.53$eV (489nm [108]) for the transition in a Ce:YAG crystal. Using the oscillator strength of this transition 0.286 [108], we calculate the transition dipole $\mu_0 = 5.46\text{D}$. These are the parameters used to generate Fig. 5c.

For monolayer MoS_2, we consider A-excitons at $\hbar\omega_\text{e} = 1.855$eV [120]. From Chen *et al*. [120], we take the Rabi splitting at resonance, and use $\mu_0\sqrt{\rho_A}\sqrt{\hbar\omega_\text{e}/2L_z\varepsilon\epsilon_0} \approx 39\text{meV}/2 = 19.5\text{meV}$ in our calculations (Fig. 5f).

Bibliography

[1] D. G. Lidzey, D. Bradley, M. Skolnick, T. Virgili, S. Walker, and D. Whittaker, "Strong exciton–photon coupling in an organic semiconductor microcavity," Nature **395**, 53–55 (1998).

[2] A. Shalabney, J. George, J. a. Hutchison, G. Pupillo, C. Genet, and T. W. Ebbesen, "Coherent coupling of molecular resonators with a microcavity mode," Nat. Commun. **6**, 1–6 (2015).

[3] C. Weisbuch, M. Nishioka, A. Ishikawa, and Y. Arakawa, "Observation of the coupled exciton-photon mode splitting in a semiconductor quantum microcavity," Phys. Rev. Lett. **69**, 3314–3317 (1992).

[4] R. Butté, G. Christmann, E. Feltin, J.-F. Carlin, M. Mosca, M. Ilegems, and N. Grandjean, "Room-temperature polariton luminescence from a bulk gan microcavity," Phys. Rev. B **73**, 033315 (2006).

[5] X. Liu, T. Galfsky, Z. Sun, F. Xia, E.-c. Lin, Y.-H. Lee, S. Kéna-Cohen, and V. M. Menon, "Strong light–matter coupling in two-dimensional atomic crystals," Nat. Photonics **9**, 30–34 (2015).

[6] J. P. Long and B. Simpkins, "Coherent coupling between a molecular vibration and fabry–perot optical cavity to give hybridized states in the strong coupling limit," ACS Photonics **2**, 130–136 (2015).

[7] M. Moore and A. Vardi, "Bose-enhanced chemistry: Amplification of selectivity in the dissociation of molecular bose-einstein condensates," Phys. Rev. Lett. **88**, 160402 (2002).

[8] D. Heinzen, R. Wynar, P. Drummond, and K. Kheruntsyan, "Superchemistry: dynamics of coupled atomic and molecular bose-einstein condensates," Phys. Rev. Lett. **84**, 5029 (2000).

[9] J. Keeling and S. Kéna-Cohen, "Bose–einstein condensation of exciton-polaritons in organic microcavities," Annu. Rev. Phys. Chem. **71**, 435–459 (2020).

[10] R. Su, A. Fieramosca, Q. Zhang, H. S. Nguyen, E. Deleporte, Z. Chen, D. Sanvitto, T. C. Liew, and Q. Xiong, "Perovskite semiconductors for room-temperature exciton-polaritonics," Nat. Mater. **20**, 1315–1324 (2021).

[11] S. Pannir-Sivajothi, J. A. Campos-Gonzalez-Angulo, L. A. Martínez-Martínez, S. Sinha, and J. Yuen-Zhou, "Driving chemical reactions with polariton condensates," Nat. Commun. **13**, 1–9 (2022).

[12] S. Pannir-Sivajothi, N. P. Stern, and J. Yuen-Zhou, "Molecular and solid-state topological polaritons induced by population imbalance," Nanophotonics **12**, 3109–3119 (2023).

[13] A. Thomas, L. Lethuillier-Karl, K. Nagarajan, R. M. Vergauwe, J. George, T. Chervy, A. Shalabney, E. Devaux, C. Genet, J. Moran *et al.*, "Tilting a ground-state reactivity landscape by vibrational strong coupling," Science **363**, 615–619 (2019).

[14] K. Hirai, R. Takeda, J. A. Hutchison, and H. Uji-i, "Modulation of prins cyclization by vibrational strong coupling," Angew. Chem. **132**, 5370–5373 (2020).

[15] T. W. Ebbesen, "Hybrid light–matter states in a molecular and material science perspective," Acc. Chem. Res. **49**, 2403–2412 (2016).

[16] W. Ahn, J. F. Triana, F. Recabal, F. Herrera, and B. S. Simpkins, "Modification of ground-state chemical reactivity via light–matter coherence in infrared cavities," Science **380**, 1165–1168 (2023).

[17] J. Campos-Gonzalez-Angulo, Y. Poh, M. Du, and J. Yuen-Zhou, "Swinging between shine and shadow: Theoretical advances on thermally activated vibropolaritonic chemistry," The Journal of Chemical Physics **158** (2023).

[18] G. D. Wiesehan and W. Xiong, "Negligible rate enhancement from reported cooperative vibrational strong coupling catalysis," The Journal of Chemical Physics **155** (2021).

[19] M. V. Imperatore, J. B. Asbury, and N. C. Giebink, "Reproducibility of cavity-enhanced chemical reaction rates in the vibrational strong coupling regime," The Journal of Chemical Physics **154** (2021).

[20] Z. Brawley, J. E. Yim*, S. Pannir-Sivajothi*, Y. R. Poh, J. Yuen-Zhou, and M. Sheldon, "Sub-wavelength chemical imaging of a modified reaction due to vibrational strong coupling," ChemRxiv preprint (2023).

[21] X. Li, A. Mandal, and P. Huo, "Cavity frequency-dependent theory for vibrational polariton chemistry," Nature communications **12**, 1315 (2021).

[22] J. Galego, C. Climent, F. J. Garcia-Vidal, and J. Feist, "Cavity casimir-polder forces and their effects in ground-state chemical reactivity," Phys. Rev. X **9**, 021057 (2019).

[23] T. E. Li, A. Nitzan, and J. E. Subotnik, "On the origin of ground-state vacuum-field catalysis: Equilibrium consideration," J. Chem. Phys. **152**, 234107 (2020).

[24] J. A. Campos-Gonzalez-Angulo and J. Yuen-Zhou, "Polaritonic normal modes in transition state theory," J. Chem. Phys. **152**, 161101 (2020).

[25] N. P. Proukakis, D. W. Snoke, and P. B. Littlewood, *Universal Themes of Bose-Einstein Condensation* Cambridge Univ. Press, Cambridge, (2017).

[26] K. Daskalakis, S. Maier, R. Murray, and S. Kéna-Cohen, "Nonlinear interactions in an organic polariton condensate," Nat. Mater. **13**, 271–278 (2014).

[27] J. D. Plumhof, T. Stöferle, L. Mai, U. Scherf, and R. F. Mahrt, "Room-temperature bose–einstein condensation of cavity exciton–polaritons in a polymer," Nat. Mater. **13**, 247–252 (2014).

[28] C. P. Dietrich, A. Steude, L. Tropf, M. Schubert, N. M. Kronenberg, K. Ostermann, S. Höfling, and M. C. Gather, "An exciton-polariton laser based on biologically produced fluorescent protein," Sci. Adv. **2**, e1600666 (2016).

[29] A. I. Väkeväinen, A. J. Moilanen, M. Nečada, T. K. Hakala, K. S. Daskalakis, and P. Törmä, "Sub-picosecond thermalization dynamics in condensation of strongly coupled lattice plasmons," Nat. Commun. **11**, 1–12 (2020).

[30] A. V. Zasedatelev, A. V. Baranikov, D. Urbonas, F. Scafirimuto, U. Scherf, T. Stöferle, R. F. Mahrt, and P. G. Lagoudakis, "A room-temperature organic polariton transistor," Nat. Photon. **13**, 378–383 (2019).

[31] M. A. Zeb, P. G. Kirton, and J. Keeling, "Incoherent charge transport in an organic polariton condensate," Preprint at https://arxiv.org/abs/2004.09790 (2020).

[32] M. Du, R. F. Ribeiro, and J. Yuen-Zhou, "Remote control of chemistry in optical cavities," Chem **5**, 1167–1181 (2019).

[33] M. Delor, P. A. Scattergood, I. V. Sazanovich, A. W. Parker, G. M. Greetham, A. J. Meijer, M. Towrie, and J. A. Weinstein, "Toward control of electron transfer in donor-acceptor molecules by bond-specific infrared excitation," Science **346**, 1492–1495 (2014).

[34] S. Hammes-Schiffer and J. C. Tully, "Vibrationally enhanced proton transfer," J. Phys. Chem. **99**, 5793–5797 (1995).

[35] A. Strashko, P. Kirton, and J. Keeling, "Organic polariton lasing and the weak to strong coupling crossover," Phys. Rev. Lett. **121**, 193601 (2018).

[36] E. R. Bittner and C. Silva, "Estimating the conditions for polariton condensation in organic thin-film microcavities," J. Chem. Phys. **136**, 034510 (2012).

[37] J. del Pino, J. Feist, and F. J. Garcia-Vidal, "Quantum theory of collective strong coupling of molecular vibrations with a microcavity mode," New J. Phys. **17**, 053040 (2015).

[38] N. Somaschi, L. Mouchliadis, D. Coles, I. Perakis, D. Lidzey, P. Lagoudakis, and P. Savvidis, "Ultrafast polariton population build-up mediated by molecular phonons in organic microcavities," Appl. Phys. Lett. **99**, 209 (2011).

[39] A. Dunkelberger, B. Spann, K. Fears, B. Simpkins, and J. Owrutsky, "Modified relaxation dynamics and coherent energy exchange in coupled vibration-cavity polaritons," Nat. Commun. **7**, 1–10 (2016).

[40] B. Xiang, R. F. Ribeiro, L. Chen, J. Wang, M. Du, J. Yuen-Zhou, and W. Xiong, "State-selective polariton to dark state relaxation dynamics," J. Phys. Chem. A **123**, 5918–5927 (2019).

[41] H. Fröhlich, "Bose condensation of strongly excited longitudinal electric modes," Phys. Lett. A **26**, 402–403 (1968).

[42] Z. Zhang, G. S. Agarwal, and M. O. Scully, "Quantum fluctuations in the fröhlich condensate of molecular vibrations driven far from equilibrium," Phys. Rev. Lett. **122**, 158101 (2019).

[43] L. Banyai, P. Gartner, O. Schmitt, and H. Haug, "Condensation kinetics for bosonic excitons interacting with a thermal phonon bath," Phys. Rev. B **61**, 8823 (2000).

[44] A. Imamoglu, R. Ram, S. Pau, Y. Yamamoto *et al.*, "Nonequilibrium condensates and lasers without inversion: Exciton-polariton lasers," Phys. Rev. A **53**, 4250 (1996).

[45] I. Vurgaftman, B. S. Simpkins, A. D. Dunkelberger, and J. C. Owrutsky, "Negligible effect of vibrational polaritons on chemical reaction rates via the density of states pathway," J. Phys. Chem. Lett. **11**, 3557–3562 (2020).

[46] J. Del Pino, F. J. Garcia-Vidal, and J. Feist, "Exploiting vibrational strong coupling to make an optical parametric oscillator out of a raman laser," Phys. Rev. Lett. **117**, 277401 (2016).

[47] F. Herrera and F. C. Spano, "Cavity-controlled chemistry in molecular ensembles," Phys. Rev. Lett. **116**, 238301 (2016).

[48] A. Semenov and A. Nitzan, "Electron transfer in confined electromagnetic fields," J. Chem. Phys. **150**, 174122 (2019).

[49] J. A. Campos-Gonzalez-Angulo, R. F. Ribeiro, and J. Yuen-Zhou, "Resonant catalysis of thermally activated chemical reactions with vibrational polaritons," Nat. Commun. **10**, 1–8 (2019).

[50] N. T. Phuc, P. Q. Trung, and A. Ishizaki, "Controlling the nonadiabatic electron-transfer reaction rate through molecular-vibration polaritons in the ultrastrong coupling regime," Sci. Rep. **10**, 1–11 (2020).

[51] R. A. Marcus, "Chemical and electrochemical electron-transfer theory," Annu. Rev. Phys. Chem. **15**, 155–196 (1964).

[52] V. Levich, "Present state of the theory of oxidation-reduction in solution (bulk and electrode reactions)," Adv. Electrochem. Electrochem. Eng **4**, 249–371 (1966).

[53] J. Jortner, "Temperature dependent activation energy for electron transfer between biological molecules," J. Chem. Phys. **64**, 4860–4867 (1976).

[54] D. J. Nesbitt and R. W. Field, "Vibrational energy flow in highly excited molecules: Role of intramolecular vibrational redistribution," J. Phys. Chem. **100**, 12735–12756 (1996).

[55] A. Strashko and J. Keeling, "Raman scattering with strongly coupled vibron-polaritons," Phys. Rev. A **94**, 023843 (2016).

[56] J. R. Miller, L. Calcaterra, and G. Closs, "Intramolecular long-distance electron transfer in radical anions. the effects of free energy and solvent on the reaction rates," J. Am. Chem. Soc **106**, 3047–3049 (1984).

[57] M. Roche, "On the polyatomic franck-condon factors," Chem. Phys. Lett. **168**, 556–558 (1990).

[58] T. Sharp and H. Rosenstock, "Franck-condon factors for polyatomic molecules," J. Chem. Phys. **41**, 3453–3463 (1964).

[59] A. Toniolo and M. Persico, "Efficient calculation of franck–condon factors and vibronic couplings in polyatomics," J. Comput. Chem. **22**, 968–975 (2001).

[60] E. T. Whittaker and G. N. Watson, *A Course of Modern Analysis, 4th ed* Cambridge Univ. Press, Cambridge, (1996).

[61] H. Frei and G. C. Pimentel, "Infrared induced photochemical processes in matrices," Annu. Rev. Phys. Chem. **36**, 491–524 (1985).

[62] R. André, D. Heger, L. S. Dang, and Y. Merle d'Aubigné, "Spectroscopy of polaritons in cdte-based microcavities," J. Cryst. Growth **184-185**, 758–762 (1998).

[63] R. Shimada, J. Xie, V. Avrutin, Ü. Özgür, and H. Morkoč, "Cavity polaritons in zno-based hybrid microcavities," Appl. Phys. Lett. **92**, 011127 (2008).

[64] A. Brehier, R. Parashkov, J.-S. Lauret, and E. Deleporte, "Strong exciton-photon coupling in a microcavity containing layered perovskite semiconductors," Appl. Phys. Lett. **89**, 171110 (2006).

[65] F. Hu and Z. Fei, "Recent progress on exciton polaritons in layered transition-metal dichalcogenides," Adv. Opt. Mater. **8**, 1901003 (2020).

[66] J. A. Hutchison, T. Schwartz, C. Genet, E. Devaux, and T. W. Ebbesen, "Modifying chemical landscapes by coupling to vacuum fields," Angew. Chem., Int. Ed. **51**, 1592–1596 (2012).

[67] N. Krainova, A. J. Grede, D. Tsokkou, N. Banerji, and N. C. Giebink, "Polaron photoconductivity in the weak and strong light-matter coupling regime," Phys. Rev. Lett. **124**, 177401 (2020).

[68] Q. Liao, C. Leblanc, J. Ren, F. Li, Y. Li, D. Solnyshkov, G. Malpuech, J. Yao, and H. Fu, "Experimental measurement of the divergent quantum metric of an exceptional point," Phys. Rev. Lett. **127**, 107402 (2021).

[69] M. Dusel, S. Betzold, T. H. Harder, M. Emmerling, J. Beierlein, J. Ohmer, U. Fischer, R. Thomale, C. Schneider, S. Hofling *et al.*, "Room-temperature topological polariton laser in an organic lattice," Nano Lett. **21**, 6398–6405 (2021).

[70] D. D. Solnyshkov, G. Malpuech, P. St-Jean, S. Ravets, J. Bloch, and A. Amo, "Microcavity polaritons for topological photonics," Opt. Mater. Express **11**, 1119–1142 (2021).

[71] C.-E. Bardyn, T. Karzig, G. Refael, and T. C. H. Liew, "Topological polaritons and excitons in garden-variety systems," Phys. Rev. B **91**, 161413 (2015).

[72] J. Yuen-Zhou, S. K. Saikin, T. Zhu, M. C. Onbasli, C. A. Ross, V. Bulovic, and M. A. Baldo, "Plexciton dirac points and topological modes," Nat. Commun. **7**, 1–7 (2016).

[73] S. Klembt, T. Harder, O. Egorov, K. Winkler, R. Ge, M. Bandres, M. Emmerling, L. Worschech, T. Liew, M. Segev *et al.*, "Exciton-polariton topological insulator," Nature **562**, 552–556 (2018).

[74] T. Karzig, C.-E. Bardyn, N. H. Lindner, and G. Refael, "Topological polaritons," Phys. Rev. X **5**, 031001 (2015).

[75] W. Liu, Z. Ji, Y. Wang, G. Modi, M. Hwang, B. Zheng, V. J. Sorger, A. Pan, and R. Agarwal, "Generation of helical topological exciton-polaritons," Science **370**, 600–604 (2020).

[76] M. Li, I. Sinev, F. Benimetskiy, T. Ivanova, E. Khestanova, S. Kiriushechkina, A. Vakulenko, S. Guddala, M. Skolnick, V. M. Menon *et al.*, "Experimental observation of topological z2 exciton-polaritons in transition metal dichalcogenide monolayers," Nat. Commun. **12**, 1–10 (2021).

[77] A. Gianfrate, O. Bleu, L. Dominici, V. Ardizzone, M. De Giorgi, D. Ballarini, G. Lerario, K. West, L. Pfeiffer, D. Solnyshkov *et al.*, "Measurement of the quantum geometric tensor and of the anomalous hall drift," Nature **578**, 381–385 (2020).

[78] K. Rechcińska, M. Król, R. Mazur, P. Morawiak, R. Mirek, K. Łempicka, W. Bardyszewski, M. Matuszewski, P. Kula, W. Piecek *et al.*, "Engineering spin-orbit synthetic hamiltonians in liquid-crystal optical cavities," Science **366**, 727–730 (2019).

[79] J. Ren, Q. Liao, F. Li, Y. Li, O. Bleu, G. Malpuech, J. Yao, H. Fu, and D. Solnyshkov, "Nontrivial band geometry in an optically active system," Nat. Commun. **12**, 1–8 (2021).

[80] K. Łempicka-Mirek, M. Król, H. Sigurdsson, A. Wincukiewicz, P. Morawiak, R. Mazur, M. Muszyński, W. Piecek, P. Kula, T. Stefaniuk *et al.*, "Electrically tunable berry curvature and strong light-matter coupling in liquid crystal microcavities with 2d perovskite," Sci. Adv. **8**, eabq7533 (2022).

[81] S. Guddala, Y. Kawaguchi, F. Komissarenko, S. Kiriushechkina, A. Vakulenko, K. Chen, A. Alù, V. M Menon, and A. B. Khanikaev, "All-optical nonreciprocity due to valley polarization pumping in transition metal dichalcogenides," Nat. Commun. **12**, 1–9 (2021).

[82] E. J. Lenferink, G. Wei, and N. P. Stern, "Coherent optical non-reciprocity in axisymmetric resonators," Opt. Express **22**, 16099–16111 (2014).

[83] K. Schwennicke and J. Yuen-Zhou, "Optical activity from the exciton aharonov–bohm effect: A floquet engineering approach," J. Phys. Chem. C **124**, 4206–4214 (2020).

[84] O. Bleu, D. D. Solnyshkov, and G. Malpuech, "Photonic versus electronic quantum anomalous hall effect," Phys. Rev. B **95**, 115415 (2017).

[85] T. Long, X. Ma, J. Ren, F. Li, Q. Liao, S. Schumacher, G. Malpuech, D. Solnyshkov, and H. Fu, "Helical polariton lasing from topological valleys in an organic crystalline microcavity," Adv. Sci. **9**, 2203588 (2022).

[86] M. Rubio, B. O. Roos, L. Serrano-Andrés, and M. Merchán, "Theoretical study of the electronic spectrum of magnesium-porphyrin," J. Chem. Phys. **110**, 7202–7209 (1999).

[87] L. Edwards, D. H. Dolphin, and M. Gouterman, "Porphyrins: Xvi. vapor absorption spectra and redox reactions: Octalkylporphins," J. Mol. Spectrosc. **35**, 90–109 (1970).

[88] T. Rangel, A. Rinn, S. Sharifzadeh, F. H. da Jornada, A. Pick, S. G. Louie, G. Witte, L. Kronik, J. B. Neaton, and S. Chatterjee, "Low-lying excited states in crystalline perylene," Proc. Natl. Acad. Sci. U.S.A. **115**, 284–289 (2018).

[89] I. Barth, J. Manz, Y. Shigeta, and K. Yagi, "Unidirectional electronic ring current driven by a few cycle circularly polarized laser pulse: quantum model simulations for mg- porphyrin," J. Am. Chem. Soc. **128**, 7043–7049 (2006).

[90] J. Yuen-Zhou, S. K. Saikin, N. Y. Yao, and A. Aspuru-Guzik, "Topologically protected excitons in porphyrin thin films," Nat. Mater. **13**, 1026–1032 (2014).

[91] S. Sun, B. Gu, and S. Mukamel, "Polariton ring currents and circular dichroism of mg-porphyrin in a chiral cavity," Chem. Sci. **13**, 1037–1048 (2022).

[92] S. Mukamel, *Principles of nonlinear optical spectroscopy*, 6 Oxford University Press, (1999).

[93] V. Agranovich, *Excitations in Organic Solids* Oxford University Press, (2008).

[94] A. V. Kavokin, J. J. Baumberg, G. Malpuech, and F. P. Laussy, *Microcavities*, vol. 21 Oxford University Press, (2017).

[95] G. Panzarini, L. C. Andreani, A. Armitage, D. Baxter, M. S. Skolnick, V. N. Astratov, J. S. Roberts, A. V. Kavokin, M. R. Vladimirova, and M. A. Kaliteevski, "Exciton-light coupling in single and coupled semiconductor microcavities: Polariton dispersion and polarization splitting," Phys. Rev. B **59**, 5082–5089 (1999).

[96] M. G. Silveirinha, "Chern invariants for continuous media," Phys. Rev. B **92**, 125153 (2015).

[97] U. Even, J. Magen, J. Jortner, J. Friedman, and H. Levanon, "Isolated ultracold porphyrins in supersonic expansions. i. free-base tetraphenylporphyrin and zn-tetraphenylporphyrin," J. Chem. Phys. **77**, 4374–4383 (1982).

[98] S. Voelker, R. Macfarlane, A. Genack, H. Trommsdorff, and J. van Der Waals, "Homogeneous linewidth of the s 1← s 0 transition of free-base porphyrin in an n-octane crystal as studied by photochemical hole-burning," J. Chem. Phys. **67**, 1759–1765 (1977).

[99] B. Xiang, R. F. Ribeiro, A. D. Dunkelberger, J. Wang, Y. Li, B. S. Simpkins, J. C. Owrutsky, J. Yuen-Zhou, and W. Xiong, "Two-dimensional infrared spectroscopy of vibrational polaritons," Proc. Natl. Acad. Sci. U.S.A. **115**, 4845–4850 (2018).

[100] T. Yagafarov, D. Sannikov, A. Zasedatelev, K. Georgiou, A. Baranikov, O. Kyriienko, I. Shelykh, L. Gai, Z. Shen, D. Lidzey *et al.*, "Mechanisms of blueshifts in organic polariton condensates," Commun. Phys. **3**, 1–10 (2020).

[101] R. F. Ribeiro, A. D. Dunkelberger, B. Xiang, W. Xiong, B. S. Simpkins, J. C. Owrutsky, and J. Yuen-Zhou, "Theory for nonlinear spectroscopy of vibrational polaritons," J. Phys. Chem. Lett. **9**, 3766–3771 (2018).

[102] A. H. Salij, R. H. Goldsmith, and R. Tempelaar, "Chiral polaritons based on achiral fabry-perot cavities using apparent circular dichroism," arXiv preprint arXiv:2208.14461 (2022).

[103] L. Polimeno, G. Lerario, M. De Giorgi, L. De Marco, L. Dominici, F. Todisco, A. Coriolano, V. Ardizzone, M. Pugliese, C. T. Prontera *et al.*, "Tuning of the berry curvature in 2d perovskite polaritons," Nat. Nanotechnol. **16**, 1349–1354 (2021).

[104] C. Galli, K. Wynne, S. M. LeCours, M. Therien, and R. Hochstrasser, "Direct measurement of electronic dephasing using anisotropy," Chem. Phys. Lett. **206**, 493–499 (1993).

[105] L. Pickup, K. Kalinin, A. Askitopoulos, Z. Hatzopoulos, P. G. Savvidis, N. G. Berloff, and P. G. Lagoudakis, "Optical bistability under nonresonant excitation in spinor polariton condensates," Phys. Rev. Lett. **120**, 225301 (2018).

[106] L. Young, K. Ueda, M. Gühr, P. H. Bucksbaum, M. Simon, S. Mukamel, N. Rohringer, K. C. Prince, C. Masciovecchio, M. Meyer, A. Rudenko, D. Rolles, C. Bostedt, M. Fuchs, D. A. Reis, R. Santra, H. Kapteyn, M. Murnane, H. Ibrahim, F. Légaré, M. Vrakking, M. Isinger, D. Kroon, M. Gisselbrecht, A. L'Huillier, H. J. Wörner, and S. R. Leone, "Roadmap of ultrafast x-ray atomic and molecular physics," Journal of Physics B: Atomic, Molecular and Optical Physics **51**, 032003 (2018).

[107] L. J. P. Ament, M. van Veenendaal, T. P. Devereaux, J. P. Hill, and J. van den Brink, "Resonant inelastic x-ray scattering studies of elementary excitations," Rev. Mod. Phys. **83**, 705–767 (2011).

[108] R. Kolesov, K. Xia, R. Reuter, M. Jamali, R. Stöhr, T. Inal, P. Siyushev, and J. Wrachtrup, "Mapping spin coherence of a single rare-earth ion in a crystal onto a single photon polarization state," Phys. Rev. Lett. **111**, 120502 (2013).

[109] R. J. Moerland, I. G. C. Weppelman, M. Scotuzzi, and J. P. Hoogenboom, "Nanoscale imaging of light-matter coupling inside metal-coated cavities with a pulsed electron beam," Nano Lett. **18**, 6107–6112 (2018).

[110] S. R. K. Rodriguez, S. Murai, M. A. Verschuuren, and J. G. Rivas, "Light-emitting waveguide-plasmon polaritons," Phys. Rev. Lett. **109**, 166803 (2012).

[111] T. Zhong, J. M. Kindem, E. Miyazono, and A. Faraon, "Nanophotonic coherent light–matter interfaces based on rare-earth-doped crystals," Nat. Commun. **6**, 1–6 (2015).

[112] T. Zhong, J. M. Kindem, J. Rochman, and A. Faraon, "Interfacing broadband photonic qubits to on-chip cavity-protected rare-earth ensembles," Nat. Commun. **8**, 1–7 (2017).

[113] P. Siyushev, K. Xia, R. Reuter, M. Jamali, N. Zhao, N. Yang, C. Duan, N. Kukharchyk, A. Wieck, R. Kolesov *et al.*, "Coherent properties of single rare-earth spin qubits," Nat. Commun. **5**, 1–6 (2014).

[114] K. F. Mak, K. He, J. Shan, and T. F. Heinz, "Control of valley polarization in monolayer mos2 by optical helicity," Nat. Nanotechnol. **7**, 494–498 (2012).

[115] H. Zeng, J. Dai, W. Yao, D. Xiao, and X. Cui, "Valley polarization in mos2 monolayers by optical pumping," Nat. Nanotechnol. **7**, 490–493 (2012).

[116] A. K. Pattanayak, P. Das, D. Chakrabarty, A. Dhara, S. Paul, S. Maji, M. M. Brundavanam, and S. Dhara, "Probing spin dynamics of 2d excitons with twisted light," ACS Photonics **9**, 3351–3356 (2022).

[117] L. Sun, C.-Y. Wang, A. Krasnok, J. Choi, J. Shi, J. S. Gomez-Diaz, A. Zepeda, S. Gwo, C.-K. Shih, A. Alù *et al.*, "Separation of valley excitons in a mos2 monolayer using a subwavelength asymmetric groove array," Nat. Photonics **13**, 180–184 (2019).

[118] G.-H. Peng, O. J. G. Sanchez, W.-H. Li, P.-Y. Lo, and S.-J. Cheng, "Twisted-light-induced exciton wave packets in transition-metal dichalcogenide monolayers," arXiv preprint arXiv:2203.02081 (2022).

[119] S. Dal Conte, F. Bottegoni, E. A. A. Pogna, D. De Fazio, S. Ambrogio, I. Bargigia, C. D'Andrea, A. Lombardo, M. Bruna, F. Ciccacci, A. C. Ferrari, G. Cerullo, and M. Finazzi, "Ultrafast valley relaxation dynamics in monolayer mos_2 probed by nonequilibrium optical techniques," Phys. Rev. B **92**, 235425 (2015).

[120] Y.-J. Chen, J. D. Cain, T. K. Stanev, V. P. Dravid, and N. P. Stern, "Valley-polarized exciton–polaritons in a monolayer semiconductor," Nat. Photonics **11**, 431–435 (2017).

[121] T. LaMountain, J. Nelson, E. J. Lenferink, S. H. Amsterdam, A. A. Murthy, H. Zeng, T. J. Marks, V. P. Dravid, M. C. Hersam, and N. P. Stern, "Valley-selective optical stark effect of exciton-polaritons in a monolayer semiconductor," Nat. Commun. **12**, 1–7 (2021).

[122] B. Datta, M. Khatoniar, P. Deshmukh, F. Thouin, R. Bushati, S. De Liberato, S. K. Cohen, and V. M. Menon, "Highly nonlinear dipolar exciton-polaritons in bilayer mos2," Nat. Commun. **13**, 1–7 (2022).

[123] C. Louca, A. Genco, S. Chiavazzo, T. P. Lyons, S. Randerson, C. Trovatello, P. Claronino, R. Jayaprakash, K. Watanabe, T. Taniguchi *et al.*, "Nonlinear interactions of dipolar excitons and polaritons in mos2 bilayers," arXiv preprint arXiv:2204.00485 (2022).

[124] M. Muszyński, M. Król, K. Rechcińska, P. Oliwa, M. Kędziora, K. Łempicka-Mirek, R. Mazur, P. Morawiak, W. Piecek, P. Kula, P. G. Lagoudakis, B. Piętka, and J. Szczytko, "Realizing persistent-spin-helix lasing in the regime of rashba-dresselhaus spin-orbit coupling in a dye-filled liquid-crystal optical microcavity," Phys. Rev. Appl. **17**, 014041 (2022).

[125] T. Renger and R. A. Marcus, "On the relation of protein dynamics and exciton relaxation in pigment–protein complexes: An estimation of the spectral density and a theory for the calculation of optical spectra," The Journal of Chemical Physics **116**, 9997–10019 (2002).

[126] A. Thomas, J. George, A. Shalabney, M. Dryzhakov, S. J. Varma, J. Moran, T. Chervy, X. Zhong, E. Devaux, C. Genet *et al.*, "Ground-state chemical reactivity under vibrational coupling to the vacuum electromagnetic field," Angewandte Chemie **128**, 11634–11638 (2016).

[127] A. P. Fidler, L. Chen, A. M. McKillop, and M. L. Weichman, "Ultrafast dynamics of cn radical reactions with chloroform solvent under vibrational strong coupling," arXiv preprint arXiv:2307.04875 (2023).

[128] P. Pilar, D. De Bernardis, and P. Rabl, "Thermodynamics of ultrastrongly coupled light-matter systems," Quantum **4**, 335 (2020).

[129] K. Y. Fong, H.-K. Li, R. Zhao, S. Yang, Y. Wang, and X. Zhang, "Phonon heat transfer across a vacuum through quantum fluctuations," Nature **576**, 243–247 (2019).

[130] F. P. Incropera, D. P. DeWitt, T. L. Bergman, A. S. Lavine *et al.*, *Fundamentals of heat and mass transfer*, vol. 6 Wiley New York, (1996).

[131] D. W. Mackowski, "Conduction heat transfer: Notes for mech 7210," Mechanical Engineering Department, Auburn University (2011).

[132] A. Lock and H. Bakker, "Temperature dependence of vibrational relaxation in liquid h 2 o," The Journal of chemical physics **117**, 1708–1713 (2002).

[133] S. T. Van der Post, C.-S. Hsieh, M. Okuno, Y. Nagata, H. J. Bakker, M. Bonn, and J. Hunger, "Strong frequency dependence of vibrational relaxation in bulk and surface water reveals sub-picosecond structural heterogeneity," Nature communications **6**, 8384 (2015).

[134] S. Pandelov, B. M. Pilles, J. C. Werhahn, and H. Iglev, "Time-resolved dynamics of the oh stretching vibration in aqueous nacl hydrate," The Journal of Physical Chemistry A **113**, 10184–10188 (2009).

[135] D. Hutzler, C. Brunner, P. S. Petkov, T. Heine, S. F. Fischer, E. Riedle, R. Kienberger, and H. Iglev, "Dynamics of the oh stretching mode in crystalline ba (clo4) 2· 3h2o," The Journal of Chemical Physics **148** (2018).

[136] D. Hutzler, K. Stallhofer, R. Kienberger, E. Riedle, and H. Iglev, "Icelike vibrational properties of strong hydrogen bonds in hydrated lithium nitrate," The Journal of Physical Chemistry A **124**, 5784–5789 (2020).

[137] D. Hutzler, J. C. Werhahn, R. Heider, M. Bradler, R. Kienberger, E. Riedle, and H. Iglev, "Highly selective relaxation of the oh stretching overtones in isolated hdo molecules observed by infrared pump–repump–probe spectroscopy," The Journal of Physical Chemistry A **119**, 6831–6836 (2015).

[138] M. Thoss, H. Wang, and W. H. Miller, "Self-consistent hybrid approach for complex systems: Application to the spin-boson model with debye spectral density," The Journal of Chemical Physics **115**, 2991–3005 (2001).

[139] A. Tokmakoff, "Time-dependent quantum mechanics and spectroscopy," (2014).

[140] F. Ansbacher, "A note on the overlap integral of two harmonic oscillator wave functions," Zeitschrift für Naturforschung A **14**, 889–892 (1959).

[141] J.-L. Chang, "A new formula to calculate franck–condon factors for displaced and distorted harmonic oscillators," Journal of Molecular Spectroscopy **232**, 102–104 (2005).

[142] P. T. Ruhoff and M. A. Ratner, "Algorithms for computing franck–condon overlap integrals," International Journal of Quantum Chemistry **77**, 383–392 (2000).

[143] M. Lax, "The franck-condon principle and its application to crystals," The Journal of chemical physics **20**, 1752–1760 (1952).

[144] D. Fitchen, W. B. Fowler, C. H. Henry, M. V. Klein, R. Knox, F. Lüty, H. Mahr, H. Seidel, C. P. Slichter, K. J. Teegarden *et al.*, *Physics of color centers* Academic Press, (1968).

[145] M. de Jong, L. Seijo, A. Meijerink, and F. T. Rabouw, "Resolving the ambiguity in the relation between stokes shift and huang–rhys parameter," Physical Chemistry Chemical Physics **17**, 16959–16969 (2015).

[146] W. Stadler, D. Hofmann, H. Alt, T. Muschik, B. Meyer, E. Weigel, G. Müller-Vogt, M. Salk, E. Rupp, and K. Benz, "Optical investigations of defects in cd 1- x zn x te," Physical review B **51**, 10619 (1995).

[147] J. Luo, X. Wang, S. Li, J. Liu, Y. Guo, G. Niu, L. Yao, Y. Fu, L. Gao, Q. Dong *et al.*, "Efficient and stable emission of warm-white light from lead-free halide double perovskites," Nature **563**, 541–545 (2018).

[148] H. T. Cao, T. Doan, D. T. Thoai, and H. Haug, "Condensation kinetics of cavity polaritons interacting with a thermal phonon bath," Phys. Rev. B **69**, 245325 (2004).

[149] C. Fabre and N. Treps, "Modes and states in quantum optics," Reviews of Modern Physics **92**, 035005 (2020).

[150] H. Zoubi and G. C. La Rocca, "Microscopic theory of anisotropic organic cavity exciton polaritons," Physical Review B **71**, 235316 (2005).

[151] M. Martinelli and P. Martelli, "Polarization, mirrors, and reciprocity: birefringence and its compensation in optical retracing circuits," Advances in Optics and Photonics **9**, 129–168 (2017).

[152] J. K. Asbóth, L. Oroszlány, and A. Pályi, *A short course on topological insulators* Springer Cham, (2016).

[153] T. Fukui, Y. Hatsugai, and H. Suzuki, "Chern numbers in discretized brillouin zone: Efficient method of computing (spin) hall conductances," Journal of the Physical Society of Japan **74**, 1674–1677 (2005).

[154] P. Fowler-Wright, B. W. Lovett, and J. Keeling, "Efficient many-body non-markovian dynamics of organic polaritons," Physical Review Letters **129**, 173001 (2022).

[155] B. Hulsken, R. Van Hameren, J. W. Gerritsen, T. Khoury, P. Thordarson, M. J. Crossley, A. E. Rowan, R. J. Nolte, J. A. Elemans, and S. Speller, "Real-time single-molecule imaging of oxidation catalysis at a liquid–solid interface," Nature nanotechnology **2**, 285–289 (2007).

[156] D. Li, B. I. Swanson, J. M. Robinson, and M. A. Hoffbauer, "Porphyrin based self-assembled monolayer thin films: synthesis and characterization," Journal of the American Chemical Society **115**, 6975–6980 (1993).

[157] V. Bachmann, C. Ronda, and A. Meijerink, "Temperature quenching of yellow ce3+ luminescence in yag: Ce," Chemistry of Materials **21**, 2077–2084 (2009).

[158] P. Ctibor, J. Sedláček, and T. Hudec, Boletín de la Sociedad Española de Cerámica y Vidrio .